# Simulation of laser energy deposition with structured light beams in air and machine learning data treatment for LIBS analysis of remote targets

Long Zou

INSTITUT POLYTECHNIQUE DE PARIS

NNT : 2023IPPAX053

Thèse de doctorat

ÉCOLE POLYTECHNIQUE

IP PARIS

SHANGHAI JIAO TONG UNIVERSITY

# Simulation of laser energy deposition with structured light beams in air and machine learning data treatment for LIBS analysis of remote targets

Thèse de doctorat de l'Institut Polytechnique de Paris et de l'Université Jiao Tong de Shanghai
préparée à l'École Polytechnique

École doctorale n°626 Ecole Doctorale de l'Institut Polytechnique de Paris (ED IP Paris)
Spécialité de doctorat: Physique

**LONG ZOU**

Composition du Jury :

| | |
|---|---|
| Aurélien Houard<br>Research scientist, Laboratoire d'Optique Appliquée, ENSTA Paris, Ecole Polytechnique, CNRS, IP Paris, France | Président |
| Stelios Tzortzakis<br>Professor, Texas A & M University at Qatar, FORTH & University of Crete, Greece | Rapporteur |
| Jérome Kasparian<br>Professor, Nonlinearity and Climate Group, Université de Genève, Switzerland | Rapporteur |
| François Courvoisier<br>Directeur de recherche, CNRS, FEMTO-ST Institute, Univ. Bourgogne Franche-Comte, France | Examinateur |
| Tiejun Wang<br>Professor, State Key Laboratory of High Field Laser Physics, SIOM, CAS, China | Examinateur |
| Yanping Chen<br>Professor, Shcool of Physics and Astronomy, Shanghai Jiao Tong University, China | Examinateur |
| Arnaud Couairon<br>Directeur de recherche, CNRS, Ecole Polytechnique, IP Paris, France | Directeur de thèse |
| Jin Yu<br>Professor, School of Physics and Astronomy, Shanghai Jiao Tong University, China | Co-directeur de thèse |

# Acknowledgements

I've finally reached the point in my education when I'm about to graduate and enter the social melting pot. There have been a lot of memorable moments throughout my 22-year journey from elementary school to Ph.D.. I've received a lot of assistance from many people during this time.

I want to start by thanking Yanliang Xu, my elementary school math teacher. Even though I was at the bottom of the class, he motivated me to continue studying and provided me encouragement. Then there was Haifeng Li, a physics instructor from my junior high school. For me, he unlocked the entrance to the fascinating realm of physics for me and helped a lot in my understanding of many physical phenomena. I still recall that afternoon when I witnessed light refracting through a prism and subsequently splitting into colored streaks, which piqued my interest in nature. I would also like to thank my high school teachers, who were very nice. In addition to academic help, they also taught many life lessons. For example, *All study and no play, makes smart kids turn gray* by Fuzhou Wu and *Work hard with your head down, but also look up and around* by Zhangcai Xu. I wish to thank Prof. Wei Ku from Shanghai Jiao Tong University for hosting me in his group at the beginning of my Ph.D., when I've learned a lot about quantum physics.

There is no doubt that the completion of this thesis would not have been possible without the support and assistance of my two supervisors, Prof. Jin Yu from Shanghai Jiao Tong University and Prof. Arnaud Couairon from École Polytechnique. They helped me refine my ideas together, provided physical explanations and suggestions to the calculation results, and finally assisted me in revising and completing the article for submission. They also put in a lot of effort and energy into helping me apply for the short term visiting in France. I sincerely express my gratitude to them. Also I'd like to thank Chen Sun for her assistance in my projects, as well as the discussion and writing of the thesis. She also help me contact a lot of professors and goes through a lot of paperwork as my defense secretary. I want to thank my French teacher Mme. Marie Noëlle, who patiently corrected my oral expression and pronunciation, and led us to experience the diverse culture of France.

I would also like to thank my classmates and friends during my Ph.D., Fengye Chen, Jinning Hou, Ruoshi Jiang, Zijian Lang, Yunfei Rao, Tianyang Sun, Weijie Xu, Zengqi Yue, Xinyao Zhang, Yibei Zhang, Yuqing Zhang and so on. We have spent a very enjoyable time together.

In particular, special thanks to my significant other - Yujia Wu, with whom I have weathered many storms hand in

hand. During my low point in research, thank you for standing by me through thick and thin, and for being my pillars of strength when I needed them the most, encouraging, supporting and accompanying me, ultimately aiding my emergence from the shadows. We share common interests and hobbies, yet truly understand and accommodate each other's differences. Your presence in my life has been a constant source of comfort and inspiration, and I cherish every moment we have spent together.

Finally, I would like to express my gratitude to my family. It is your constant companionship and silent support that have shaped me into the person I am today. Without your unwavering love and encouragement, I would not have come this far on my journey.

# Résumé en français

La propagation d'impulsions laser ultra-courtes et ultra-intenses dans l'atmosphère est de plus en plus étudiée. Un contrôle précis de la focalisation du champ laser et de la distribution des filaments de lumière qui s'étendent au-delà du foyer est nécessaire pour de nombreuses applications, comme la mission d'exploration de Mars qui comprend l'analyse des éléments chimiques à l'aide de la spectroscopie de désintégration induite par laser (LIBS), l'analyse de la composition de l'atmosphère par des techniques de détection et de télémétrie lumineuses (LIDAR), le déclenchement et le guidage de décharges électriques entre les nuages, ou la génération de lasers à lumière blanche par filamentation laser. Un contrôle quantitatif des propriétés de l'impulsion laser est très difficile en raison de l'interaction non-linéaire complexe entre l'impulsion laser intense et le milieu. Actuellement, les méthodes couramment utilisées reposent sur le contrôle des paramètres initiaux de l'impulsion laser en fonction du champ laser observé sur la cible. La grande dimension de l'espace des paramètres et la sensibilité des résultats aux conditions initiales rendent l'ajustement du champ laser hors du laboratoire difficile et inefficace pour répondre aux exigences des applications pratiques.

Dans ce contexte, cette thèse propose une réponse à quelques-uns des défis de la propagation d'impulsions laser femtoseconde à longue portée, basée sur des scénarios de modulation de l'impulsion laser qui garantissent d'atteindre un champ laser sur cible avec les propriétés souhaitées. Ces scénarios ont été obtenus en associant méthodes d'ingénierie inverse et simulations numériques. Nous montrons que différents champs cibles peuvent être facilement et efficacement atteints en modulant le champ en sortie du laser. Chaque fois que cela est possible, la modulation est obtenue par simulation de la propagation inverse du champ cible vers le laser.

Cette thèse se concentre sur deux objectifs différents de contrôle du champ laser : la projection à longue distance dans l'air (1) d'un filament de longueur prédéfinie, et (2) d'une intensité élevée. (1) Pour atteindre le premier objectif, une des innovations de cette thèse consiste à introduire un faisceau intermédiaire contrôlable proche de la cible, de type Bessel-Gauss, et à utiliser un algorithme numérique pour propager ce champ électrique en avant afin d'obtenir la distribution des filaments au point cible ainsi que rétropropager le champ intermédiaire pour obtenir la sortie laser souhaitée. Les paramètres de sortie laser obtenus sont ensuite liés aux caractéristiques du filament (point de départ, longueur, densité), fournissant une carte des paramètres clés définissant l'impulsion laser modulée qui peut être projetée sur le champ cible et le filament désirés. (2) Pour l'objectif de transmission

d'intensités élevées à des distances kilométriques, nous examinons la propagation non-linéaire de faisceaux d'Airy circulaires et montrons qu'une puissance laser de quelques dizaines de GW est suffisante pour ioniser l'air et former un filament court à une distance de 1 km, ce qui pourrait faciliter les conditions de fonctionnement du laser par rapport aux lasers de classe TW utilisés dans les solutions conventionnelles pour projeter des intensités élevées à ces distances.

Dans une étude séparée, nous proposons une amélioration de l'algorithme d'analyse élémentaire du spectre LIBS. L'algorithme est appliqué à la détection en ligne de la teneur en KCl et $H_2O$ dans les engrais potassiques par LIBS, dans lequel la modélisation de régression de corrélation des spectres LIBS est combinée à un algorithme d'apprentissage automatique qui extrait efficacement les informations liées aux changements de contenu élémentaire à partir des spectres en ligne complexes, ce qui améliore considérablement la vitesse de détection tout en garantissant la précision de la détection et renforce encore la compétitivité.

# Contents

# List of Figures

# List of Tables

# Chapter 1 General Introduction

## 1.1 Brief introduction to the development of optics and laser technology

The study of optics can be traced back to 400 $B.C.$, when Chinese scholar Mo Zi first documented the linear propagation of light and the imaging through small holes[1]:

"光之人，煦若射。下者之人也高，高者之入也下。足蔽下光，故成景于上；首蔽上光，故成景于下。在远近有端与于光故景库内也。"

**Figure 1–1 A portrait of Mozi who was a Chinese philosopher and thinker.**

Yet, true scientific research into optics didn't start until the 17th century. At that time, European researchers started to use mathematics and science to attempt to explain light and associated optical phenomena. A renowned experiment demonstrating the dispersion of white light through a prism was carried out by Newton. The observed colorful spectrum of sunlight indeed implies the concept of wavelength. However, Newton thought that light is particle-like, which makes it difficult to explain diffraction phenomena. Disputing Newton's point of view, Huygens argued that light is wave-like. He proposed that *Any point on the moving wavefront can be regarded as a new secondary wave source, and the envelope formed by many secondary waves emitted from various points on the wavefront is the new wave surface to which the original wavefront propagates within a certain period of time.* in his work *Traité de la Lumiere*[2]. Later, Fresnel assumed that these waves would interfere with each other on the basis of Huygens' principle. The presence of the Poisson spot when

light propagates through an opaque plate evidenced the correctness of Fresnel. At this point, the wave theory of light has gradually been accepted, developed and formalized by James C. Maxwell in the 19th century. In 1905, Einstein introduced the concept of photon quanta and the following experiment on photoelectric effect proved the particle nature of light. Because the description of light waves in the Maxwell equations and the photon interpretation were incompatible, physicists were forced to admit that in addition to wave properties, light also has particle properties. The specific form in which light appears depends on the way it is measured.

With the development of quantum physics, T. H. Maiman used ruby as an activation medium to realize the first laser in 1960[3], emitting the first beam that could be applied in practice, opening a new chapter in the history of optics. One year later at the University of Michigan, P. A. Franken *et al.* focused a ruby laser at 694.3 nm into a crystalline quartz and observed the optical second harmonic at 347.15 nm[4]. Although the conversion efficiency is low due to phase mismatch, this work opens up a new direction of research。The earliest theoretical explanation for nonlinear optics was developed by N. Bloembergen *et al.* in 1962[5]. In this paper, they proposed a phase matching technique that provides a theoretical basis for improving the frequency conversion efficiency of the second harmonic process. Since then, other nonlinear effects were also discovered and investigated, such as high harmonic generation, optical parametric amplification and oscillation, electro-optic effect (Pockels or Kerr), multi-photon absorption, supercontinuum generation and stimulated light scattering.

The development of other technologies has promoted the upgrading of lasers, and a variety of lasers have been researched and invented, such as gas lasers, solid-state lasers and Q-switched lasers. The chirped pulse amplification technology[6] that appeared in 1985 brought lasers into a new era of ultra-fast and powerful femtosecond pulses, which benefits the applications based on laser-matter interactions. In this chapter, the motivation of this thesis is presented: to investigate how to facilitate quantitative analysis of remote targets from different aspects. In particular, 1) how to project an ultra-intense laser beam remotely near the target and control its properties such as the ability to deposit high power density. 2) how to process the raw data (spectra) collected under complicated conditions to accomplish quantitative composite analysis. In the sections below, we start with a brief review on the recent advances of laser-based remote sensing especially related to femtosecond filamentation and

laser induced breakdown spectroscopy. Then we introduce the challenges encountered in these studies. Finally, the structure of this thesis is presented.

## 1.2 Research background and motivation of this thesis

Laser-based remote sensing, also known as lidar (light detection and ranging), is a powerful and versatile tool for investigating the physical and chemical properties of the atmosphere, oceans, and land surfaces. This technique utilizes laser beams to measure the distance to a target and analyze the properties of the target based on the characteristics of the returned light. In atmospheric studies, it is used to measure the concentration and distribution of atmospheric gases such as ozone, carbon dioxide, and other chemical compounds. This information is critical for understanding climate change and air quality, as well as for monitoring the effects of pollution and volcanic activity.

Before the first experimental observation of light filamentation in air by Braun *et al.*[7] and other researchers at Laboratoire d'Optique Appliquée[8] in the mid-1990s, it was widely believed that ultrafast and ultra-intense femtosecond laser pulses were not suitable for long-distance transmission in air. A simple estimate shows that the peak intensity of a Gaussian light pulse with a pulse duration of 30 fs and a beam waist radius of 5 mm will drop to $\sim$ 1/5000 of the initial intensity after one kilometer of linear propagation in air due to the combined effects of diffraction and group velocity dispersion[9]. When the beam input power is sufficiently strong, however, the light field appears to self-focus or even collapse as it propagates, and its light intensity grows rather than decreases. The light intensity is clamped in a specific area after the filament - a plasma channel - is formed in the air and will not increase further. The physics of filamentation in air is currently well studied and understood. In essence, due to the dynamic competition between the optical Kerr effect and the plasma defocusing effect, the beam can travel over considerably longer distances than the Rayleigh length without broadening[10]. Multiphoton absorption both allows for the generation of the plasma characterizing the filament and limits the further increase of intensity.

Controlling the deposition of laser energy in the atmosphere is crucial for many applications requiring an accurate quantitative analysis. The peak intensity in the core of the laser pulse induced filament can reach $10^{13}$-$10^{14}$ W/cm$^2$ and is sufficient to cause the breakdown of a solid target, fragmentation of biological molecules or ionization of air molecules located

tens or even thousands of meters away, allowing for remote analysis based on the collected characteristic emission signals[7-8,11-17]. In terms of the femtosecond laser filament-induced breakdown spectroscopy (FIBS) studies, the European Research Program Teramobile team was one of the first to elaborate relevant research. Using a terawatt mobile (Teramobile) laser (10 Hz, 75 fs, 350 mJ, 800 nm) and a telescopic focusing system, Rohwetter *et al.* performed the first FIBS spectroscopy of metallic objects, such as copper and aluminum, at a distance of 25 m in 2003[18].

By changing the chirp of a 250 mJ femtosecond laser pulse, Stelmaszczyk *et al.* were able to identify the LIBS spectra of metal samples at a distance of 90 m in 2004[19]. Later in 2005, the same team employed chirp modulation to excite the LIBS spectral signal of a metallic target at a distance of 180 m using femtosecond laser pulses with a spot diameter of 4.5 cm[20]. Tzortzakis *et al.* employed a 450 fs (5 mJ) laser pulse with a center wavelength in the UV 248 nm in 2006 to propagate filaments in the atmosphere, focusing on a sample at 10 m and exciting the LIBS signal of rocks[21]. In a series of experimental tests including remote FIBS, See Leang Chin's team at Université Laval in Canada successfully detected the LIBS spectra of metals, ethanol, mosquito smoke, organic materials, and aerosols[22]. They discovered that OH and NH fluorescence could be produced in association with water vapor concentration by forming filaments in a foggy atmosphere using femtosecond laser pulses, proving the feasibility of remote measurements of air humidity[23]. In order to improve the LIBS signal and increase the clamping intensity of femtosecond laser filamentation, they worked together in 2012 with Ruxin Li's group at the Shanghai Institute of Optics, Chinese Academy of Sciences[24]. When comparing ultraviolet (266 nm) and near-infrared (795 nm) femtosecond laser filaments, Jean-Claude Diels's team at the University of New Mexico in the United States found that UV filaments are better suited for the excitation of molecular spectral bands and can distinguish clearly between explosive dinitrotoluene DNT and the muddled ammonium salt[25]. In order to show that organic thin-film samples may be found on the surface of a distant target, Martin Richardson and Matthieu Baudelet's team at the University of Central Florida in the USA generated filaments at a distance of 12 m in 2009[26]. In 2019, the team of L.A. Finney at the University of Michigan detected uranium atomic spectral lines and UO molecular bands in a uranium metal target by exciting the target at 10 m with a single femtosecond laser[27]. In 2020 the group enhanced uranium atomic and molec-

ular spectra by optimizing the chirp of the outgoing laser pulse[28]. In 2021, the group used genetic algorithm-assisted wavefront control to improve the efficiency of signal generation in metallic copper FIBS experiments and verified that wavefront control with signal feedback can improve FIBS remote detection performance[29]. Weiwei Liu's team at Nankai University in 2022 detected enhanced nitrogen fluorescence spectra by effectively compensating the scattered light aberration in off-axis reflection systems through free phase plates[30]. In the same year, the team investigated the effect of laser pulse repetition rate on filaments and eliminated the negative effect of slow air relaxation by scanning[31]; the team also explored the effect of atmospheric turbulence on filament-induced fluorescence remote sensing and observed that turbulence led to an increase in the number of filaments and thus enhanced fluorescence emission[32]; in collaboration with a European team, they modulated the high intensity region along the propagation direction by inserting a wire mesh with square cells at the exit of the laser system[33]. In 2023 Weiwei Liu's team measured the onset and length of the filament by means of an acoustic model and experimentally investigated the effect of pulse energy and initial pulse chirp on the filament in air at three different focal lengths ( 10m, 20m and 30m) of focus[34]. In the same year, the group demonstrated a remote detection scheme based on laser filament induced plasma spectroscopy and lidar (FIPS-LIDAR) for the detection and analysis of sodium ions in aerosols[35]. In 2019, Huailiang Xu's team at Jilin University used an 800 nm, 40 fs laser pulse to generate a filament to detect tree bark at 2.5 m, demonstrating that FIBS can directly and rapidly analyze tree species and their growth environment[36]; in 2022 they used femtosecond filament LIBS to detect metal elements in water[37]. The team of Ruxin Li and Tiejun Wang at Shanghai Institute of Optics, Chinese Academy of Sciences in 2018 improved the signal-to-noise ratio of aluminum atomic line detection by inserting a polarizer before the detector to effectively attenuate the continuous background of the FIBS spectrum at 3.8 m[38]; in 2021 they investigated the effect of laser pulse polarization on the intensity of the filament[39]. The team of Jingquan Lin and Xun Gao from Changchun University of Science and Technology conducted a study on the analysis of heavy metal Cr elements in soil using femtosecond LIBS in 2014[40]; in 2019, they analyzed heavy metal Pb elements in soil using dual-pulse laser-induced breakdown spectroscopy with femtosecond filament-nanosecond pulse coupling to improve the detection sensitivity[41]. In 2020, Heping Zeng's team at East China Normal University proposed plasma grating in-

duced breakdown spectroscopy (GIBS)[42]. In 2022, they further developed two-dimensional plasma gratings[43] and used the GIBS technique to analyze the heavy metal element Cr in soil[44].

In addition, through filament-induced fluorescence spectra, remote atmospheric sensing on the chemical composite can be accomplished[22,45-47]. A recent paper by Jiewei Guo *et al.* reported the detection of NaCl aerosol down to 0.32 ppb in air at a distance of 30 m using a femtosecond laser filament with a single pulse energy of 4 mJ[48]. The optical setup was carefully adjusted by the researchers in order to compensate for astigmatism and increase the intensity of the optical filament as well as generated fluorescence, which is directly related to lowering the detection limit. Besides spectroscopy analysis, the induced filament itself can act as a virtual antenna emitting electromagnetic radiations. In 2005, Méchain *et al.* showed that the signal transmission process via plasma channels was achievable between two electrodes separated a few tens of meters. Using femtosecond filamentation in air, H. Michberg *et al.* demonstrated the possibility of launching a steady and robust thermal waveguide structure in air for the transmission of high power continuous wave laser beam beams[49-51]. Ali Reza *et al.* from Moussa N'Gom's Lab proposed a robust approach for free-space optical communication that employs structured light beams combined with a femtosecond filament[52]. They created a quasi-transparent conducting channel for signal transmission by forcing small water droplets in the clouds away from the propagation path via filamentation, which improves the scalability, robustness, and capacity of the free optical channel. The control of the generation of filamentation can also be used to guide the electric discharging between electrodes as well as in the clouds[53-55].

On the other hand, after obtaining the measurement signal, it is also important to model the content from the spectral signal to the substance content by means of data processing. While the generation of plasma by laser-matter interaction, on which LIBS is based, is a complex nonlinear kinetic process, the quantitative analysis efficiency is closely related to the chemical and physical properties of the material. For complex targets, such as soils and rocks, matrix effects become a bottleneck for accurate quantitative analysis[56-57]. Specifically, the chemical matrix effect refers to the difference in the plasma properties, including electron density, temperature, and morphology, due to the difference in laser-matter interaction during the LIBS process when an element to be measured is present in a certain amount in

different matrix materials, which eventually leads to the variation of the characteristic spectral intensity of the element to be measured with the sample matrix components. The physical matrix effect refers to the variation of the LIBS spectrum even if the chemical composition of the target is the same due to the different physical morphology, granularity, roughness, and looseness of the target surface[58]. Therefore, both chemical and physical matrix effects can cause the loss of a single correlation between the intensity of elemental emission spectra and their content in the sample, leading to a ill-posed inverse problem in the inversion from LIBS spectra to elemental content. This is especially true when LIBS is used for direct analysis of raw materials without any pretreatment.

However, there are still many challenges ahead in this field. It is extremely difficult to perform direct measurements and diagnostics using standard optical equipment because of the filament ultra-high intensity as well as its remoteness. With complicated nonlinear effects further involved in laser filamentation, the pulse will be significantly reshaped and undergo self-steepening or/and self-compression of its profile. As a result, it is nearly impossible to directly control the filament and shape it precisely in advance to fulfill the needs for diverse applications. For example, the spatial resolution of filament-based remote sensing is significantly limited by the filament length[59]. Generating and tailoring an intense and short filament remotely is important for the purpose of enhancing the performance of remote sensing. When direct control of the filament is a challenging problem, we can try other methods, such as inverse design.

The variability of the atmospheric conditions can affect the propagation and stability of the laser filament, which leads to fluctuations in the signal strength and quality, making it difficult to obtain accurate and reliable measurements. The complexity of the materials' composition impacts the absorption and scattering properties of the laser beam, making it difficult to interpret the data obtained from remote sensing measurements, particularly in complex environments. Therefore, it is necessary to acquire more sophisticated and efficient data processing algorithms to analyze the large amounts of data generated by remote sensing applications. As will be introduced in Chapter 5 in detail, this will require a combination of advanced statistical and machine learning techniques to extract meaningful information from the data and to provide reliable and accurate results.

## 1.3 Presentation of the chapters

Chapter 1 gave a brief overview of the history of nonlinear optics development, reviewed current laser-based remote sensing research progress and remaining challenges, particularly related to femtosecond filaments, and discussed the need to couple more complex data analysis methods into LIBS technology for online detection. Finally, a summary of this thesis's content, organization, and innovative points is provided as below.

Chapter 2 starts with the description of Maxwell's equations in dielectric media and then introduces the main physical effects involved in the filamentation process, such as diffraction, dispersion, Kerr effect and self-focusing and ionization related processes. The dynamic spatial replenishment model proposed by Mlejnek *et al.* accompanied with a derivation of the nonlinear wave envelope propagation equation is also presented. Finally, several numerical method in solving the wave equation are discussed.

Chapter 3 deals with the implementation of wavefront engineering by inverse design in order to delay and stretch the effect of nonlinear losses while launching a near infrared (NIR) filament to a large distance. The demonstration begins with a succinct overview of previous research on the tailoring of temporal and spatial wavefronts to control filamentation. The reversibility of the filament, which is not guaranteed for any beam, is discussed next. In addition, the key characteristics of the Bessel-Gauss beam and numerous methods for obtaining it will be introduced. It will function as a connection between the laser output and the controllable filament in our research on filament producing and modulation. We will also provide examples of how to apply the concept of inverse design to reverse-engineer the laser output in experiments to achieve simultaneous control of filament locations and length based on this intermediate state.

In Chapter 4, we extend our investigation of the nonlinear propagation of ultra-intense beams. To this end, we select a finite energy ring-Airy beam as the input waveform due to its inherent self-reconstruction and acceleration properties, which aid in reducing the optical device size. Specifically, we study the power dependence of the nonlinear focus and focus on the energy flow of the beam during propagation. Our results demonstrate the feasibility of generating kilometer-scale filaments using a gigawatt laser system.

In Chapter 5, in order to bridge the gap between well-controlled filaments and reliable remote sensing or online analysis in complicated environments, we will show how to do quan-

titative elemental analysis based on LIBS spectra recorded under conditions that are virtually entirely unpredictable. Potash has been selected as the subject of this investigation. After introducing the background of our study, an explanation of how to implement LIBS in potash production lines for spectrum acquisition is given. Comparisons between the outcomes of standard univariate analysis methods versus machine learning-based multivariate analysis methods for the collected spectra are also made. The results indicate that the univariate analysis method of spectral line intensity-element content frequently used in laboratories is no longer applicable to spectra in real situations. It is required to utilize multivariate models based on big data analysis, such as machine learning, in order to extract valid information from enormous volumes of collected spectral data.

Chapter 6 systematically summarizes the main research work and results of this paper。

## Bibliography

[1] 方勇译注. 墨子[M]. 北京: 中华书局, 2022.

[2] HUYGENS C. Traité de la lumière[M]. Paris: Gauthier-Villars, 1920.

[3] MAIMAN T H. Stimulated Optical Radiation in Ruby[J/OL]. Nature, 1960, 187(4736): 493-494. https://doi.org/10.1038/187493a0. DOI: 10.1038/187493a0.

[4] FRANKEN P A, HILL A E, PETERS C W, et al. Generation of Optical Harmonics[J/OL]. Phys. Rev. Lett., 1961, 7: 118-119. https://link.aps.org/doi/10.1103/PhysRevLett.7.118. DOI: 10.1103/PhysRevLett.7.118.

[5] ARMSTRONG J A, BLOEMBERGEN N, DUCUING J, et al. Interactions between Light Waves in a Nonlinear Dielectric[J/OL]. Phys. Rev., 1962, 127: 1918-1939. https://link.aps.org/doi/10.1103/PhysRev.127.1918. DOI: 10.1103/PhysRev.127.1918.

[6] STRICKLAND D, MOUROU G. Compression of amplified chirped optical pulses[J/OL]. Optics Communications, 1985, 56(3): 219-221. https://www.sciencedirect.com/science/article/pii/0030401885901208. DOI: https://doi.org/10.1016/0030-4018(85)90120-8.

[7] BRAUN A, KORN G, LIU X, et al. Self-channeling of high-peak-power femtosecond laser pulses in air[J/OL]. Opt. Lett., 1995, 20(1): 73-75. http://opg.optica.org/ol/abstract.cfm?URI=ol-20-1-73. DOI: 10.1364/OL.20.000073.

[8] NIBBERING E T J, CURLEY P F, GRILLON G, et al. Conical emission from self-guided femtosecond pulses in air[J/OL]. Opt. Lett., 1996, 21(1): 62-64. https://opg.optica.org/ol/abstract.cfm?URI=ol-21-1-62. DOI: 10.1364/OL.21.000062.

[9] COUAIRON A, MYSYROWICZ A. Femtosecond filamentation in transparent media[J/OL]. Physics Reports, 2007, 441(2): 47-189. https://www.sciencedirect.com/science/article/pii/S037015730700021X. DOI: https://doi.org/10.1016/j.physrep.2006.12.005.

[10] QI P, LIN L, SU Q, et al. In-situ visualization of multiple filament competition dynamic during nonlinear propagation of femtosecond laser[J/OL]. Scientific Reports, 2017, 7(1): 10384. https://doi.org/10.1038/s41598-017-10768-2. DOI: 10.1038/s41598-017-10768-2.

[11] LA FONTAINE B, COMTOIS D, CHIEN C Y, et al. Guiding large-scale spark discharges with ultrashort pulse laser filaments[J/OL]. Journal of Applied Physics, 2000, 88(2): 610-615. eprint: https://doi.org/10.1063/1.373710. https://doi.org/10.1063/1.373710. DOI: 10.1063/1.373710.

[12] MÉCHAIN G, COUAIRON A, ANDRÉ Y B, et al. Long-range self-channeling of infrared laser pulses in air: a new propagation regime without ionization[J]. Applied Physics B, 2004, 79: 379-382.

[13] MÉCHAIN G, C.D' Amico, ANDRÉ Y B, et al. Range of plasma filaments created in air by a multi-terawatt femtosecond laser[J/OL]. Optics Communications, 2005, 247(1): 171-180. https://www.sciencedirect.com/science/article/pii/S0030401804011812. DOI: https://doi.org/10.1016/j.optcom.2004.11.052.

[14] RODRIGUEZ M, BOURAYOU R, MÉJEAN G, et al. Kilometer-range nonlinear propagation of femtosecond laser pulses[J/OL]. Phys. Rev. E, 2004, 69: 036607. https://link.aps.org/doi/10.1103/PhysRevE.69.036607. DOI: 10.1103/PhysRevE.69.036607.

[15] KASPARIAN J, SAUERBREY R, CHIN S. The critical laser intensity of self-guided light filaments in air[J]. Appl. Phys. B, 2000, 71: 877-879.

[16] BECKER A, AKÖZBEK N, VIJAYALAKSHMI K, et al. Intensity clamping and re-focusing of intense femtosecond laser pulses in nitrogen molecular gas[J/OL]. Applied Physics B, 2001, 73(3): 287-290. https://doi.org/10.1007/s003400100637. DOI: 10.1007/s003400100637.

[17] XU H, CHENG Y, CHIN S L, et al. Femtosecond laser ionization and fragmentation of molecules for environmental sensing[J/OL]. Laser & Photonics Reviews, 2015, 9(3): 275-293. eprint: https://onlinelibrary.wiley.com/doi/pdf/10.1002/lpor.201400208. https://onlinelibrary.wiley.com/doi/abs/10.1002/lpor.201400208. DOI: https://doi.org/10.1002/lpor.201400208.

[18] ROHWETTER P, YU J, MÉJEAN G, et al. Remote LIBS with ultrashort pulses: characteristics in picosecond and femtosecond regimes[J/OL]. J. Anal. At. Spectrom., 2004, 19: 437-444. http://dx.doi.org/10.1039/B316343A. DOI: 10.1039/B316343A.

[19] STELMASZCZYK K, ROHWETTER P, MÉJEAN G, et al. Long-distance remote laser-induced breakdown spectroscopy using filamentation in air[J/OL]. Applied Physics Letters, 2004, 85(18): 3977-3979. eprint: https://doi.org/10.1063/1.1812843. https://doi.org/10.1063/1.1812843. DOI: 10.1063/1.1812843.

[20] ROHWETTER P, STELMASZCZYK K, WÖSTE L, et al. Filament-induced remote surface ablation for long range laser-induced breakdown spectroscopy operation[J/OL]. Spectrochimica Acta Part B: Atomic Spectroscopy, 2005, 60(7): 1025-1033. https://www.sciencedirect.com/science/article/pii/S0584854705000893. DOI: https://doi.org/10.1016/j.sab.2005.03.017.

[21] TZORTZAKIS S, ANGLOS D, GRAY D. Ultraviolet laser filaments for remote laser-induced breakdown spectroscopy (LIBS) analysis: applications in cultural heritage monitoring[J/OL]. Opt. Lett., 2006, 31(8): 1139-1141. http://opg.optica.org/ol/abstract.cfm?URI=ol-31-8-1139. DOI: 10.1364/OL.31.001139.

[22] CHIN S L, XU H L, LUO Q, et al. Filamentation "remote" sensing of chemical and biological agents/pollutants using only one femtosecond laser source[J/OL]. Applied Physics B, 2009, 95(1): 1-12. https://doi.org/10.1007/s00340-009-3381-7. DOI: 10.1007/s00340-009-3381-7.

[23] YUAN S, WANG T, TERANISHI Y, et al. Lasing action in water vapor induced by ultrashort laser filamentation[J/OL]. Applied Physics Letters, 2013, 102(22): 224102. eprint: https://doi.org/10.1063/1.4809585. https://doi.org/10.1063/1.4809585. DOI: 10.1063/1.4809585.

[24] ZENG B, WANG T J, HOSSEINI S, et al. Enhanced remote filament-induced breakdown spectroscopy with spatio-temporally chirped pulses[J/OL]. J. Opt. Soc. Am. B,

2012, 29(12): 3226-3230. https://opg.optica.org/josab/abstract.cfm?URI=josab-29-12-3226. DOI: 10.1364/JOSAB.29.003226.

[25] MIRELL D, CHALUS O, PETERSON K, et al. Remote sensing of explosives using infrared and ultraviolet filaments[J/OL]. J. Opt. Soc. Am. B, 2008, 25(7): B108-B111. https://opg.optica.org/josab/abstract.cfm?URI=josab-25-7-B108. DOI: 10.1364/JOSAB.25.00B108.

[26] MARTIN J, BAUDELET M, WEIDMAN M, et al. Stand-off detection of organic samples using filament-induced breakdown spectroscopy[C/OL]//KUMAR B V, PRABHAKAR S, ROSS A A, et al. Optics and Photonics in Global Homeland Security V and Biometric Technology for Human Identification VI: vol. 7306. SPIE, 2009: 73060Z. https://doi.org/10.1117/12.820523. DOI: 10.1117/12.820523.

[27] FINNEY L A, SKRODZKI P J, BURGER M, et al. Single-shot, multi-signature remote detection of uranium by filament-induced breakdown spectroscopy[J/OL]. Opt. Lett., 2019, 44(11): 2783-2786. https://opg.optica.org/ol/abstract.cfm?URI=ol-44-11-2783. DOI: 10.1364/OL.44.002783.

[28] BURGER M, SKRODZKI P J, FINNEY L A, et al. Remote Detection of Uranium Using Self-Focusing Intense Femtosecond Laser Pulses[J/OL]. Remote Sensing, 2020, 12(8). https://www.mdpi.com/2072-4292/12/8/1281. DOI: 10.3390/rs12081281.

[29] FINNEY L, LIN J, SKRODZKI P, et al. Filament-induced breakdown spectroscopy signal enhancement using optical wavefront control[J/OL]. Optics Communications, 2021, 490: 126902. https://www.sciencedirect.com/science/article/pii/S0030401821001528. DOI: https://doi.org/10.1016/j.optcom.2021.126902.

[30] TAO S, XIE B, XUE J, et al. Giant enhancement of acoustic and fluorescence emission from an off-axis reflective femtosecond laser filamentation system[J/OL]. Opt. Express, 2022, 30(21): 38745-38752. https://opg.optica.org/oe/abstract.cfm?URI=oe-30-21-38745. DOI: 10.1364/OE.473776.

[31] XUE J, ZHANG N, GUO L, et al. Effect of laser repetition rate on the fluorescence characteristic of a long-distance femtosecond laser filament[J/OL]. Opt. Lett., 2022, 47(21): 5676-5679. https://opg.optica.org/ol/abstract.cfm?URI=ol-47-21-5676. DOI: 10.1364/OL.474317.

[32] LIU J, ZHANG Z, SHANG B, et al. Enhancement of multi-filament generation and filament-induced fluorescence by turbulence[J/OL]. Optics Communications, 2022, 517: 128290. https://www.sciencedirect.com/science/article/pii/S003040182200222X. DOI: https://doi.org/10.1016/j.optcom.2022.128290.

[33] GEINTS Y E, MININA O V, GEINTS I Y, et al. Nonlinear Propagation and Filamentation on 100 Meter Air Path of Femtosecond Beam Partitioned by Wire Mesh[J/OL]. Sensors, 2022, 22(17). https://www.mdpi.com/1424-8220/22/17/6322. DOI: 10.3390/s22176322.

[34] SHANG B, QI P, GUO J, et al. Manipulation of Long-Distance femtosecond laser Filamentation: From physical model to acoustic diagnosis[J/OL]. Optics & Laser Technology, 2023, 157: 108636. https://www.sciencedirect.com/science/article/pii/S0030399222007836. DOI: https://doi.org/10.1016/j.optlastec.2022.108636.

[35] ZHANG Z, ZHANG N, WANG Y, et al. Detection of 1.4 μg/m3 Na+ in aerosol at a 30 m distance using 1 kHz femtosecond laser filamentation in air[J/OL]. Opt. Express, 2023, 31(4): 6464-6474. https://opg.optica.org/oe/abstract.cfm?URI=oe-31-4-6464. DOI: 10.1364/OE.481577.

[36] FU Y, HOU M, ZANG H, et al. Remote discrimination of willow, pine and poplar trees and their growing environments by femtosecond filament-induced breakdown spectroscopy[J/OL]. Spectrochimica Acta Part B: Atomic Spectroscopy, 2019, 155: 107-114. https://www.sciencedirect.com/science/article/pii/S0584854719300254. DOI: https://doi.org/10.1016/j.sab.2019.04.001.

[37] CHEN S, CONG X, CHEN J, et al. Sensing Trace-Level Metal Elements in Water Using Chirped Femtosecond Laser Pulses in the Filamentation Regime[J/OL]. Sensors, 2022, 22(22). https://www.mdpi.com/1424-8220/22/22/8775. DOI: 10.3390/s22228775.

[38] ZHU Z, WANG T J, LIU Y, et al. Polarization-dependent femtosecond laser filamentation in air[J/OL]. Chin. Opt. Lett., 2018, 16(7): 073201. https://opg.optica.org/col/abstract.cfm?URI=col-16-7-073201.

[39] GUO H, DONG X, WANG T J, et al. Polarization dependent clamping intensity inside a femtosecond filament in air[J/OL]. Chin. Opt. Lett., 2021, 19(10): 103201. https://opg.optica.org/col/abstract.cfm?URI=col-19-10-103201.

[40] 高勋 李 刘 宋 郝 林, 杜闯. 基于飞秒激光等离子体丝诱导击穿光谱探测土壤重金属 Cr 元素含量. 2014. https://wulixb.iphy.ac.cn//article/id/58984. DOI: 10.7498/aps.63.095203.

[41] 任佳, 高勋. 飞秒细丝-纳秒激光诱导击穿光谱技术对土壤重金属 Pb 元素检测[J]. 光学精密工程, 2019, 27(5): 1069.

[42] HU M, PENG J, NIU S, et al. Plasma-grating-induced breakdown spectroscopy[J/OL]. Advanced Photonics, 2020, 2(6): 065001. https://doi.org/10.1117/1.AP.2.6.065001. DOI: 10.1117/1.AP.2.6.065001.

[43] HU M, SHI S, YAN M, et al. Femtosecond laser-induced breakdown spectroscopy by multidimensional plasma grating[J/OL]. J. Anal. At. Spectrom., 2022, 37: 841-848. http://dx.doi.org/10.1039/D1JA00376C. DOI: 10.1039/D1JA00376C.

[44] 施沈城, 胡梦云, 张青山, 等. 等离子体光栅诱导击穿光谱检测土壤重金属元素[J]. 中国激光, 2022, 49(13): 1311002.

[45] LI H L, WEI X Y, XU H L, et al. Femtosecond laser filamentation for sensing combustion intermediates: A comparative study[J/OL]. Sensors and Actuators B: Chemical, 2014, 203: 887-890. https://www.sciencedirect.com/science/article/pii/S0925400514007758. DOI: https://doi.org/10.1016/j.snb.2014.06.086.

[46] YUAN S, CHIN S L, ZENG H P. Femtosecond filamentation induced fluorescence technique for atmospheric sensing*[J/OL]. Chinese Physics B, 2015, 24(1): 014208. https://dx.doi.org/10.1088/1674-1056/24/1/014208. DOI: 10.1088/1674-1056/24/1/014208.

[47] XU H L, CHIN S L. Femtosecond Laser Filamentation for Atmospheric Sensing[J/OL]. Sensors, 2011, 11(1): 32-53. https://www.mdpi.com/1424-8220/11/1/32. DOI: 10.3390/s110100032.

[48] GUO J, ZHANG Z, ZHANG N, et al. Sub-ppb aerosol detection at a distance of 30 meters by millijoule femtosecond laser pulse filamentation in air[Z]. 2023. arXiv: 2301.11485 [physics.optics].

[49] JHAJJ N, ROSENTHAL E W, BIRNBAUM R, et al. Demonstration of Long-Lived High-Power Optical Waveguides in Air[J/OL]. Phys. Rev. X, 2014, 4: 011027. https://link.aps.org/doi/10.1103/PhysRevX.4.011027. DOI: 10.1103/PhysRevX.4.011027.

[50] GOFFIN A, LARKIN I, TARTARO A, et al. Optical Guiding in 50-Meter-Scale Air Waveguides[J/OL]. Phys. Rev. X, 2023, 13: 011006. https://link.aps.org/doi/10.1103/PhysRevX.13.011006. DOI: 10.1103/PhysRevX.13.011006.

[51] GOFFIN A, TARTARO A, MILCHBERG H M. Quasi-steady-state air waveguide[Z]. 2023. arXiv: 2302.03510 [physics.optics].

[52] REZA S B A, WANG T, BULDT F, et al. Femtosecond Filament Coupled with Structured Light for Free-Space Optical Communication[J/OL]., 2022. https://www.techrxiv.org/articles/preprint/Femtosecond_Filament_Coupled_with_Structured_Light_for_Free-Space_Optical_Communication/19735534. DOI: 10.36227/techrxiv.19735534.v1.

[53] ACKERMANN R, MÉCHAIN G, MÉJEAN G, et al. Influence of negative leader propagation on the triggering and guiding of high voltage discharges by laser filaments[J/OL]. Applied Physics B, 2006, 82(4): 561-566. https://doi.org/10.1007/s00340-005-2061-5. DOI: 10.1007/s00340-005-2061-5.

[54] ACKERMANN R, STELMASZCZYK K, ROHWETTER P, et al. Triggering and guiding of megavolt discharges by laser-induced filaments under rain conditions[J/OL]. Applied Physics Letters, 2004, 85(23): 5781-5783. eprint: https://doi.org/10.1063/1.1829165. https://doi.org/10.1063/1.1829165. DOI: 10.1063/1.1829165.

[55] HOUARD A, WALCH P, PRODUIT T, et al. Laser-guided lightning[J/OL]. Nature Photonics, 2023. https://doi.org/10.1038/s41566-022-01139-z. DOI: 10.1038/s41566-022-01139-z.

[56] EPPLER A S, CREMERS D A, HICKMOTT D D, et al. Matrix Effects in the Detection of Pb and Ba in Soils Using Laser-Induced Breakdown Spectroscopy[J/OL]. Appl. Spectrosc., 1996, 50(9): 1175-1181. https://opg.optica.org/as/abstract.cfm?URI=as-50-9-1175.

[57] ANZANO J M, VILLORIA M A, RUÍZ-MEDINA A, et al. Laser-induced breakdown spectroscopy for quantitative spectrochemical analysis of geological materials: Effects of the matrix and simultaneous determination[J/OL]. Analytica Chimica Acta, 2006, 575(2): 230-235. https://www.sciencedirect.com/science/article/pii/S0003267006011706. DOI: https://doi.org/10.1016/j.aca.2006.05.077.

[58] XU W, SUN C, TAN Y, et al. Total alkali silica classification of rocks with LIBS: influences of the chemical and physical matrix effects[J/OL]. J. Anal. At. Spectrom., 2020, 35: 1641-1653. http://dx.doi.org/10.1039/D0JA00157K. DOI: 10.1039/D0JA00157K.

[59] QI P, QIAN W, GUO L, et al. Sensing with Femtosecond Laser Filamentation[J/OL]. Sensors, 2022, 22(18). https://www.mdpi.com/1424-8220/22/18/7076. DOI: 10.3390/s22187076.

# Chapter 2 Theoretical basis of femotosecond filamentation in air

The complex process of filamentation involves a variety of nonlinear optical effects, including self-focusing, self-phase modulation, and high-order harmonic generation. The properties of the resulting filaments, such as their number, length, and separation, depend on various factors such as the laser beam parameters, the properties of the medium, and the environmental conditions. Studying the physics of filamentation is important for understanding the fundamental mechanisms of nonlinear optics and for developing new applications of laser-matter interaction.

## 2.1 Maxwell's equations in a dielectric medium

Almost two hundred years ago, the physicist and mathematician James Clerk Maxwell published a series of equations unifying the theories of light and electromagnetism. In a dielectric medium, the equations consist of four parts:

- **Gauss's law**:

$$\nabla \cdot D = \rho_f, \tag{2–1}$$

  it describes the relationship between the density of free charges $\rho_f$ and the induced electric field $E$ or electric displacement $D$.

- **Gauss's law for magnetism**:

$$\nabla \cdot B = 0, \tag{2–2}$$

  it simply states that there is no magnetic analogues of electric charges.

- **Faraday's law**:

$$\nabla \times E = -\frac{\partial B}{\partial t}, \tag{2–3}$$

  it describes that an electric field can be induced by a changing magnetic field $B$.

- **Ampére's law with Maxwell's correction**:

$$\nabla \times H = (J + \frac{\partial D}{\partial t}), \tag{2–4}$$

  where $B = \mu H$, $\mu$ is the permeability of the medium and $J$ the current density of free

charges. In the same way as for Faraday's law, this law states that a magnetic field can be induced by a changing electric field.

Here, we are interested in the case when there is no free charges $\rho_f = 0$ or free current $J = 0$ inside the medium. The electric field displacement $D$ is a function of the electric field $E$:

$$D = \epsilon_0 E + P, \tag{2–5}$$

where $\epsilon_0$ denote the permittivity of vacuum and $P$ the polarization describing the medium response to the electric field. As long as the field is not too strong, we can expand $P$ as a power series of E:

$$\begin{aligned} P &= \epsilon_0[\chi^{(1)}E + \chi^{(2)}E^2 + \chi^{(3)}E^3 + \cdots] \\ &\equiv P^{(1)} + P^{(2)} + P^{(3)} + \cdots \\ &= P^{(1)} + P^{NL}, \end{aligned} \tag{2–6}$$

where $\chi^{(n)}$ denotes the nth-order optical susceptibilities, $P^{(1)} = \epsilon_0\chi^{(1)}E$ and $P^{NL}$ contains all the nonlinear polarization terms. In general, $P^{NL}$ is very small and can be neglected for conventional optics. However, when the laser intensity is high, for example $I \sim 10^{12}$ W/cm$^2$ in air, we have to consider the influence of the nonlinear response of the medium on the propagation of the field.

By applying the curl to Faraday's law, we can get a propagation equation involving only the electric field:

$$l.h.s = \nabla \times (\nabla \times E) = \nabla(\nabla \cdot E) - \nabla^2 E, \tag{2–7a}$$

$$r.h.s = \nabla \times (-\frac{\partial B}{\partial t}) = -\frac{\partial}{\partial t}(\nabla \times B) = -\mu\frac{\partial J}{\partial t} - \mu\frac{\partial^2 D}{\partial t^2}, \tag{2–7b}$$

Regroup the linear and nonlinear terms appearing in the electric displacement $D$ (Eq. (2–5)) as below:

$$\begin{aligned} D &= \epsilon_0 E + P \\ &= \epsilon_0 E + P^{(1)} + P^{NL} \\ &= \epsilon_0(1 + \chi^{(1)})E + P^{NL} \\ &= \epsilon_0\epsilon E + P^{NL}, \end{aligned} \tag{2–8}$$

where $\epsilon = 1 + \chi^{(1)}$ represents the relative permittivity of the medium. Thus, we get the wave equation in space-time domain:

$$\nabla^2 E - \nabla(\nabla \cdot E) - \frac{1}{c^2}\frac{\partial^2}{\partial t^2}\int_{-\infty}^{t} \epsilon(t-t')E(r,t',z)dt' = \mu(\frac{\partial J}{\partial t} + \frac{\partial^2 P^{NL}}{\partial t^2}) \tag{2–9}$$

In linear regime, if the medium is homogeneous, in other words, the permittivity $\epsilon$ and susceptibility $\mu$ of the medium is independent of $(x, y, z)$. Then, the divergence of the electric field vanishes:

$$\nabla \cdot E = 0. \tag{2–10}$$

Hence, the electric wave equation in a homogeneous medium without nonlinearity reads:

$$\nabla^2 E - \frac{n^2}{c^2}\frac{\partial^2 E}{\partial t^2} = 0, \tag{2–11}$$

where $n \equiv \sqrt{\epsilon\mu}$ denotes the refractive index of the medium.

## 2.2 Main physical effects involved in filamentation

### 2.2.1 Diffraction

Diffraction is a universal property for all kinds of waves. It occurs not only as waves circulate around the corners of an obstacle or propagate through an aperture, but also for free propagation in vacuum. A laser beam with a finite transverse size can be considered as a plane wave modulated by a spatial aperture and thus acquires the ability to diffract along the transverse direction. According to Gaussian optics, the wavefront of the beam bends during propagation, and the beam width is enlarged by $\sqrt{2}$ compared to the waist of the beam with a flat spatial phase after it propagates over a distance called the Rayleigh length:

$$z_R = \frac{k w_0^2}{2} = \frac{\pi n_0 w_0^2}{\lambda}, \tag{2–12}$$

where $n_0$ is the refractive index of the medium at wavelength $\lambda$, $w_0$ the beam waist, $k \equiv n_0 k_0 \equiv n_0 2\pi/\lambda$ the wavenumber in the medium. As shown in Fig. 2–1, the spatial phase of the initial beam is flat. The wavefront of the beam gets bent and the curvature becomes nonzero after the light beam propagates over a finite distance. When the wavefront is far away from the source, the on-axis curvature returns to zero again.

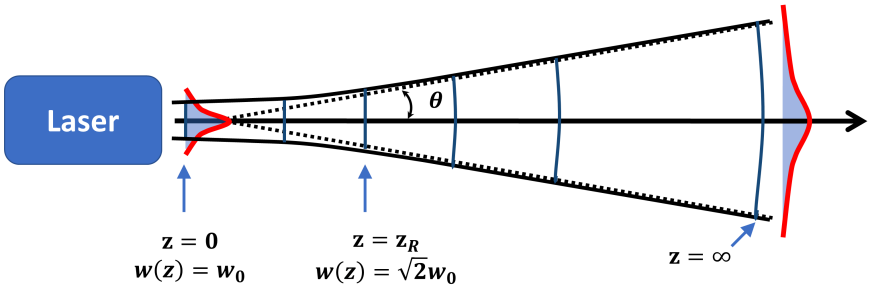


**Figure 2–1 Diffraction of a Gaussian beam from a laser source.**

### 2.2.2 Group velocity dispersion

The dependence of the refractive index $n$ of the medium as a function of wavelength $\lambda$ leads to a phenomenon called dispersion. The classification of normal or anomalous dispersion is determined by the tendency of the refractive index to change (decrease or increase, respectively) as the wavelength increases. For a transparent medium, the dependence between $n$ and $\lambda$ is often described by the Sellmeier formula:

$$n(\lambda) = \sqrt{1 + \sum_j \frac{A_j \lambda^2}{\lambda^2 - B_j}}, \tag{2–13}$$

where the $A_j$ and $B_j$ are empirical coefficients specified after the least squares fitting procedure is applied to experimental measurements[1].

The propagation of a laser pulse in a dispersive medium will exhibit an increase in the duration of the pulse, since every frequency component of the pulse propagates at a different speed. This effect is called group velocity dispersion. For example, lower frequencies travel faster than higher frequencies in normal dispersion media. Thus, after the initial pulse with a flat temporal phase is propagated, redder frequencies will dominate its leading part while bluer frequencies will gather around the trailing part of the pulse envelope. Fig. 2–2 shows how dispersion affects changes in the pulse envelope during propagation.


**Figure 2–2 Broadening of the pulse envelope and frequency shift after a pulse with flat temporal phase propagating through a normal dispersion medium.**

Similar to diffraction, the influence of dispersion on the pulse duration can also be quantified. We define the characteristic length $z_{gvd}$ of group velocity dispersion for a Gaussian pulse with flat temporal phase to be the distance over which linear propagation will result in an increase of the pulse duration by a factor of $\sqrt{2}$:

$$z_{gvd} = \frac{t_p^2}{2k''}, \tag{2–14}$$

where $k'' \equiv \partial^2 k/\partial\omega^2|_{\omega_0}$ is the quadratic Taylor expansion coefficient of wavenumber $k$ as a function of frequency $\omega$ around central frequency $\omega_0$:

$$k(\omega) = \frac{n(\omega)\omega}{c} = \frac{n(\omega_0)\omega_0}{c} + k'(\omega - \omega_0) + \frac{k''}{2}(\omega - \omega_0)^2 + \cdots . \tag{2–15}$$

### 2.2.3 Kerr effect and Self-focusing

When an ultra-intense electromagnetic pulse propagates through an isotropic and centrosymmetric medium, the lowest order of nonlinear response is third order. The change of refractive index of the medium $\Delta n$ due to $\chi^{(3)}$ response is called optical Kerr effect. The magnitude of $\Delta n$ is determined by both the nonlinear refractive index $n_2 = 3\chi^{(3)}/4\epsilon_0 c n_0^2$ and the intensity of the field $I(r,t)$:

$$n = n_0 + \Delta n = n_0 + n_2 I(r,t), \tag{2–16}$$

where $n_0$ is the linear refractive index, $\epsilon_0$ the permittivity of vacuum and $c$ the speed of light.

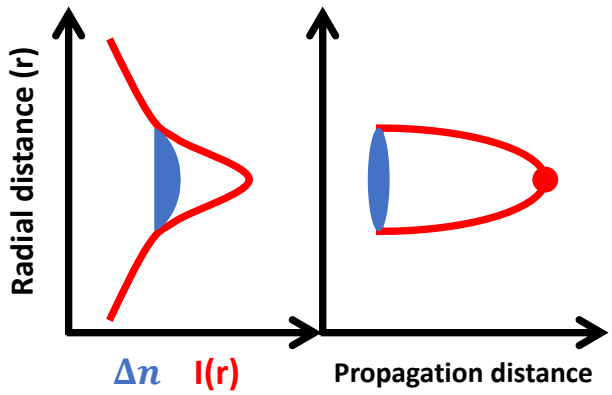


**Figure 2–3 Illustration of optical Kerr effect and self-focusing of a Gaussian beam[2]. The red curve on the right panel represents the beam waist at different propagation distance.**

The nonlinear response of the medium induces additional spatial phase modulation:

$$\phi(x, y, z) \longrightarrow \phi(x, y, z) + \frac{\omega_0}{c} n_2 I(x, y, z) \Delta z. \tag{2–17}$$

For most transparent media, $n_2$ is positive. The additional spatial phase induced by the Kerr effect has negative curvature which is equivalent to a focusing lens. Therefore, an intense Gaussian beam propagating through a Kerr medium will experience higher refractive index in the center than in the outer region and continue to self focus until intensity blows up. As shown in Fig. 2–3, the induced change of refractive index results in focusing of the input Gaussian beam. The competition between Kerr focusing and transverse diffraction can lead to self-trapped propagation for a certain beam power value, or to catastrophic collapse of the beam for larger beam powers[2-3]. The length required for the accumulated nonlinear phase calculated through the $B$-integral ($B \equiv k_0 \int_0^z n_2 I dz$) to reach a value of one represents a characteristic length for Kerr focusing $L_{sf}$ and can be expressed as:

$$L_{sf} = \frac{1}{n_2 k_0 I_0}, \tag{2–18}$$

where $k_0 = 2\pi/\lambda$ and $I_0$ is the peak intensity of the beam. In order to observe self-focusing and collapse of a Gaussian beam, the power of the beam $P_{in}$ should exceed a threshold $P_{cr} = 3.72\lambda^2/8\pi n_0 n_2$[3]. In the case of air molecules, the nonlinear refractive index coefficient $n_2 \approx 3.2 \times 10^{-19}$ cm$^2$/W corresponds to a critical power $P_{cr} = 3$ GW when the laser wavelength $\lambda = 800$ nm[4-5]. Once the Gaussian beam starts to self-focus, it will collapse at distance:

$$z_{sf} = \frac{0.367 z_R}{\sqrt{[(\frac{P_{in}}{P_{cr}})^{1/2} - 0.852]^2 - 0.0219}}, \tag{2–19}$$

in which $z_R$ denotes the Rayleigh length of the beam[3,6]. Note that $z_{sf}$ is the distance measured from the beam waist. With an additional lens in the optical path, the beam will collapse at distance $z'_{sf}$ determined by $z_{sf}$ and the focal length $f$ as expressed below[7]:

$$\frac{1}{z'_{sf}} = \frac{1}{f} + \frac{1}{z_{sf}}. \tag{2–20}$$

### 2.2.4 Photo-ionization

From previous section, we know that self-focusing of the laser beam will result in intensity collapse if $P_{in} > P_{cr}$. This means that in principle, the intensity will continuously

increase without any limitation as the beam size is reducing. However, when the light intensity increases, the medium may be ionized, thereby acting against the increase of light intensity. For ultrashort laser pulses, the main processes of ionization of transparent media consist in multiphoton ionization and tunnel ionization, both in which the electrons are excited from the valence band to the conduction band.

Multiphoton ionization is the process by which bound electrons absorb several injected photons simultaneously and cross the energy gap to gain freedom. This regime occurs when the energy of the photon $\hbar\omega_0$ is smaller than the size of the energy gap $U_i$. In air, the ionization potential $U_i$ is approximately 12 eV considering the oxygen as the first element being ionized. Each photon of a laser beam at $\lambda = 800$ nm possess energy $\hbar\omega_0 = 1.5$ eV. Therefore, it is necessary to have 8 photons in order to reach the ionization gap $U_i$. The corresponding multiphoton ionization rate is thus proportional to $I^8$. Ionization of other constituents of air is negligible when the peak intensity of the laser pulse does not exceed a few tens of TW/cm$^2$, and therefore will not be considered in the simulation in the chapters below[8].

Tunnel ionization occurs when the atomic Coulomb potential is deformed drastically due to the external electric field. It requires higher intensities than multiphoton ionization. It describes the escape or the so-called quantum tunneling of an electron across the highly perturbed potential. A graphical illustration of the difference between multiphoton and tunnel ionization is shown in Fig. 2–4.

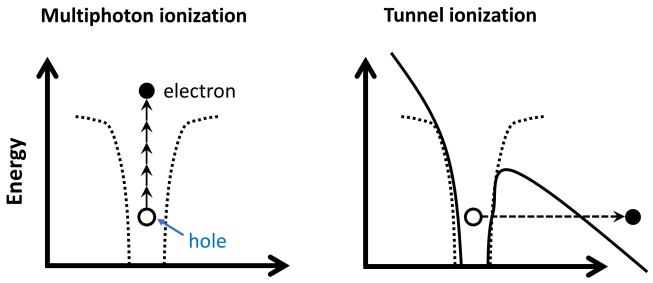


**Figure 2–4 Schematic representation of multiphoton ionization and tunnel ionization[2].**

In order to know when to consider which ionization process occurs, we can calculate the Keldysh parameter $\gamma$:

$$\gamma = \frac{\omega_0}{e}\sqrt{\frac{m_e U_i n_0 c \epsilon_0}{I}}, \tag{2–21}$$

where $I$ is the field intensity. If $\gamma \gg 1$, $I$ is relatively small and multiphoton ionization is

dominant; otherwise the field strength is sufficient to lowr the atomic potential barrier, in which case the main ionization effect would be tunnel ionization. For a filament generated in air by a pulse of peak intensity $I = 5 \times 10^{13}$ W/cm$^2$ at $\lambda = 800$ nm, the value of $\gamma$ is around 1.4. This implies that both ionization effects should be considered in simulations of the filamentation process. However, previous works have shown that simulations based on multiphoton ionization rates fairly reproduce electron densities that can be evaluated from experimental data[9-10]. Therefore, we adopt this approximation in our simulations in the following chapters.

### 2.2.5 Plasma generation and defocusing

Large numbers of highly excited atoms, electrons and ions are generated as the medium is ionized. The evolution of the electron number density is mainly driven by multiphoton ionization and governed by the rate equation:

$$\partial_t \rho = \frac{\sigma}{U_i}\rho I + \frac{\beta^{(K)} I^K}{K\hbar\omega_0} - a\rho^2, \tag{2–22}$$

where $\beta^{(K)}$ is the $K$-photon absorption coefficient, $\sigma$ the cross section for inverse Bremsstrahlung[11]:

$$\sigma = \frac{k_0}{\rho_c}\frac{\omega_0\tau_c}{1+\omega_0^2\tau_c^2}, \tag{2–23}$$

in which $\tau_c$ represents the electron collision time and $\rho_c \equiv \omega_0^2\epsilon_0 m/e^2$ is the critical electron number density above which the plasma becomes overdense and opaque with respect to an electromagnetic radiation of frequency $\omega_0$. Besides multiphoton ionization, we have also considered the weaker phenomena of cascade ionization and radiative recombination in the second and third term of Eq. (2–22), respectively.

The plasma generated through ionization contributes to a reduction of the refractive index of the medium:

$$n(r,t) = n_0 - \frac{\rho(r,t)}{2\rho_c}, \tag{2–24}$$

where $\rho_c$ is the critical electron number density defined previously. This results in defocusing of the incident beam, which competes with the Kerr self-focusing effect and can cause the beam to propagate in the form of a filament.

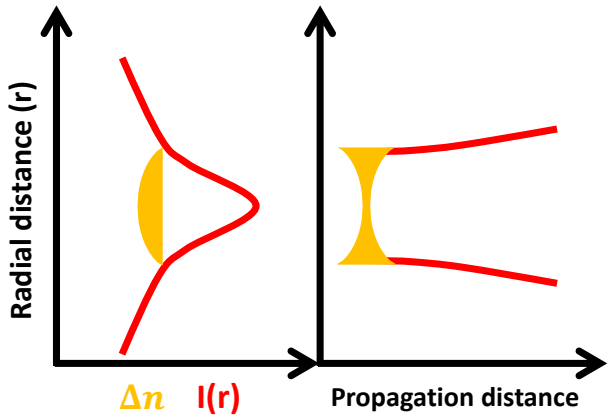


**Figure 2–5 Illustration of defocusing of a beam due to the presence of plasma[2]. The red curve on the right panel represents the beam waist at different propagation distance.**

### 2.2.6 Intensity clamping and dynamic spatial replenishment

The first observations of ultrashort laser pulse filamentation in air by A. Braun *et al*[12] revealed that the pulse energy within an infrared filament is quantized to approximately 1 mJ and that the filament diameter of 100 $\mu$m is fairly constant over extended distances. This suggested a maximum and fairly constant value for the peak intensity of about $5\times10^{13}\mathrm{W/cm^2}$ in air, which was later confirmed by other indirect measurement techniques[13-15].

To explain their observations, Braun *et al*[12] have proposed a phenomenological model based on an equilibrium in the competition between Kerr focusing and plasma defocusing. If these two effects balance each other, the refractive index changes in equations (2–16) and (2–24) cancel each other out, the nonlinear phase accumulation vanishes and the beam curvature no longer evolves. That is:

$$\Delta n = n_2 I - \frac{\rho}{2\rho_c} = 0. \tag{2–25}$$

At this point, the contraction of the beam will stop and the defocusing as well. The light intensity will reach a maximum provided the balance is preserved. Numerous publications on femtosecond laser filamentation reported an absence of increase of the peak intensity within a filament when the laser pulse energy is increased[16-18]. This phenomenon was called Intensity Clamping and constitutes an important physical phenomenon which sets an upper limit of light intensity for the transmission of filament in air and transparent media. An approximate value of $I_c \sim 10^{13} - 10^{14}$ W/cm$^2$ for the clamping intensity can be evaluated from Eq. (2–25)

in fair agreement with the clamping intensity estimated from other measurements[18-20].

However, this agreement must be interpreted with care as the competition between self-focusing and plasma defocusing is dynamic, as shown in 1998 by Mlejnek *et al.* who proposed the dynamic spatial replenishment model[21-22] based on numerical simulation results of filamentation in air. According to the model, an ultrashort laser pulse with peak power in excess of the critical power in air will first undergo self-focusing and an increase of its peak intensity. As a result, plasma will be formed on the rising edge of the pulse, and this plasma will have a defocusing effect on the falling edge of the pulse. On the other hand, multiphoton absorption will also result in a decrease in the rising edge's intensity, which will in turn cause the plasma it produces to become dimmer or even disappear, as well as the defocusing effect it has on the falling edge of the pulse. At this point, self-focusing of the rising edge of the pulse is significantly enhanced and recovers its prior dominance.

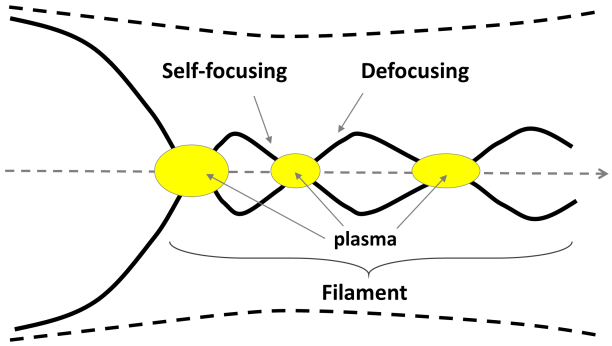


**Figure 2–6 Schematic representation of the Dynamic spatial replenishment model showing the focusing-defocusing cycles during filamentation[2].**

As shown in Fig. 2–6, the dynamic spatial replenishment model can be conceptualized as a pulse cycle of "focusing-defocusing-focusing". This cyclic process will sustain the propagation of the beam until the power of the pulse can no longer support refocusing. Therefore, the high intensity laser beam can propagate over a long distance without being limited by the Rayleigh length.

### 2.2.7 Importance of the energy reservoir

It is necessary to note the importance of the background energy reservoir during filamentation. Previous studies have demonstrated that filamentation will be suppressed in the absence of energy replenishment from the background energy reservoir, as in the case of

using Iris diaphragms to filter the distribution of light fields surrounding the filament[23-27]. There is a dynamic energy exchange between the background energy reservoir and the filament, which provides energy support for the femtosecond filamentation process[28].

## 2.3 Modeling of filamentation

In this section, we will introduce the theoretical model of the propagation of laser pulses in a nonlinear medium.

### 2.3.1 Derivation of the nonlinear envelope equation

It is assumed that the electric field is linearly polarized and can be decomposed into a pulse envelope $\mathcal{E}$ and a rapidly oscillating carrier wave with frequency $\omega_0$:

$$E(x, y, z, t) = \mathcal{E}(x, y, z, t) \exp(ik_0 z - i\omega_0 t) + c.c, \tag{2–26}$$

where $c.c$ represents complex conjugate. It can also be written in the local pulse frame:

$$E(x, y, \zeta, \tau) = \mathcal{E}(x, y, \zeta, \tau) \exp(i(k_0 - \omega_0 v_g)\zeta - i\omega_0 \tau) + c.c, \tag{2–27}$$

where $v_g$ denotes the group velocity, $\zeta = z$ and $\tau = t - z/v_g$.

As introduced in Chapter 2.1, the scalar wave equation in a dielectric medium without source and current is:

$$\nabla^2 E - \frac{n^2}{c^2}\frac{\partial^2 E}{\partial t^2} = 0, \tag{2–28}$$

in which $\nabla^2$ denotes the Laplace operator, in Cartesian coordinate $\nabla^2 \equiv \partial^2/\partial x^2 + \partial^2/\partial y^2 + \partial^2/\partial z^2$; $D$ is the electric displacement:

$$D(x, y, z, \omega) = \epsilon_0(1 + \chi^{(1)}(\omega))E(x, y, z, \omega) + P(x, y, z, \omega), \tag{2–29}$$

where $\epsilon_0$ is the permittivity of vacuum, $\chi^{(1)}(\omega)$ the linear susceptibility of the medium and $P \equiv P^{NL}$ the nonlinear polarization of the medium. Replacing $1 + \chi^{(1)}(\omega)$ with $\epsilon(\omega)$ and bringing expression (2–29) into equation (2–28), we get the following equation:

$$\nabla^2 E - \frac{1}{c^2}\frac{\partial^2}{\partial t^2}\int_{-\infty}^{t} \epsilon(t - t')E(x, y, z, t')dt' = \mu_0 \frac{\partial^2 P}{\partial t^2}, \tag{2–30}$$

where $\epsilon(t)$ is the time representation of material permittivity $\epsilon(\omega)$ and $\mu_0$ the permeability of vacuum. In frequency space, it can be simplified as:

$$\nabla^2 E - \frac{\omega^2 n^2(\omega)}{c^2} E = -\mu_0 \omega^2 P, \tag{2–31}$$

where $\epsilon(\omega) \equiv n^2(\omega)$ defines the complex index of refraction $n(\omega)$.

In order to further distinguish the distribution of the light field propagated along the direction of the transmission axis and the cross-sectional distribution of the light field perpendicular to the direction of the transmission axis, we rewrite the Laplace operator into two parts:

$$\nabla^2 \equiv \frac{\partial^2}{\partial x^2} + \frac{\partial^2}{\partial y^2} + \frac{\partial^2}{\partial z^2} = \Delta_\perp + \frac{\partial^2}{\partial z^2}. \tag{2–32}$$

The wave equation (2–31) is thus becoming:

$$(\Delta_\perp + \frac{\partial^2}{\partial z^2}) E - k^2(\omega) E = -\mu_0 \omega^2 P, \tag{2–33}$$

where $k(\omega) \equiv n(\omega)\omega/c$. In the pulse frame, the partial derivative of $E$ (Eq. (2–27)) to $\zeta$ is:

$$\frac{\partial E}{\partial \zeta} = \exp(i(k_0 - \omega_0/v_g)\zeta - i\omega_0\tau)[\frac{\partial}{\partial \zeta} + i(k_0 - \omega_0/v_g)]\mathcal{E}. \tag{2–34}$$

With this coordinate transformation, we can rewrite the equation (2–31) in the local pulse frame. After considering the decomposition (2–27), removing the fast oscillating part and put the $\omega/v_g$ together with $k_0 - \omega_0/v_g$ to get $\kappa(\omega) = k_0 + (\omega - \omega_0)/v_g$, we have:

$$\frac{\partial^2 \mathcal{E}}{\partial \zeta^2} + 2i\kappa(\omega)\frac{\partial \mathcal{E}}{\partial \zeta} = -\Delta_\perp \mathcal{E} - [k^2(\omega) - \kappa^2(\omega)]\mathcal{E} - \frac{\omega^2}{c^2}\frac{\mathcal{P}}{\epsilon_0}. \tag{2–35}$$

Note that at this stage we do not use any approximation and thus this expression is still exact.

In one optical cycle, if the amplitude of the electric field changes much less than the amplitude itself, that is,

$$\frac{\partial \mathcal{E}}{\partial \zeta} \ll k_0 \mathcal{E}, \tag{2–36}$$

$$\frac{\partial^2 \mathcal{E}}{\partial \zeta^2} \ll k_0 \frac{\partial \mathcal{E}}{\partial \zeta}, \tag{2–37}$$

the first term on the *l.h.s* of Eq. (2–35) can be neglected. This is the so-called Slowly Varying Envelope Approximation (SVEA). Now we are left with:

$$\frac{\partial \mathcal{E}}{\partial \zeta} = \frac{i}{2\kappa(\omega)}\Delta_\perp \mathcal{E} + i\frac{[k^2(\omega) - \kappa^2(\omega)]}{2\kappa(\omega)}\mathcal{E} + \frac{i}{2\kappa(\omega)}\frac{\omega^2}{c^2}\frac{\mathcal{P}}{\epsilon_0}. \tag{2–38}$$

The second term can be further regrouped as:

$$k^2(\omega) - \kappa^2(\omega) = 2\kappa(\omega)[k(\omega) - \kappa(\omega)] + [k(\omega) - \kappa(\omega)]^2, \tag{2–39}$$

We can do a Taylor-expansion of $k_0(\omega) - \kappa(\omega)$ near the central frequency $\omega_0$:

$$k(\omega) - \kappa(\omega)|_{\omega=\omega_0+\Omega} = \sum_{l=2}^{+\infty} \frac{\partial_\omega^l k|_{\omega=\omega_0}}{l!}\Omega^l. \tag{2–40}$$

When $\Omega \equiv \omega - \omega_0$ is very small, the lowest order of the second term on the *r.h.s* of Eq. (2–39) is $O(\Omega^4)$. This implies that it appears as a small correction and can be neglected. Considering this approximation, equation (2–38) becomes:

$$\frac{\partial \mathcal{E}}{\partial \zeta} = \frac{i}{2\kappa(\omega)}\Delta_\perp \mathcal{E} + i[k(\omega) - \kappa(\omega)]\mathcal{E} + \frac{i}{2\kappa(\omega)}\frac{\omega^2}{c^2}\frac{\mathcal{P}}{\epsilon_0}. \tag{2–41}$$

Finally, we approximate $\kappa(\omega) = n_0\omega_0/c = k_0$ on the first and third term of Eq. (2–41). This yields the Nonlinear Envelope Equation in frequency space:

$$\frac{\partial \mathcal{E}}{\partial \zeta} = \frac{i}{2k_0}\Delta_\perp \mathcal{E} + i[k(\omega) - \kappa(\omega)]\mathcal{E} + \frac{i}{2n_0}\frac{\omega_0}{c}\frac{\mathcal{P}}{\epsilon_0}. \tag{2–42}$$

Its space-time counterpart reads:

$$\frac{\partial \mathcal{E}}{\partial \zeta} = \frac{i}{2k_0}\Delta_\perp \mathcal{E} + iD\left(i\partial_\tau\right)\mathcal{E} + \frac{i}{2n_0}\frac{\omega_0}{c}\frac{\mathcal{P}}{\epsilon_0}, \tag{2–43}$$

where $D(i\partial_\tau) = \sum_{l=2}^{+\infty} \frac{k_0^{(l)}}{l!}(i\partial_\tau)^l$. This equation is the basis on which we will conduct our simulations in the following chapters.

## 2.4 Numerical simulation method

Except for a few partial differential equations (PDEs) that can be solved analytically, most of them need to be solved numerically by approximation, especially in the presence of nonlinearities or couplings. And this is exactly the case in my thesis work. As shown in equation (2–44), when an ultrashort intense beam/pulse passes through a dielectric, there is a significant nonlinear response in addition to diffraction and dispersion, which makes it very difficult to solve the wave propagation equations:

$$\partial_z \mathcal{E} = \frac{i}{2k_0}\Delta_\perp \mathcal{E} + iD\left(i\partial_t\right)\mathcal{E} + \frac{i}{2n_0}\frac{\omega_0}{c}\frac{\mathcal{P}\left(\mathcal{E}\right)}{\epsilon_0}. \tag{2–44}$$

In equation (2–44), the polarization term contains all the nonlinear response including the Kerr effect, multiphoton absorption and plasma defocusing, etc. According to the dependence to the electric field, the wave propagation equation can be simplified as below:

$$\partial_z \mathcal{E} = (\mathcal{L} + \mathcal{N})\mathcal{E}, \tag{2–45}$$

where $\mathcal{L} = \frac{i}{2k_0}\Delta_\perp + iD\ (i\partial_t)$ represents the linear differential operator that accounts for diffraction and dispersion, and $\mathcal{N}$ is the general nonlinear operator acting on the electric field. The most straightforward way to solve this equation is using a split-step method. Assuming that operators $\mathcal{L}$ and $\mathcal{N}$ are both independent on $z$, we can solve this equation as an ordinary equation by direct integration and get the solution expressed in operator form:

$$\mathcal{E}(z + dz) = \exp([\mathcal{L} + \mathcal{N}]dz)\mathcal{E}(z). \tag{2–46}$$

This exponential can be expanded by using the *Baker-Hausdorff* formula,

$$\exp([\mathcal{L} + \mathcal{N}]dz) = \exp(\mathcal{L}dz + \mathcal{N}dz + \frac{1}{2}[\mathcal{L}, \mathcal{N}]dz^2 + ...). \tag{2–47}$$

Normally, the operator $\mathcal{L}$ and $\mathcal{N}$ do not commute. But the assumption that only first-order terms are left is sufficient for us to perform accurate and reliable numerical calculations. Thus, equation (2–47) becomes

$$\exp([\mathcal{L} + \mathcal{N}]dz) = \exp(\mathcal{L}dz)\exp(\mathcal{N}dz). \tag{2–48}$$

So equation (2–45) can be rewritten as

$$\mathcal{E}(z + dz) = \exp(\mathcal{N}dz)\exp(\mathcal{L}dz)\mathcal{E}(z). \tag{2–49}$$

When solving this evolution equation, a natural split-step scheme consists in separating linear operators from nonlinear terms. Considering our goal to preserve the reversibility of the numerical scheme in the case of reversible propagation, we symmetrized the split-step scheme, i.e., the field will be propagated half a step linearly, then a full step nonlinearly, and finally the remaining half step linearly:

$$\mathcal{E}(z + dz) = \exp(\mathcal{L}dz/2)\exp(\mathcal{N}dz)\exp(\mathcal{L}dz/2)\mathcal{E}(z). \tag{2–50}$$

The details about the implementation of the algorithm corresponding to different simulation regimes will be illustrated in the following subsections.

### 2.4.1 Pseudo-spectral method

Given a differential equation defined in $\mathbb{R}^d$ which is bounded and closed, $d$ is the space dimension larger than 1. For example, a differential problem with a bounded domain of function could be $\mathcal{L}u(x,z) = g(x,z),\ x \in [x_0, x_1]$. What we would like to do is to seek the solution $u(x,z)$ given a set of initial or boundary conditions. In principle, the operator $\mathcal{L}$ itself could be linear or nonlinear. And we also consider the source term $g(x,z)$ on the right-hand side. For the diffraction of a light beam in vacuum, $\mathcal{L} = \partial_z - \frac{i}{2k_0}\Delta_x$ and $g(x,z) = 0$.

The basic idea of using a spectral method to solve this equation is assuming that we can expand the function $u(x,z)$ as a combination of some basis functions $v(k_x, z)$ with different coefficient $C_k$:

$$u(x,z) = \int_{-\infty}^{+\infty} C_{k_x}(z) v_{k_x}(x) dk_x \approx \sum_{k_x} C_{k_x}(z) v_{k_x}(x) \tag{2–51}$$

In order to do the expansion, we often select basis functions with the following requirements:

1. Convergence: the discrete summation in (2–51) quickly converges to the analytical solution $u(x,z)$ as the number of terms involved increases.
2. Differentiation: Given a set of coefficients $C_{k_x}(z)$ satisfying (2–51), there is always another set of coefficients $C^1_{k_x}(z)$ satisfying the derivative form,

$$\frac{\partial u(x,z)}{\partial x} = \sum_{k_x} C^1_{k_x}(z) v_{k_x}(x). \tag{2–52}$$

3. Transformable: transformation between $u(x,z)$ and $v_{k_x}(x)$ is feasible.

Next we choose two sets of basis functions - trigonometric polynomials and Bessel functions - for further discussions in detail.

#### 2.4.1.1 Cartesian coordinates - Fourier transform

We start with the simplest 1D propagation equation with periodic boundary conditions, in which the operator $\mathcal{L} = \partial_z - \partial_{xx}$ without source term - $g(x,z) = 0$,

$$\partial_z u(x,z) = D\partial_{xx} u(x,z), \tag{2–53}$$

where $D = \frac{i}{2k_0}$ represents the diffraction coefficient. We decompose the function $u(x,z)$ using trigonometric polynomials. Thus, the transformation operating on trigonometric poly-

nomials results in its Fourier modes.

$$u\left(k_x, z\right) = \int_{-\infty}^{+\infty} u\left(x, z\right) \exp\left(-ik_x x\right) dx. \tag{2–54}$$

After the Fourier transform of equation (2–53) using (2–54), we obtain:

$$\partial_z u\left(k_x, z\right) = D\left(-k_x^2\right) u\left(k_x, z\right). \tag{2–55}$$

Integrate (2–55) on $z$ leading to the solution of $u\left(k_x, z\right)$:

$$u\left(k_x, z\right) = u\left(k_x, 0\right) \exp\left(-Dk_x^2 z\right). \tag{2–56}$$

Finally, the real space distribution $u\left(x, z\right)$ is calculated by taking the inverse Fourier transform on equation (2–56).

$$u\left(x, z\right) = \frac{1}{2\pi} \int_{-\infty}^{+\infty} u\left(k_x, z\right) \exp\left(ik_x x\right) dk_x. \tag{2–57}$$

Restate the necessary step involved, first we need to Fourier transform the initial condition $u\left(x, 0\right)$ into its representation in the spatial frequency space $u\left(k_x, 0\right)$, and multiply it with a phase factor $\exp\left(-Dk_x^2 z\right)$, finally we apply the inverse Fourier transform to the result so as to obtain $u\left(x, z\right)$. The method can be simply extended to higher dimensions.

#### 2.4.1.2 Cylindrical coordinates - Hankel transform

For the case in 2D where we have rotational symmetry around the $z$-axis, we can choose a more appropriate set of basis functions to reduce the cost of doing 2D Fourier transforms.

The operator $\mathcal{L} = \partial_z - \partial_{xx} - \partial_{yy}$, again without source term $g\left(x, y, z\right) = 0$. Following a similar procedure as in equation (2–53), we write the wave propagation equation in Cartesian coordinates as well as in Cylindrical coordinates:

$$\partial_z u\left(x, y, z\right) = D\left(\partial_{xx} + \partial_{yy}\right) u\left(x, y, z\right), \tag{2–58}$$

$$\partial_z u\left(r, z\right) = D\left(\partial_{rr} + \frac{1}{r}\partial_r\right) u\left(r, z\right). \tag{2–59}$$

If the set of basis functions is chosen to be the Bessel functions $j_\nu(k_r r)$, in the case of (2–59) the order of Bessel function is just $\nu = 0$.

The Hankel transform of order 0 and its inverse is defined as follows:

$$\bar{u}\left(k_r\right) \equiv H_0 u\left(r\right) = \int_{-\infty}^{+\infty} u\left(r\right) j_0\left(k_r r\right) r dr, \tag{2–60}$$

$$u\left(r\right) \equiv H_0^{-1} \bar{u}\left(k_r\right) = \int_{-\infty}^{+\infty} \bar{u}\left(k_r\right) j_0\left(k_r r\right) k_r dk_r. \tag{2–61}$$

The procedure to get $u\left(r, z\right)$ is almost the same as in previous sections. First, we need to apply a Hankel transform to the initial condition $u\left(r, 0\right)$ so as to obtain its representation in the frequency space $\bar{u}\left(k_r, 0\right)$, and multiply it with the phase factor $\exp\left(-Dk_r^2 z\right)$, finally we take the inverse Hankel transform of the result to get $u\left(r, z\right)$.

### 2.4.2 Finite difference method

In addition to the above methods, partial differential equations can also be solved using finite differences defined on discrete space variables. If we define the function $u \equiv u\left(x\right)$, where $x$ in $[x_1, x_2, \ldots x_n]$ denoting the set of discrete points which are usually uniformly distributed. Then the approximation of the exact solution of $u\left(x\right)$ is taken by the value $u\left(x_1\right)$, $u\left(x_2\right)$, $\ldots u\left(x_n\right)$, or in short-hand notation, $u_1$, $u_2$, $\ldots u_n$. The Taylor expansion of $u\left(x_0 + dx\right)$ around $x_0$ when $dx \rightarrow 0$ is

$$u\left(x_0 + dx\right) = u\left(x_0\right) + \left.\frac{du}{dx}\right|_{x=x_0} dx + O\left(dx^2\right). \tag{2–62}$$

The corresponding discretized version replace $dx$ by the constant step size $h = x_n - x_{n-1}$, the notation for $u$ and its derivative

$$u_{n+1} = u_n + hu_n' + O\left(h^2\right) = u_n + hf(x_n, u_n). \tag{2–63}$$

The finite difference method is a numerical technique used to update the value of $u_{n+1}$ based on the previous distribution of $u_n$. This method can be implemented in different ways, including explicit and implicit methods. The explicit method computes the system state at the next time directly from the known system state, with no coupling between different moments. In contrast, the implicit method considers both the current and future system states to determine the system states at future times. In other words, the implicit method requires the solution of a system of equations, while the explicit method does not.

Stability is an important consideration in the finite difference method. In general, implicit methods are more stable than explicit methods, but they are also more computationally expensive. Explicit methods are subject to stability constraints, which limit the step size $h$ that can be used. If $h$ is too large, the solution may become unstable and the method will fail to converge. On the other hand, implicit methods are unconditionally stable, which means that the step size can be chosen independently of the problem parameters. However, the computational cost of solving the system of equations required by implicit methods can be prohibitively high for some applications. The choice between explicit and implicit methods depends on the specific problem being solved and the computational resources available. Here, the method shown in (2–63) is an explicit method since it only involves the current step.

#### 2.4.2.1 Implicit Crank-Nicolson algorithm

We take equation (2–53) as an example to show the flow of the Crank-Nicolson method. First, approximate the $z$ derivative on the left-hand side at $\left(x_j = jdx, z_n = ndz\right)$:

$$\frac{\partial u}{\partial z}|_{x=x_j,z=z_n} \approx \frac{u_j^{n+1} - u_j^n}{dz}. \tag{2–64}$$

Then the diffraction part on the right-hand side at the same position:

$$D\frac{\partial^2 u}{\partial x^2}|_{x=x_j,z=z_n} \approx \frac{D}{2dx^2}(u_{j+1}^n - 2u_j^n + u_{j-1}^n + u_{j+1}^{n+1} - 2u_j^{n+1} + u_{j-1}^{n+1}). \tag{2–65}$$

Replacing the corresponding terms in (2–53) with (2–64) and (2–65), define $\sigma \equiv \frac{Ddz}{2dx^2}$ and regroup them according to indices $j$ and $n$,

$$-\sigma u_{j-1}^{n+1} + (1+2\sigma)\, u_j^{n+1} - \sigma u_{j+1}^{n+1} = -\sigma u_{j-1}^n + (1+2\sigma)\, u_j^n - \sigma u_{j+1}^n. \tag{2–66}$$

Combined with initial condition $u_x^0 = u\,(x, 0)$ and the Neumann boundary condition

$$\frac{u_1^n - u_{-1}^n}{2dx} = 0, \tag{2–67a}$$

$$\frac{u_j^n - u_{j-2}^n}{2dx} = 0, \tag{2–67b}$$

we can solve (2–66) to simulate the diffraction of the field $u(x, z)$ in vacuum using the Crank-Nicolson method.

### 2.4.3 Runge-Kutta method

The idea of the Runge-Kutta(RK) method is to split the full-step $h$ in (2–63) into several sub-steps as shown in Fig. 2–7

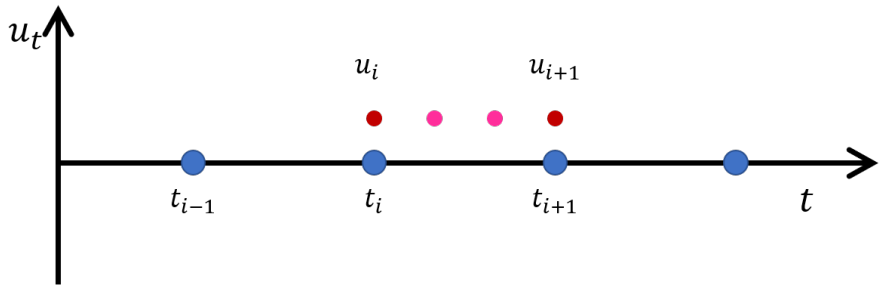


**Figure 2–7 Demonstration of RK4 method: the initial one-step calculation of the field evolution is now decomposed into four repeated evaluations, this result in a higher order approximation of $u$. Here the field changes with time $t$.**

Here we just introduce the most widely used variation of Runge-Kutta method: RK4. As the name suggested, it involves terms with 4th order in the Taylor expansion (2–63) which means the accuracy is $O\left(h^4\right)$. With a given full-step size $h$, the evolution of field $u$ is written as:

$$u_{n+1} = u_n + \frac{1}{6}h\left(k_1 + 2k_2 + 2k_3 + k_4\right) \tag{2–68}$$

For each step $n = 0, 1, 2, 3\ldots$

$$k_1 = f\left(x_n,\ u_n\right), \tag{2–69a}$$

$$k_2 = f\left(x_n + \frac{h}{2}, u_n + h\frac{k_1}{2}\right), \tag{2–69b}$$

$$k_3 = f\left(x_n + \frac{h}{2}, u_n + h\frac{k_2}{2}\right), \tag{2–69c}$$

$$k_4 = f\left(x_n + h, u_n + hk_3\right), \tag{2–69d}$$

where function $f\left(x,\ u\right)$ is defined in (2–63). The method is integrated in a split-step algorithm for solving nonlinear wave propagation equations to deal with nonlinear terms concerning the Kerr effect, multiphoton absorption and plasma-related phenomena.

## Bibliography

[1] SELLMEIER W. Zur Erklärung der abnormen Farbenfolge im Spectrum einiger Substanzen[J]. Annalen der Physik, 1871, 219(6): 272-282.

[2] COUAIRON A, MYSYROWICZ A. Femtosecond filamentation in transparent media[J/OL]. Physics Reports, 2007, 441(2): 47-189. https://www.sciencedirect.com/science/article/pii/S037015730700021X. DOI: https://doi.org/10.1016/j.physrep.2006.12.005.

[3] MARBURGER J. Self-focusing: Theory[J/OL]. Progress in Quantum Electronics, 1975, 4: 35-110. https://www.sciencedirect.com/science/article/pii/0079672775900038. DOI: https://doi.org/10.1016/0079-6727(75)90003-8.

[4] SHIMOJI Y, FAY A T, CHANG R S F, et al. Direct measurement of the nonlinear refractive index of air[J/OL]. J. Opt. Soc. Am. B, 1989, 6(11): 1994-1998. https://opg.optica.org/josab/abstract.cfm?URI=josab-6-11-1994. DOI: 10.1364/JOSAB.6.001994.

[5] NIBBERING E T J, GRILLON G, FRANCO M A, et al. Determination of the inertial contribution to the nonlinear refractive index of air, N2, and O2 by use of unfocused high-intensity femtosecond laser pulses[J/OL]. J. Opt. Soc. Am. B, 1997, 14(3): 650-660. https://opg.optica.org/josab/abstract.cfm?URI=josab-14-3-650. DOI: 10.1364/JOSAB.14.000650.

[6] DAWES E L, MARBURGER J H. Computer Studies in Self-Focusing[J/OL]. Phys. Rev., 1969, 179: 862-868. https://link.aps.org/doi/10.1103/PhysRev.179.862. DOI: 10.1103/PhysRev.179.862.

[7] TALANOV V I. Focusing of Light in Cubic Media[J]. Soviet Journal of Experimental and Theoretical Physics Letters, 1970, 11: 199.

[8] COUAIRON A, BERGÉ L. Light Filaments in Air for Ultraviolet and Infrared Wavelengths[J/OL]. Phys. Rev. Lett., 2002, 88: 135003. https://link.aps.org/doi/10.1103/PhysRevLett.88.135003. DOI: 10.1103/PhysRevLett.88.135003.

[9] COUAIRON A, TZORTZAKIS S, BERGÉ L, et al. Infrared femtosecond light filaments in air: simulations and experiments[J/OL]. J. Opt. Soc. Am. B, 2002, 19(5): 1117-1131. https://opg.optica.org/josab/abstract.cfm?URI=josab-19-5-1117. DOI: 10.1364/JOSAB.19.001117.

[10] MYSYROWICZ A, COUAIRON A, KELLER U. Self-compression of optical laser pulses by filamentation[J/OL]. New Journal of Physics, 2008, 10(2): 025023. https://dx.doi.org/10.1088/1367-2630/10/2/025023. DOI: 10.1088/1367-2630/10/2/025023.

[11] FEIT M D, FLECK J A. Effect of refraction on spot-size dependence of laser-induced breakdown[J/OL]. Applied Physics Letters, 1974, 24(4): 169-172. eprint: https://doi.org/10.1063/1.1655139. https://doi.org/10.1063/1.1655139. DOI: 10.1063/1.1655139.

[12] BRAUN A, KORN G, LIU X, et al. Self-channeling of high-peak-power femtosecond laser pulses in air[J/OL]. Opt. Lett., 1995, 20(1): 73-75. http://opg.optica.org/ol/abstract.cfm?URI=ol-20-1-73. DOI: 10.1364/OL.20.000073.

[13] CORSI C, TORTORA A, BELLINI M. Mutual coherence of supercontinuum pulses collinearly generated in bulk media[J/OL]. Applied Physics B, 2003, 77(2): 285-290. https://doi.org/10.1007/s00340-003-1184-9. DOI: 10.1007/s00340-003-1184-9.

[14] CHIN S L, CHEN Y, KOSAREVA O, et al. What is a filament?[J/OL]. Laser Physics, 2008, 18(8): 962-964. https://doi.org/10.1134/S1054660X08080070. DOI: 10.1134/S1054660X08080070.

[15] CHIN S L. Femtosecond Laser Filamentation[M]. New York: Springer, 2010.

[16] LIU W, HOSSEINI S A, LUO Q, et al. Experimental observation and simulations of the self-action of white light laser pulse propagating in air[J/OL]. New Journal of Physics, 2004, 6(1): 6. https://dx.doi.org/10.1088/1367-2630/6/1/006. DOI: 10.1088/1367-2630/6/1/006.

[17] AKÖZBEK N, SCALORA M, BOWDEN C, et al. White-light continuum generation and filamentation during the propagation of ultra-short laser pulses in air[J/OL]. Optics Communications, 2001, 191(3): 353-362. https://www.sciencedirect.com/science/article/pii/S0030401801011130. DOI: https://doi.org/10.1016/S0030-4018(01)01113-0.

[18] CHIN S L, LIU W, THÉBERGE F, et al. Some Fundamental Concepts of Femtosecond Laser Filamentation[M/OL]//Progress in Ultrafast Intense Laser Science III. Berlin, Heidelberg: Springer Berlin Heidelberg, 2008: 243-264. https://doi.org/10.1007/978-3-540-73794-0_12. DOI: 10.1007/978-3-540-73794-0_12.

[19] KASPARIAN J, SAUERBREY R, CHIN S. The critical laser intensity of self-guided light filaments in air[J]. Appl. Phys. B, 2000, 71: 877-879.

[20] MITRYUKOVSKIY S I, LIU Y, HOUARD A, et al. Re-evaluation of the peak intensity inside a femtosecond laser filament in air[J/OL]. Journal of Physics B: Atomic, Molecular and Optical Physics, 2015, 48(9): 094003. https://dx.doi.org/10.1088/0953-4075/48/9/094003. DOI: 10.1088/0953-4075/48/9/094003.

[21] MLEJNEK M, WRIGHT E M, MOLONEY J V. Dynamic spatial replenishment of femtosecond pulses propagating in air[J]. Opt. Lett., 1998, 23(5): 382-384.

[22] MLEJNEK M, WRIGHT E, MOLONEY J. Moving-focus versus self-waveguiding model for long-distance propagation of femtosecond pulses in air[J]. IEEE Journal of Quantum Electronics, 1999, 35(12): 1771-1776. DOI: 10.1109/3.806580.

[23] NIBBERING E T J, CURLEY P F, GRILLON G, et al. Conical emission from self-guided femtosecond pulses in air[J/OL]. Opt. Lett., 1996, 21(1): 62-64. https://opg.optica.org/ol/abstract.cfm?URI=ol-21-1-62. DOI: 10.1364/OL.21.000062.

[24] BRODEUR A, CHIEN C Y, ILKOV F A, et al. Moving focus in the propagation of ultrashort laser pulses in air[J/OL]. Opt. Lett., 1997, 22(5): 304-306. https://opg.optica.org/ol/abstract.cfm?URI=ol-22-5-304. DOI: 10.1364/OL.22.000304.

[25] COURVOISIER F, BOUTOU V, KASPARIAN J, et al. Ultraintense light filaments transmitted through clouds[J/OL]. Applied Physics Letters, 2003, 83(2): 213-215. eprint: https://doi.org/10.1063/1.1592615. https://doi.org/10.1063/1.1592615. DOI: 10.1063/1.1592615.

[26] DUBIETIS A, GAIŽAUSKAS E, TAMOŠAUSKAS G, et al. Light Filaments without Self-Channeling[J/OL]. Phys. Rev. Lett., 2004, 92: 253903. https://link.aps.org/doi/10.1103/PhysRevLett.92.253903. DOI: 10.1103/PhysRevLett.92.253903.

[27] DUBIETIS A, KUČINSKAS E, TAMOŠAUSKAS G, et al. Self-reconstruction of light filaments[J/OL]. Opt. Lett., 2004, 29(24): 2893-2895. http://opg.optica.org/ol/abstract.cfm?URI=ol-29-24-2893. DOI: 10.1364/OL.29.002893.

[28] KANDIDOV V P, KOSAREVA O G, KOLTUN A A. Nonlinear-optical transformation of a high-power femtosecond laser pulse in air[J/OL]. Quantum Electronics, 2003, 33(1): 69. https://dx.doi.org/10.1070/QE2003v033n01ABEH002366. DOI: 10.1070/QE2003v033n01ABEH002366.

# Chapter 3 Simultaneous control of fs filament position and length in the air

In previous chapters, We reviewed briefly the history and basic concepts of nonlinear optics. Particularly, we have introduced the physical effects related to filamentation. This process requires a powerful laser pulse to ionize the medium along the path of propagation, thereby forming plasma channels, also known as optical filament. Filament properties are highly dependent on the laser initial conditions as well as the environment. Due to the highly nonlinear nature of its generation, a filament is difficult to manipulate. Prior research discussed below has tailored either the spatial or temporal distribution of the input wavefront in order to achieve the objective of regulating the position or length of the generated filament. The simultaneous control of the position and length of an optical filament is still a challenge requiring further research. This is what we will address in this chapter from the perspective of numerical simulation.

## 3.1 Controllability of filament

Filament control refers to regulating its spatial position along the propagation axis, intensity distribution, length, plasma density, and even the formation of multiple filaments. Research efforts in the generation, characterization and optimization of filaments at a remote distance and over a large extent in the atmosphere have been conducted intensively over the last two decades, highlighted notably by an observation of vertical propagation at an altitude of 20 km, of the supercontinuum white light generated by filaments formed at a distance estimated at 2 km above the laser[1], and a direct evidence of plasma channels associated to filaments horizontally propagating at a distance exceeding 1 km from the laser[2]. Simple waveform and wavefront modulations of the output pulses of a CPA laser by respectively group velocity dispersion (GVD) pre-compensation and beam collimation by telescope were applied to push the filament starting position to the largest possible distance[3-5]. Air pressure has also been found to affect the onset of filament; however, its length is almost invariant[6-8]. More recent experimental as well as theoretical efforts have been focused on the generation of long and stable laboratory scale filaments.

Wavefront reshaping was introduced using a deformable mirror[9-10] and optimized by a genetic algorithm[11] to increase the filament length and control the filament pattern with an optimized manipulation of the energy reservoir[12]. The model of an energy reservoir surrounding and dynamically replenishing a filament[12] has inspired other works, demonstrating the prevailing role of nonlinear losses in the robustness of filaments, acting as a sink of energy in the high intensity core of the beam and driving a conical energy flux from the low intensity tails that refills and sustains the filament[13-16]. A spontaneous emergence of such energy flux toward the filament is exemplified by the nonlinear propagation of a Bessel-Gauss beam showing an effectiveness in generating a long and stable filament in spite of nonlinear losses[17-20].

An approach with a Gaussian beam surrounded in a suitable way, by a ring auxiliary beam, leads to a significant protraction of the filament length[21-22]. A similar physical process relying on the nonlinear propagation of Bessel-Gauss beams, albeit in the tight focusing regime, was applied to generate long aspect ratio plasma channels in the bulk of dielectric media. Their subsequent evolution into void through channels[23] presents a significant interest for micromachining applications[24-28].

## 3.2 Reversibility of filamentation

For an ultrashort intense laser pulse undergoing filamentation with a significant ionization loss, the reversibility has been expressly demonstrated to be valid for specific wavefronts[29]. However, as mentioned in Ref. [30], *the reversibility ensures neither that any arbitrary pulse shape can readily be backpropagated, nor that it will follow a filamentary path during its backpropagation.* As an example, we simulated the forward and backward propagation of a Gaussian pulse centered at 775 nm, with beam waist of 0.7 mm and pulse duration 170 fs. The peak input power is 3.5 GW. The nonlinear refractive index $n_2 = 5.57 \times 10^{-23}$ m$^2$/W giving rise to the critical power of the medium $P_{cr} \sim 1.7$ GW. The model used in the simualtion considers diffraction, dispersion, Kerr effect, plasma defocusing and loss and MPA. The intensity first rises as the pulse moves forward, primarily as a result of self-focusing. Next, other high-order nonlinearities become involved, which causes the intensity to saturate. Finally, the beam diffracts, and the intensity progressively decreases. At $z = 8$m, the simulation came to an end. The wavefront calculated at this location is then

used and propagated backward. Even if nonlinear losses act as nonlinear gain during backward propagation, no significant deviation from the wavefront forward evolution history is observed. As shown in Fig. 3–1, the field can indeed propagate back to its initial condition with only a very slight variation of less than 0.1 percent after passing through the highly nonlinear region.

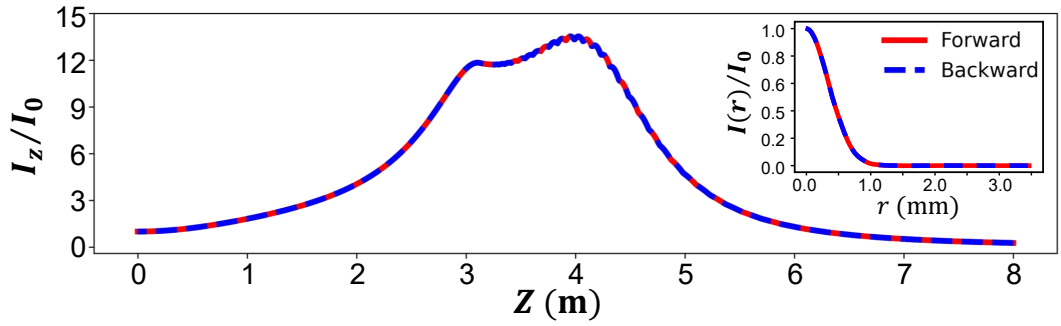


**Figure 3–1 Forward and backward propagation of a laser filament. The on-axis intensity is plotted as a function of propagation distance. The inset shows the comparison between the spatial intensity profile and calculated result through backward propagation.**

For an arbitrary wavefront, the nonlinear loss, being turned into a gain for backward propagation, may lead to a divergence of the simulation. Berti *et al.* proposed an elegant strategy to overcome this problem, based on backpropagation of a hybrid laser pulse that combines a post-filamented pulse with a target waveform, allowing the synthesis of a waveform in the post-filament region, with desired features for a specific application[30].

In the present work, rather than reaching a specific waveform at a given distance after a filament, our goal is to control the features of the target pulse that will subsequently undergo filamentation over a predefined length. Therefore, in our numerical simulation, we chose an intermediate state pulse with a Gaussian beam intensity profile and a linear phase along the radial coordinate. Their amplitude and phase are optimized to avoid ionization while backpropagating toward the position of the initial pulse (output of the laser), therefore preventing the potential divergence triggered by the nonlinear gain and guaranteeing the validity of reversibility. The waveform obtained after backpropagation can be further approximated by an analytical expression which can be characterized by a couple of control parameters.

With the above forward and backward propagation of the intermediate state, the results of the numerical simulations relate the characteristics of the filament to the control parameters of the intermediate state and then to those of the initial pulse. Scaling laws are extracted by

fitting the simulation results. Finally, a thorough forward propagation from the initial state to the final filament is performed to validate the scaling laws derived for the filament length as a function of the projection distance and the characteristics of the initial state.

## 3.3 A brief introduction to Bessel-Gauss beams

The Bessel-Gauss beam is a unique laser beam with distinctive properties that make it useful for a wide range of scientific and technical applications. This beam is a combination of two different beam types: the Bessel beam and the Gaussian beam. The Bessel beam is an invariant of the paraxial propagation equation. It is a non-diffracting, localized beam that keeps its intensity profile over a long distance. Gaussian beams, on the other hand, have a bell-shaped intensity distribution that spreads out as they propagate. It is one of many common output modes for lasers. An ideal Bessel beam is an exact analytical solution of the Helmholtz equation carrying an infinite amount of energy, due to its weakly decaying tail. Thus it cannot be implemented in the laboratory unless a truncation is applied. In the case of the truncation of a Bessel beam $J_0(\beta r)$ by a large Gaussian beam, the resultant beam is the so-called Bessel-Gauss beam of zero-order:

$$E(r,0) = AJ_0(\beta r)\exp(-\frac{r^2}{w_0^2}), \tag{3–1}$$

where $A$ is the amplitude of the field, $\beta$ is equivalent to a transverse wave vector and $w_0$ is the width of the Gaussian beam. By combining the features of these two beams, the Bessel-Gauss beam can produce a large depth of field while keeping a high level of focus. This makes it suitable for a wide range of applications, including microscopy, optical trapping, and laser cutting. In particular, we are interested in the Bessel-Gauss beam because of its capacity to produce a stable and uniform filament. The distance over which the beam remains in focus is referred to as the depth of field. The depth of field with classic Gaussian beams is rather limited due to diffraction, and the beam begins to spread out after a given distance. This limits its applicability in applications requiring a great depth of field, such as microscopy. Bessel beams, on the other hand, are non-diffracting beams that may retain their intensity profile over long distances, resulting in a large depth of field. The Bessel beam can be regarded as a result of the interference of infinite number of plane waves whose wavevector circulates around the propagation $z$-axis at an angle $\theta$. Limited by the size of the optical aperture, the

laboratory achievable Bessel beam is always truncated.

$$z_{\max} \approx R/\tan\theta, \tag{3–2}$$

where $R$ is the radius of the aperture. Thus, the interference pattern will be modified according to the size of the aperture as well as the cone angle $\theta$①. The propagation range where the interference pattern exists is defined as the Bessel zone denoted as $z_{\max}$. As shown in Fig. 3–2, it can be approximated geometrically by:

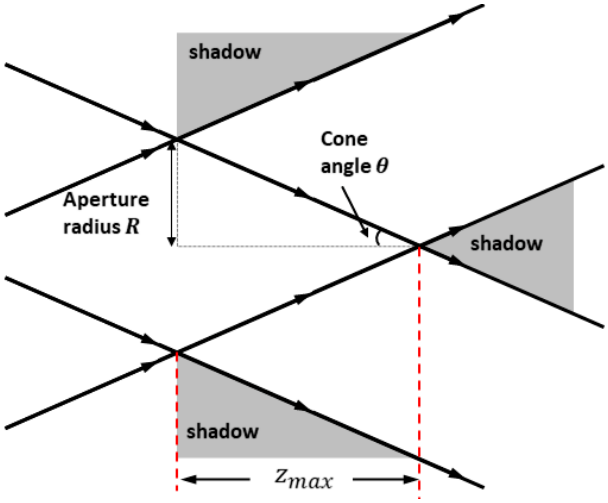


**Figure 3–2 Geometrical illustration of the estimation of Bessel zone $z_{\max}$ (Adapted from [31]).**

### 3.3.1 Usual methods in the generation of Bessel-Gauss beams

There are several methods for experimental generation of Bessel-Gauss beams. Here are some commonly used methods:

- **Fourier transform-based method**: The Fourier transform-based method involves generating a Bessel beam by using the Fourier transform properties of lenses[31]. In this method, a Gaussian beam is first sent through an annular slit positioned at the front focal plane of a lens that generates a Fourier transform of the beam. However, the efficiency of this method is very low in terms of the use of light since most of the beam energy is blocked by the slit.
- **Axicon-based method**: Axicons are conical lenses that can be used to generate Bessel beams[32-34]. The axicon-based method involves focusing a Gaussian beam through an

① $\theta$ is called the cone angle for simplicity while it represents the half-angle of the conical beam.

axicon lens to create a Bessel beam. The axicon lens converts the Gaussian beam into a Bessel beam by introducing a phase shift that results in the non-diffracting properties of the Bessel beam.

- **Digital holography-based method**: Digital holography can be used to generate Bessel beams by encoding a Bessel beam onto a hologram[35-36]. In this method, a digital hologram is generated using a computer program that incorporates both the lens and axicon functions. The hologram is then displayed on a spatial light modulator (SLM) or digital micromirror device (DMD), which converts the digital hologram into a physical hologram that can be projected using a laser beam. A Gaussian beam is focused onto the modulator, which modulates the beam amplitude and phase. The modulator can be programmed to generate different types of Bessel beams with different properties.

These methods are widely used in experimental generation of Bessel-Gauss beams and can be adapted to specific applications depending on the required beam parameters such as beam width, depth of focus, and order.

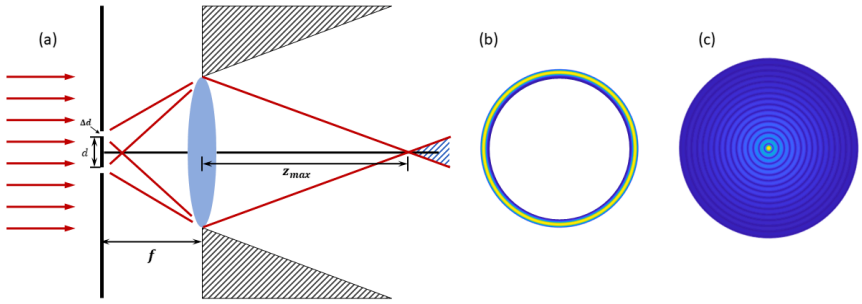


**Figure 3–3 Generation of Bessel-Gauss beams by the Fourier transform-based method. (a) Illustration of the optical path[31]: A collimated Gaussian beam passes through a circular slit placed in the front focal plane of a lens; after the modulated annular beam (b) propagates through the lens, the beam will gradually become a Bessel-Gauss beam (c).**

## 3.4 Generation of controllable filaments through an intermediate state

The full process we used to achieve simultaneous control over the filament position and length is shown in the diagram 3–6. In contrast to prior research, we do not directly manipulate the production of optical filaments by simply modulating the laser output. Instead, in order to achieve complete control, we propose a transient state between the laser output and

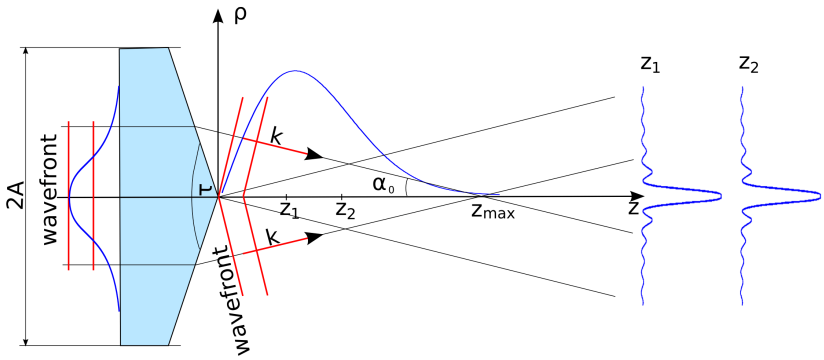


**Figure 3–4 Generation of a Bessel-Gauss beam by the conical lens-based method. A perfect axicon is placed in the propagation path of a Gaussian beam. The wavefront of the beam is indicated by red lines which will be tilted due to the presence of the axicon. Evolution of the maximum beam intensity is shown in blue solid lines.**

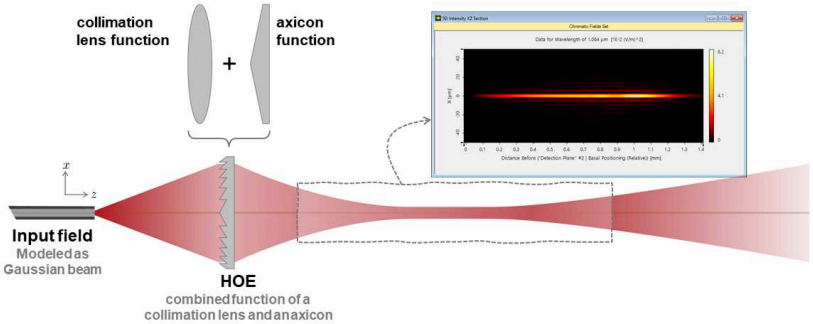


**Figure 3–5 Generation of a Bessel-Gauss beam by the holography-based method. HOE: holographics optical element. The holography is a combination of both the lens and axicon functions. Because of the axicon function, the field behind the HOE remains focused over a relatively long distance.**

the filament to guide the process. We may utilize the Bessel-Gauss beam property to create filaments of uniform and controllable length by choosing it as the intermediate state, and we can correlate the filament length with the beam parameters through numerical simulation of forward propagation. In light of this assumption, our next task is to precisely position the

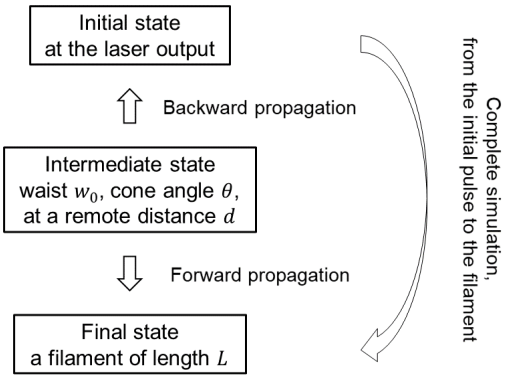


**Figure 3–6 A flowchart that illustrates how to reverse engineer an ultrashort intensity laser pulse so that it becomes a filament through the connection of an intermediate state.**

Bessel-Gauss beam remotely. In order to achieve this, we propagate the intermediate state backward to the laser and compared the resulting field with the laser Gaussian output mode. The appropriate modulation type is then clear to us. It is discovered through numerical simulation that a torus pulse with a spatially linear phase is capable of projecting such a beam over a considerable distance. At last, we directly relate the filament locations $d$ and length $L$ to the torus pulse parameters.

### 3.4.1 Intermediate state and simulation parameters

As mentioned previously, the intermediate state is a Bessel-Gauss beam in our following simulations. We assume that the beam is produced by passing a Gaussian beam through a virtual axicon. After the axicon, the beam is conical, its amplitude is Gaussian in space and time, while the phase is linearly modulated in the radial direction:

$$\mathcal{E}(r,t,z_0) = \mathcal{E}_0 \exp\left(-\frac{r^2}{w_0^2} - \frac{t^2}{t_p^2} - ik_0 r\sin\theta\right), \tag{3–3}$$

where $\mathcal{E}_0$ denotes the maximum amplitude of the electric field envelope, $w_0$ the beam width, $t_p$ the pulse duration, $k_0$ the wavevector of the beam and $\theta$ the cone angle. This beam will

evolve into a Bessel beam $\mathcal{E}(r,t,z_{ax}) \propto J_0(k_0 r \sin\theta)$ after propagation over a distance $z_{ax} = z_{max}/2 = w_0/2\tan\theta$.

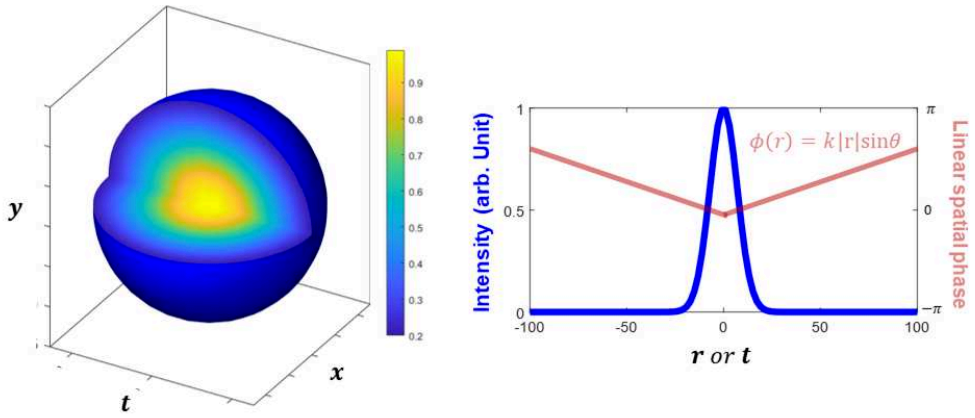


**Figure 3–7 Intensity profile of a Gaussian pulse in 3D space $(x, y, t)$ (left). The red line on the right panel represents the linear phase imprinted by the virtual axicon.**

As introduced in Chapter 2, the evolution of the electric field envelope $\mathcal{E}(r,t,z)$ satisfies the extended nonlinear Schrödinger equation below:

$$\partial_z \mathcal{E} = \frac{i}{2k_0}\Delta_\perp \mathcal{E} + iD(i\partial_t)\mathcal{E} + i\frac{\omega_0}{2cn_0}\frac{\mathcal{P}(\mathcal{E})}{\epsilon_0}. \tag{3–4}$$

On the right hand side the first term denotes diffraction $\Delta_\perp = r^{-1}\partial_r(r\partial_r)$, the second term $D(i\partial_t) = \sum_{n=2}^{+\infty}\frac{k_0^{(n)}}{n!}(i\partial_t)^n$ accounts for the full dispersion of the pulse in time domain. It is easily calculated in the frequency domain as $\hat{D}(\omega) \equiv k(\omega) - k_0 - k_0^{'}(\omega - \omega_0)$, where $k_0 \equiv k(\omega_0)$, while the dispersion in air is due to the frequency dependence of the refractive index $n(\omega)$, which is related to the wavenumber $k(\omega) = n(\omega)\omega/c$ and given by the relation established by Peck and Reeder[37]. The polarization $\mathcal{P}(\mathcal{E})$ in the last term denotes the nonlinear response of the medium to the intense laser pulse:

$$\mathcal{P}(\mathcal{E}) \equiv 2\epsilon_0 n_0(\Delta n(r,t,z) + i\kappa(r,t,z))\mathcal{E}(r,t,z). \tag{3–5}$$

It describes the changes of refractive index $\Delta n$, due to optical Kerr effect and plasma defocusing, as well as nonlinear absorption with a coefficient $\kappa$, contributed by multi-photon

absorption and plasma absorption,

$$\begin{aligned} \Delta n(r,t,z) &= n_2 \int_{-\infty}^{t} R(t-\tau)\mathcal{I}(r,\tau,z)d\tau - \frac{\sigma\omega_0\tau_c}{2k_0}\rho(r,t,z), \\ \kappa(r,t,z) &= \frac{\sigma}{2k_0}\rho(r,t,z) + \frac{\beta_K}{2k_0}\mathcal{I}^{K-1}(r,t,z). \end{aligned} \tag{3–6}$$

The Kerr response function

$$R(t) = (1-f_R)\delta(t) + f_R\frac{\Gamma^2+\Omega^2}{\Omega}\exp(-\Gamma t)\sin(\Omega t) \tag{3–7}$$

encompasses the instantaneous electronic and delayed molecular rotational contributions, parametrized by a relative weight $f_R$ for the delayed part with frequencies $\Gamma$ and $\Omega$. The quantity $\tau_c$ denotes the electron collision time entering in the cross section for inverse bremsstrahlung[38]

$$\sigma = \frac{k_0}{\rho_c}\frac{\omega_0\tau_c}{1+\omega_0^2\tau_c^2}, \tag{3–8}$$

where $\rho_c \equiv \omega_0^2\epsilon_0 m/e^2$ denotes the critical electron number density for an overdense plasma with respect to an electromagnetic radiation of frequency $\omega_0$. Evolution of the electron number density $\rho$ on the femtosecond time scale is described in detail in previous chapters at section 2.2.5.

The input pulse duration is $t_p = 50$ fs and the central wavenumber $k_0 = 2\pi/\lambda_0$ corresponds to a central wavelength of $\lambda_0 = 800$ nm. Different pairs of parameters $(w_0, \theta)$ are chosen for the intermediate state, guided by the knowledge that

1. a linear propagation of the pulse (Eq. (3–3)) would result in a focal line extending over the Bessel zone of length $z_B \equiv w_0/\tan\theta$[31,39],
2. a nonlinear propagation would lead to a filament that covers the Bessel zone with a more uniform intensity[18].

The amplitude $\mathcal{E}_0 = \sqrt{2P_{in}/\pi w_0^2}$ is obtained by fixing $w_0$ and the input power $P_{in}$ for a pulse energy of 10 mJ. The choice of the pulse energy of the intermediate state ensures a negligible ionization for a reversely propagating pulse avoiding therefore an eventual divergence of the simulation[29]. Among nonlinear effects, only the Kerr nonlinearity is relevant during the backward propagation of the intermediate pulse.

Table 3–1 summarizes the parameters used to solve the NLSE (Eq. (3–4)), in both the forward and backward directions with the initial conditions determined by the intermediate state given by Eq. (3–3)). The critical power $P_{cr}$ for self-focusing is about 3 GW.

**Table 3–1 Parameters used for simulations of the nonlinear pulse propagation of a Bessel-Gauss beam**

| | Air, 800 nm |
|---|---|
| Pulse energy (mJ) | 10 |
| $\theta$ (deg) | 0.1, 0.125, 0.15, 0.175, 0.2 |
| $w_0$ (mm) | 5, 10, 15, 20 |
| $t_p$ (fs) | 50 |
| $n_2$ (m$^2$/W) | $3.2 \times 10^{-23}$ |
| $f_R$ | 0.5 |
| $\Gamma^{-1}$ (fs) | 70 |
| $\Omega$ (THz) | 16 |
| $\tau_c$ (fs) | 350 |
| $E_g$ (eV) | 12.1 |
| $K$ | 8 |
| $\beta^{(K)}$ (m$^{13}$/W$^7$) | $1.83 \times 10^{-120}$ |
| $a$ (m$^3$/s) | $5.0 \times 10^{-13}$ |

### 3.4.2 Forward propagation: Filamentation of a Bessel-Gauss beam

We first determine the conditions required to generate a filament in air with a several meters long plasma channel by modeling the nonlinear propagation of the intermediate state - a Bessel-Gauss beam. The evolution of the field and the generation of a filament depend on the properties of the intermediate state, especially the spatial distribution of the intensity. The fluence of the beam $F(r,z) = \int_{-\infty}^{+\infty} dt|\mathcal{E}(r,t,z)|^2$ is shown in Fig. 3–8 as a function of $(w_0, \theta)$. It is evident that the Bessel zone lengthens with increasing $w_0$ and shortens with increasing $\theta$. When $w_0$ is small, oscillations of the intensity is also observed. The appearance of periodic oscillations of a small amplitude is due to

- the interference between the conical and axial components of the beam,
- the interference induced by the nonlinear phase modulation.

Fig. 3–9 (a) shows the result of a Fourier analysis of the peak intensity profiles along the $z$-axis, allowing us to analyse the small-oscillation period. For each value of the cone angle, the period matches the function $\lambda/(1-\cos\theta)$ which reflects the interference between axial and conical components of the beam[17,34]. We can clearly see this interference pattern in the evolution of power $P(t,z) = \int_0^{\infty} 2\pi r dr|\mathcal{E}(r,t,z)|^2$ along $z$, shown in Fig. 3–9 (b).

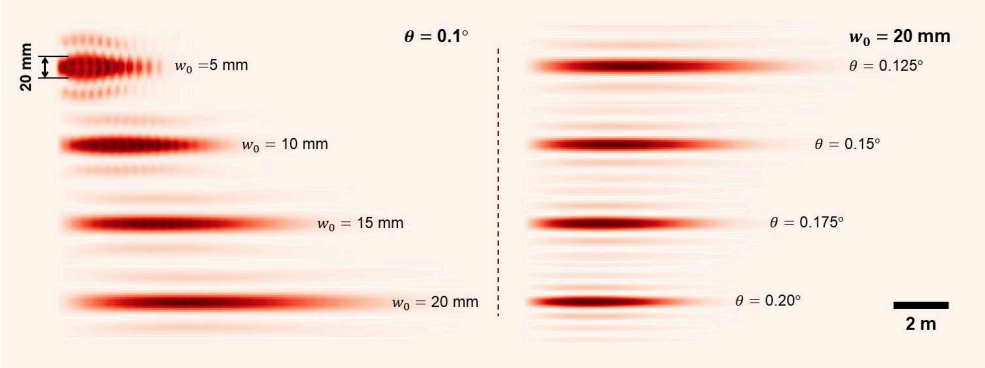


**Figure 3–8 Evolution of fluence along the propagation path from the intermediate state to the filamentation regime as a function of (left panel) $w_0$ with fixed $\theta = 0.1$. From top to bottom: $w_0$ = 5 mm, $w_0$ = 10 mm, $w_0$ = 15 mm, $w_0$ = 20 mm and (right panel) of $\theta$ with fixed $w_0$ = 20 mm. From top to bottom: $\theta = 0.125°$, $\theta = 0.15°$, $\theta = 0.175°$, $\theta = 0.20°$.**

The wavefront whose curvature is negative evidences the phase modulation caused by self-focusing.

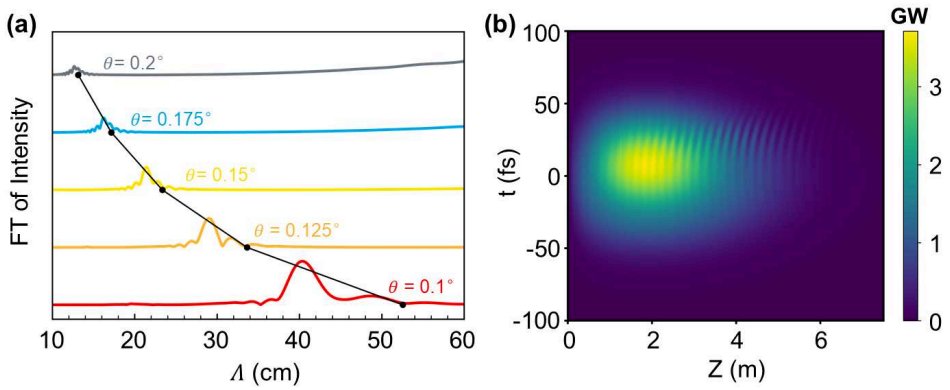


**Figure 3–9 (a). Fourier analysis of the peak intensity profile along $z$ for constant $w_0 = 15mm$ and for different cone angles $\theta$. The horizontal axis has been transformed to show the modulation period in length units. The black dotted line represents $\Lambda = \lambda/(1 - \cos\theta)$ where $\lambda$ = 800 nm. (b). Evolution of power along the propagation axis from the intermediate state at $z = 0$ to the filamentation regime.**

Fig. 3–10 presents a summary of the simulation results for the peak intensity of the filament and the peak electron number density in the plasma channel. They are obtained for cone angles $\theta$ ranging from 0.1 to 0.2 degrees and for beam widths $w_0$ ranging from 5 to 20 mm. The peak intensity is calculated by taking the maximum of $|\mathcal{E}(r,t,z)|^2$ at each propagation distance $z$ and the electron density is extracted out by solving the rate equation

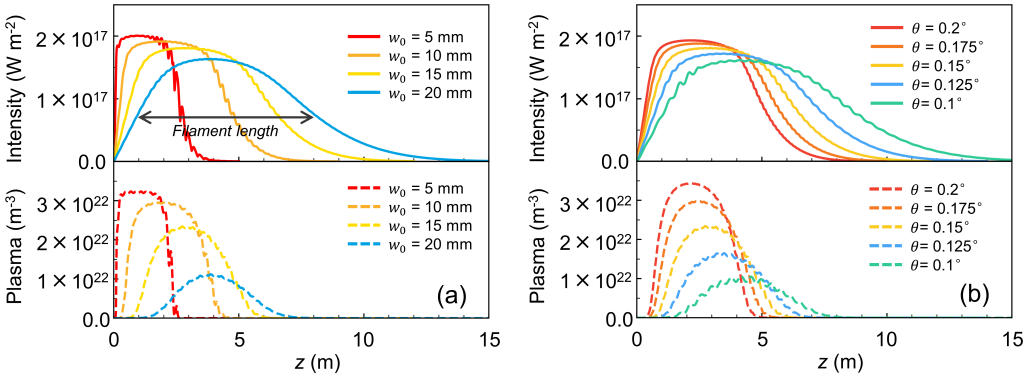


**Figure 3–10 Peak intensity and electron number density of a filament as functions of the propagation distance $z$. (a) for different beam waists $w_0$ of the intermediate pulse with a given cone angle $\theta = 0.15°$, and (b) for different cone angles $\theta$ with $w_0 = 15$ mm. The length of a filament $L$ is extracted by measuring the full width at half maximum (FWHM) of the intensity curve.**

governing the photoionization (See Eq. (2–22)). Shown in Fig. 3–10 (a) are results for a fixed cone angle $\theta = 0.15°$. With an increasing $w_0$, both the peak intensity and electron density decrease, while the lengths of the corresponding light and plasma channels increase. Results in Fig. 3–10 (b) are obtained for different cone angles by keeping a constant $w_0 = 15$ mm. The peak intensity and electron number density grow with an increasing $\theta$, while the channel lengths are reduced. The observed trends are determined by the spatial phase distribution of the intermediate pulse, which governs the conical energy flux sustaining the filament. As the waist $w_0$ increases, a larger energy reservoir surrounds the central core. In parallel, a smaller cone angle $\theta$ reduces the inward energy flow. The nonlinear propagation can be maintained for a longer distance due to the both effects. Note that in all simulation results, a single, continuous and quite homogeneous filament with the associated plasma channel string is obtained.

Quantitatively, the length of a filament $L$ is defined by the full width at half maximum (FWHM) of the peak intensity profile along the $z$-axis (see Fig. 3–10 (a)). Filament lengths calculated from our simulation results are shown in Fig. 3–11 as a function of $w_0$ and $\theta$. In our simulations, intensity clamping becomes one of the relevant effects flattening the profiles of the peak intensity along the $z$-axis, as compared to the profile obtained with a linear propagation of a Bessel-Gauss beam, whose focal line scales as the Bessel zone $z_B = w_0/\tan\theta$. A fit of the simulation data results in a scaling law of the filament length $L$ as a function of

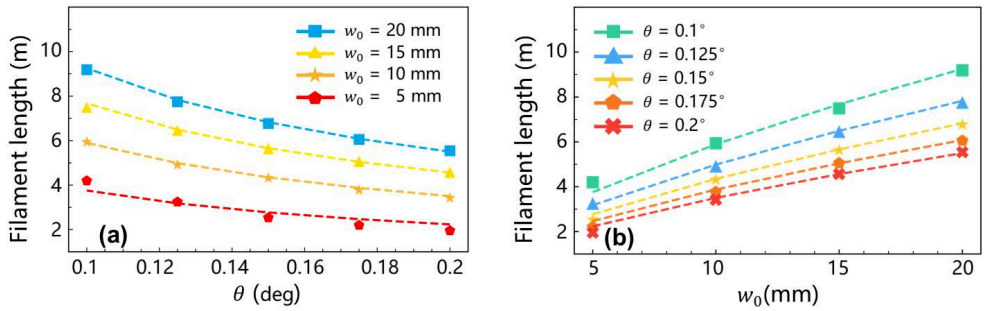


**Figure 3–11 Filament length $L$ as a function of (a) the cone angle $\theta$, and (b) the beam waist ($w_0$) of the intermediate state. The dashed lines represent the fits by the function given in Eq.** (3–9)

$w_0$ and $\theta$:

$$L(w_0, \theta) = 136 \frac{\lambda_0^{0.35} w_0^{0.65}}{(\tan\theta)^{0.75}} \propto z_B^{0.75} / \hat{w}_0^{0.1}. \tag{3–9}$$

The dependence on the dimensionless beam waist $\hat{w}_0 \equiv w_0/\lambda_0$ and $\theta$ indicates that the filament length is expected to increase less fast than the Bessel range $z_B$, when $w_0$ increases or $\theta$ decreases. The scaling law of Eq. (3–9) provides therefore a practical way to precisely control the length of a filament, together with its related properties by the characteristics of the intermediate state.

### 3.4.3 Back propagation toward an initial state nearby the laser

To investigate the required initial pulse capable of projecting a Bessel-Gauss beam at a large distance, we propagate the intermediate pulse backward toward the laser and deduce the characteristics of the initial pulse nearby the laser. Since the intermediate pulse is chosen to have an intensity below the ionization threshold while possibly carrying a significant energy with a quite large beam waist, and a spatial phase gradient corresponding to a divergent back propagation, the reverse solution is almost linear, except for a small contribution from the optical Kerr effect.

Fig. 3–12 shows the simulation results of the amplitude and phase distributions of an initial pulse obtained at a distance $d$ of 20 m upstream of the intermediate state. During the reverse propagation, the intermediate Bessel-Gauss pulse evolves into a torus-like pulse that can be considered as a Gaussian pulse with a ring beam profile (Fig. 3–12 (a) & (d)). The major and minor radii $w_R$, $w_r$ of the ring depend on $w_0$ and $\theta$. There is almost no change in the distribution of the electric field envelope along the time axis. The pulse remains Gaussian

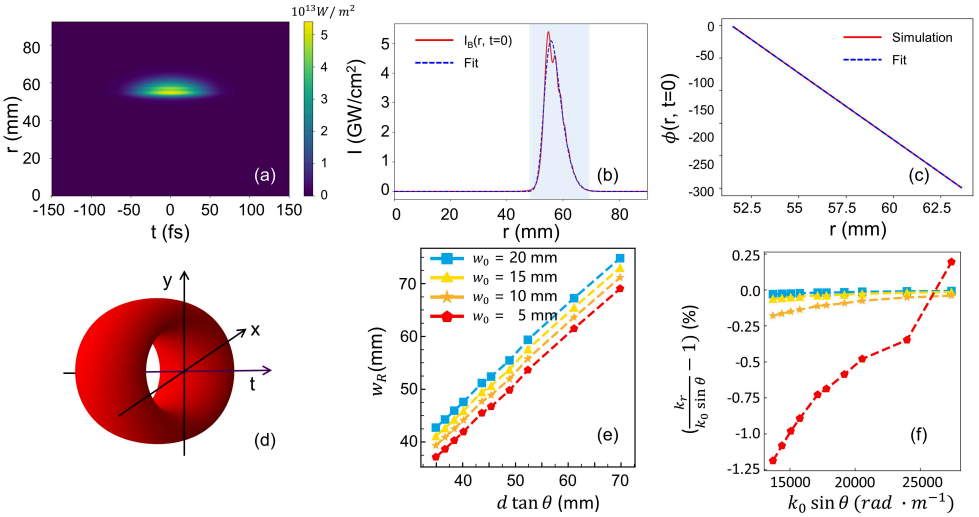


**Figure 3–12 Results of the reverse propagation of the intermediate pulse over a distance $d$ of 20 m, with $\theta = 0.15°, w_0 = 10$ mm. (a) Intensity distribution of the resulting initial pulse $|\mathcal{E}(r,t,z=-d)|^2$ as a function of $r$ and $t$. (b) Intensity in the pulse center $|\mathcal{E}(r,t=0,z=-d)|^2$ and a fit with Eq. (3–12). (c) Radial phase variation at the center of the pulse $\phi(r,t=0)$ and its fit with a linear function. (d) Illustration of a torus pulse. (e) Major radius of the initial torus pulse $w_R$ as a function of $d\tan\theta$ for different $w_0$. (f) Comparison of the actual radial wavenumber $k_r$ of the torus pulse and the projection of the central wavevector $k_0 \sin\theta$.**

and its duration is nearly the same as that of the intermediate pulse of 50 fs. Dispersion in air is too weak to induce a significant pulse distortion over a distance of 20 m, the dispersive length in air for a 50 fs pulse being 62 m.

For a larger propagation distance, dispersion can be compensated by pre-chirping the initial pulse. In this case, we can use a parabolic function to express the chirped temporal phase and a Gaussian function to express the amplitude when reversely propagating the wavefront. Along the radial axis, the electric field amplitude evolves into a ring beam (Fig. 3–12 (b)) with a linear phase shift within the width of the ring, $\phi(r) = k_r + \phi_0$ as shown in Fig. 3–12 (c).

The simulated values of $w_R$ as a function of $w_0$ and $\theta$ are shown in Fig. 3–12(e). In the figure, we can see that the data can be well fitted by the relations derived by Gori *et al.* for the diffraction of a Bessel-Gauss beam[39], proving that they remain a valid approximation of the solution in the presence of a weak nonlinear effect,

$$w_R \sim d\tan(\theta). \tag{3–10}$$

At the same time, the simulations also show a good fit of the values of $w_r$ by the diffraction

of a Bessel-Gauss beam[39],

$$w_r \sim w_0\sqrt{1 + d^2/{Z_R}^2}, \tag{3–11}$$

where $w_0$ is the beam waist at the intermediate state and $Z_R = \pi {w_0}^2/\lambda_0$ the Rayleigh length. In Fig. 3–12 (f), the actual radial wavevectors $k_r$ extracted from the simulations are compared with the projection of the central wavevector $k_0 \sin\theta$ according to the cone angle of the Bessel-Gauss beam. The result shows a relative difference within 2‰, which confirms a quite good linear variation of the phase, similar to the intermediate state.

### 3.4.4 Projection of a torus pulse into a remote filament

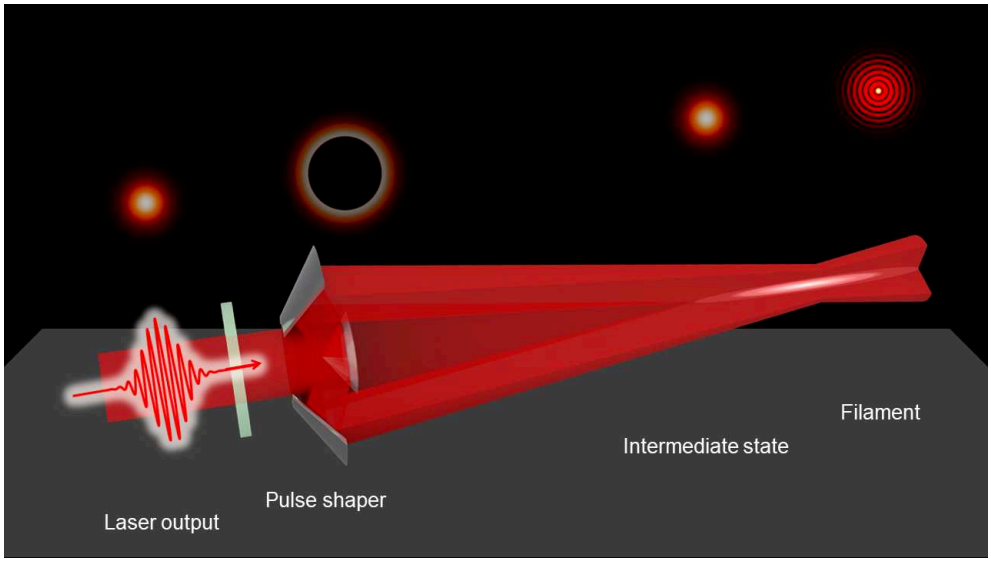


**Figure 3–13 Schematic representation of reverse engineering of a remote filament. Starting with a predefined intermediate state, the wavefronts after the pulse shaper are calculated by backward propagation. From the Gaussian pulse at the laser output, the required phase and amplitude modulation can be realized by a phase plate and axicon reflectors. The color plots show the evolution of the field from a Gaussian to a torus pulse through the pulse shape, the projection of the torus pulse to a Gaussian beam passing through a remote virtual axicon, and finally its propagation in the form of a nonlinear Bessel-Gauss beam entering into the filamentation regime.**

The above simulation results suggest an implementation of the studied method to launch and control a filament at a remote distance. As shown in Fig. 3–13, an output pulse from a CPA laser with temporal and spatial Gaussian profiles, transmits first through a phase plate ensuring a linear radial phase modulation over the wavefront of the pulse. It is then reflected on an axicon mirror resulting in a pulse with a ring-formed beam profile. The latter propa-

gates toward a ring mirror and is reflected in the forward direction with a required convergence angle. At the same time, the reflectivity of the ring mirror is modulated in the radial direction so that when the ring-formed beam is reflected away from it, its intensity profile in the radial direction within the width of the ring is modulated according to the required profile. The ensemble of the phase plate, the axicon mirror and the ring mirror constitutes therefore a pulse shaper, which can transform a Gaussian pulse from a CPA laser into a torus pulse required for the projection of an intermediate state of a Bessel-Gauss pulse and the subsequent formation of a filament.

For an easy implementation of the above conceptual arrangement, we neglect the small scale radial modulation of the intensity within the width of the ring beam profile as shown in Fig. 3–12 (a) and (b). The radial intensity distribution is approximated by a Gaussian profile centered at a major radius of $w_R$ and having a $e^{-1}$ half width of $w_r$. Simulations results will show the pertinence of this approximation, supported by the fact that a similar filament can be formed when an actual radial intensity profile is replaced by the above described Gaussian profile. The initial pulse obtained by reverse engineering as shown in Fig. 3–12 (a) and (b) is therefore approximated by an analytical expression,

$$\mathcal{E}_{\mathrm{eng}}(r,t) = A\exp\left(-\frac{(r-w_R)^2}{w_r^2} - (1+iC)\frac{t^2}{t_0^2} - ik_r r\right)\left[1+\mathrm{erf}\left(p\frac{(r-w_R)}{\lambda\sqrt{\hat{w}_r}}\right)\right], \qquad (3\text{–}12)$$

where $A$ is the amplitude determined by the pulse energy, $\mathrm{erf}(x)$ represents the error function, $p$ is a fitting parameter which can be approximated by $p \cong 0.028$ and $\hat{w}_r \equiv w_r/\lambda_0$. The chirp coefficient $C$ is parametrized so as to compensate for dispersion during the projection stage to the intermediate state, i.e., $C = -d/Z_d$ where $Z_d = t_p^2/2k''$ denotes the dispersion length. The initial pulse duration can be modified accordingly to $t_0 = t_p\sqrt{1+d^2/Z_d^2}$. For $t_p = 50$ fs and $k'' = 0.2$ fs$^2$/cm, we find $Z_d = 62.5$ m, and for $d = 20$ m, we obtain $C = 0.32$ and $t_0 = 1.05t_p$. Such ideal torus pulse considered as the initial state of a complete forward propagation is therefore characterized by three parameters of $w_R$, $w_r$, and $d$, together with the characteristics of the pulse delivered by the CPA laser (pulse energy, pulse duration and wavelength). Note that $k_r = k_0 \sin\theta$, and $\theta$ can be further expressed as a function of $w_R$ and $d$. The intensity distribution of an ideal torus pulse is shown in Fig. 3–14 for projecting an intermediate state with $\theta = 0.15°$ and $w_0 = 10$ mm at a distance $d = 20$ m.

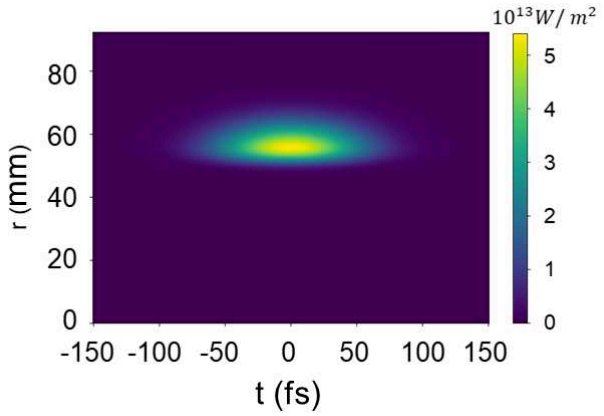


**Figure 3–14 Intensity profile of an ideal torus pulse as the initial state for projecting a Bessel-Gauss beam intermediate state at a distance $d = 20$ m, with $\theta = 0.15°$ and $w_0 = 10$ mm, the corresponding spatial and temporal phases are respectively linear and quadratic as described in the previous section.**

### 3.4.5 Full propagation: filamentation of a torus pulse

Starting the simulation from the torus pulse of Eq. (3–12) and propagating forward, the results confirm that the pulse is focused at the predefined projection distance $d$ and further evolves into a filament with a length $L(w_R, w_r, d)$. It is therefore interesting to deduce the expression of $L(w_R, w_r, d)$ using the above deduced scaling law of $L(w_0, \theta)$ in Eq. (3–9) and those relating $w_0$ and $\theta$ to $w_R$, $w_r$ and $d$. Furthermore, using the scaling laws of Eqs. (3–10) and (3–11) confirmed by the results of the reverse simulation, we can relate the pair of control parameters of the intermediate state $w_0$ and $\theta$ to the characteristics of the ideal torus pulse of the initial state and the projection distance $d$,

$$\tan\theta = \frac{w_R}{d}, \tag{3–13}$$

$$w_0^2 = \frac{w_r^2}{2}\left(1 + \sqrt{1 - \frac{4d^2}{Z_r^2}}\right), \tag{3–14}$$

where $Z_r = \pi w_r^2/\lambda_0$ denotes the Rayleigh length constructed from $w_r$. Note that, $Z_r$ must be greater than twice the projection distance to avoid reaching the diffraction limit. The scaling law for the filament length $L$ as a function of the projection distance $d$ and the torus pulse

radii $w_R$ and $w_r$ can thus be deduced:

$$L(w_R, w_r, d) \approx \frac{51.6\,\lambda_0 \left[\frac{Z_r^2}{w_r^2}\left(1+\sqrt{1-\frac{4d^2}{Z_r^2}}\right)\right]^{0.325}}{(w_R/d)^{0.75}}. \tag{3–15}$$

Figure 3–15 briefly illustrates the projection of the torus pulse into a filament with corresponding geometric relationship between the variables.

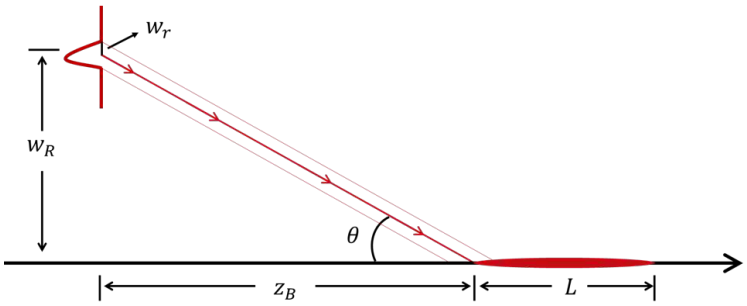


**Figure 3–15 Schematic representation of the projection of a torus pulse.**

An end-to-end forward propagation simulation is then performed to calculate the filament length $L$ for various combinations between $w_R$ and $w_r$ when $d$ is fixed at 20 m. The obtained results are shown in Fig. 3–16 together with the plots of the scaling law of Eq. (3–16). A good agreement can be observed. This scaling law can thus be used to determine the parameters of the torus pulse of the initial state according to the starting distance $d$ and the length $L$ of the filament that we want to generate. In practice, several pairs of $(w_R, w_r)$ can be used to achieve the same filament projection. For instance, the minor radius of the torus $w_r$ can be chosen arbitrarily provided that the condition $Z_r > 2d$ is fulfilled, then requiring the major radius $w_R$ to satisfy

$$w_R \approx 192\,d\left(\frac{\lambda_0}{L}\right)^{1.33}\left[\frac{Z_r^2}{w_r^2}\left(1+\sqrt{1-\frac{4d^2}{Z_r^2}}\right)\right]^{0.43}, \tag{3–16}$$

and the transverse wavenumber characterizing the radial spatial phase modulation is determined by $k_r = k_0 w_R/d$. Fig. 3–17 shows the dependence of $w_R$ upon the target filament length $L$ for several values of $d$ and $w_r$. The reduction of possible values of $w_r$ as $d$ increases is due to the threshold condition of $w_r > \sqrt{2d\lambda_0/\pi}$. The case of $w_R < w_r$ is also excluded. In the figure, we also plot the filament lengths resulting from the simulations for

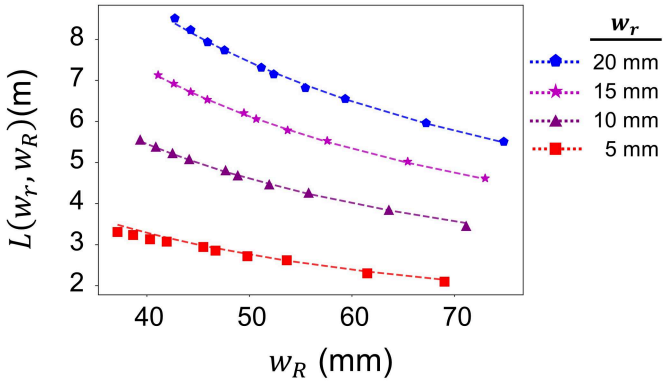


**Figure 3–16 Filament length as a function of the major radius $w_R$ of the torus pulse (see Eq. (3–12)) after forward propagation over $d = 20$ m. Dashed curves correspond to the fitting function given in Eq. (3–15) for different values of the minor radius $w_r$.**

$d = 20$ m. We can see that longer filaments can be produced at a same projection distance by keeping $w_R$ fixed and by increasing $w_r$ (up to $w_r \approx w_R$). In addition, we can launch a filament of a given length to a larger distance by increasing $w_R$ while keeping $w_r$ fixed.

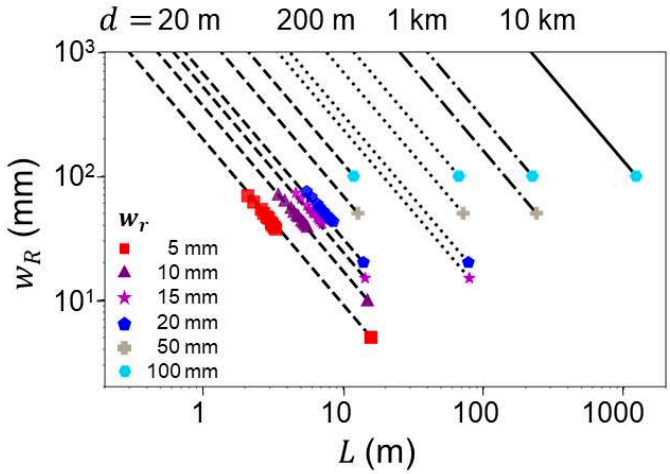


**Figure 3–17 Torus major radius $w_R$ as a function of the filament length $L$, for various minor radius $w_r$ and projection distances $d$ up to 10 km. Each line corresponds to a fixed value of $w_r$ and $d$.**

Finally, our simulations show that the larger the projection distance and the filament length are, the larger the values of $w_R$ and $w_r$ are required. For instance, projecting a 10 m long filament to a distance of $d = 100$ m, requires a torus pulse with $w_R = 8.1$ cm and $w_r = 1$ cm (corresponding to a $\theta = 0.045°$). If the projection distance is increased to $d = 1$ km,

$w_r$ must be increased above the threshold value of $\approx 2.26$ cm. Choosing $w_r = 6$ cm, a 10 m long filament can be generated with a relatively large $w_R \approx 3.9$ m. Alternatively, with the other parameters ($w_r = 6$ cm, $d = 1$ km) kept unchanged, filaments with longer lengths of $L = 30$ m or $L = 100$ m can be generated with smaller $w_R$ of respectively 91 cm or 18 cm, which remains still manageable with a tabletop laboratory optical arrangement.

## 3.5 Discussion and conclusion

In our results, the simultaneous control of the filament length and projection distance relies on two key processes: (i) the focusing stage of the torus pulse into the intermediate Bessel-Gauss beam state is entirely achieved in a weakly nonlinear regime where the peak intensity remains below ionization threshold; (ii) The subsequent filamentation of the powerful Bessel-Gauss intermediate state is governed by the spontaneous generation of a propagation-invariant beam during its nonlinear propagation, previously identified as a nonlinear unbalanced Bessel beam[13-16]. As in previous experiments on long range filamentation, optical components of large size are required to reach long distances but the benefits of projecting a nonlinear Bessel beam lies in the simultaneous control of the filament length and projection distance. We discuss the main physical effects in each propagation stage.

During the first stage, the only nonlinear effect influencing the propagation is the optical Kerr effect. Nonlinear losses are negligible as the highest peak intensity appearing at the projection distance for the intermediate state is chosen below ionization threshold, while allowing for the power of the beam to exceed the critical threshold for self-focusing. In this stage, propagation in the forward and backward directions is essentially governed by diffraction and dispersion, making possible the semi-analytical derivation of the scaling laws (3–15) and (3–16) for the filament length, reflecting diffraction optics and dispersion compensation of a pre-chirped pulse.

During the second propagation stage from the intermediate state to the filament, the prevailing physical effects in the formation of a homogeneous filament are diffraction, optical Kerr effect and nonlinear losses. The intermediate state is organized as a conical wave, i.e., a beam whose spatial phase is set to drive an energy flux along the vertex of a cone. The linear propagation of this state would result in the formation of a Bessel beam profile in the focal Bessel zone, which can be described as a superposition of two balanced Hankel components,

carrying along the cone vertex the same amount of energy in and out of the focal region[15]. When the intensity in the focal region exceeds ionization threshold, nonlinear losses generate an unbalance in the Hankel components as the energy conservation requires that the energy flux in the focal region must be equal to the sum of the energy losses in the hot core of the beam and the energy flux out of the focal region. Moreover, this unbalance was shown to characterize attractors of the dynamics of nonlinear Bessel beam propagation in a Kerr media with nonlinear losses, in the form of propagation-invariant solutions to the NLS equation called nonlinear unbalanced Bessel beams, which are supported by the inward energy flux until the energy reservoir is exhausted[15-16]. These solutions are stable in a large region of the parameter space and therefore propagate steadily, giving rise to the resulting homogeneous filaments. An unsteady propagation regime also exists, generally obtained for smaller cone angles than those we have considered, that would give rise to nonhomogeneous filaments. However, our results were limited to homogeneous filaments.

The simultaneous control of the length and projection distance of homogeneous filaments proposed in this work is therefore only limited by two requirements: (i) avoid a strong self-focusing that would lead to ionization before the target position of the intermediate Bessel-Gauss beam; (ii) avoid the unsteady regime for nonlinear unbalanced Bessel beams[16-18].

In conclusion, we have implemented inverse design in numerical simulation of the nonlinear propagation of a NIR intense femtosecond laser pulse in air. Starting from an intermediate state in the form of a Gaussian pulse with a Bessel-Gauss beam profile characterized by the waist $w_0$ and the cone angle $\theta$, its propagation is simulated using the NLSE in both the forward and backward directions. In the forward direction, the intermediate pulse evolves into a filament with the associated plasma channel. The length of the filament, $L$, is found to be controlled by $w_0$ and $\theta$. The intermediate pulse is then reversely propagated, showing the evolution of the beam profile into a torus structure with a linearly increasing radius as it approaches the CPA laser which can deliver the pulse, situated at a distance of $d$ from the intermediate state. The divergent backward propagation leads to a decrease of the intensity, avoiding ionization of the air molecules crossed by the pulse and potential divergences during reverse simulation. The obtained torus-like beam profile can be characterized by the major and minor radii $w_R$, $w_r$, as well as a linear radial phase. Both parameters $w_R$ and $w_r$ are

shown to be related to $w_0$, $\theta$ and $d$. An end-to-end forward propagation simulation is thus performed from an ideal initial torus pulse to the final filament, confirming the validity of the pulse reverse engineering procedure. Scaling laws are extracted to express $w_0$ and $\theta$ as functions of $w_R$, $w_r$ and $d$, which in turn allows for deducing a scaling law relating the filament length $L$ to the projection distance $d$ and the radii of the initial torus pulse $w_R$ and $w_r$. A conceptual optical beam shaper, with a combination of a phase plate, an axicon reflector and a ring mirror, is proposed to transform a Gaussian pulse at the output of a CPA laser into a torus pulse able to launch a Bessel filament at a remote distance. The quasi linear propagation of the initial torus pulse toward a virtual intermediate state of a Bessel-Gauss beam profile offers a large scalability of the projection distance $d$. An extrapolation of the numerical results obtained in this work thus allows for launching filaments of several tens of meters long at hundreds to thousands of meters in air for a large number of applications.

## Bibliography

[1] RODRIGUEZ M, BOURAYOU R, MÉJEAN G, et al. Kilometer-range nonlinear propagation of femtosecond laser pulses[J/OL]. Phys. Rev. E, 2004, 69: 036607. https://link.aps.org/doi/10.1103/PhysRevE.69.036607. DOI: 10.1103/PhysRevE.69.036607.

[2] DURAND M, HOUARD A, PRADE B, et al. Kilometer range filamentation[J/OL]. Opt. Express, 2013, 21(22): 26836-26845. http://opg.optica.org/oe/abstract.cfm?URI=oe-21-22-26836. DOI: 10.1364/OE.21.026836.

[3] EISENMANN S, LOUZON E, KATZIR Y, et al. Control of the filamentation distance and pattern in long-range atmospheric propagation[J/OL]. Opt. Express, 2007, 15(6): 2779-2784. http://opg.optica.org/oe/abstract.cfm?URI=oe-15-6-2779. DOI: 10.1364/OE.15.002779.

[4] MÉCHAIN G, COUAIRON A, ANDRÉ Y B, et al. Long-range self-channeling of infrared laser pulses in air: a new propagation regime without ionization[J]. Applied Physics B, 2004, 79: 379-382.

[5] MÉCHAIN G, C.D' Amico, ANDRÉ Y B, et al. Range of plasma filaments created in air by a multi-terawatt femtosecond laser[J/OL]. Optics Communications, 2005, 247(1): 171-180. https://www.sciencedirect.com/science/article/pii/S0030401804011812. DOI: https://doi.org/10.1016/j.optcom.2004.11.052.

[6] MÉCHAIN G, MÉJEAN G, ACKERMANN R, et al. Propagation of fs TW laser filaments in adverse atmospheric conditions[J/OL]. Applied Physics B, 2005, 80(7): 785-789. https://doi.org/10.1007/s00340-005-1825-2. DOI: 10.1007/s00340-005-1825-2.

[7] COUAIRON A, FRANCO M, MÉCHAIN G, et al. Femtosecond filamentation in air at low pressures: Part I: Theory and numerical simulations[J/OL]. Optics Communications, 2006, 259(1): 265-273. https://www.sciencedirect.com/science/article/pii/S0030401805009156. DOI: https://doi.org/10.1016/j.optcom.2005.08.064.

[8] MÉCHAIN G, OLIVIER T, FRANCO M, et al. Femtosecond filamentation in air at low pressures. Part II: Laboratory experiments[J/OL]. Optics Communications, 2006, 261(2): 322-326. https://www.sciencedirect.com/science/article/pii/S0030401805012344. DOI: https://doi.org/10.1016/j.optcom.2005.11.041.

[9] IONIN A A, IROSHNIKOV N G, KOSAREVA O G, et al. Filamentation of femtosecond laser pulses governed by variable wavefront distortions via a deformable mirror[J/OL]. J. Opt. Soc. Am. B, 2013, 30(8): 2257-2262. http://opg.optica.org/josab/abstract.cfm?URI=josab-30-8-2257. DOI: 10.1364/JOSAB.30.002257.

[10] APEKSIMOV D V, GEINTS Y E, ZEMLYANOV A A, et al. Controlling TW-laser pulse long-range filamentation in air by a deformable mirror[J/OL]. Appl. Opt., 2018, 57(33): 9760-9769. http://opg.optica.org/ao/abstract.cfm?URI=ao-57-33-9760. DOI: 10.1364/AO.57.009760.

[11] ENGLESBE A C, HE Z, NEES J A, et al. Control of the configuration of multiple femtosecond filaments in air by adaptive wavefront manipulation[J/OL]. Opt. Express, 2016, 24(6): 6071-6082. http://opg.optica.org/oe/abstract.cfm?URI=oe-24-6-6071. DOI: 10.1364/OE.24.006071.

[12] MLEJNEK M, WRIGHT E M, MOLONEY J V. Dynamic spatial replenishment of femtosecond pulses propagating in air[J]. Opt. Lett., 1998, 23(5): 382-384.

[13] DUBIETIS A, KUČINSKAS E, TAMOŠAUSKAS G, et al. Self-reconstruction of light filaments[J/OL]. Opt. Lett., 2004, 29(24): 2893-2895. http://opg.optica.org/ol/abstract.cfm?URI=ol-29-24-2893. DOI: 10.1364/OL.29.002893.

[14] DUBIETIS A, GAIŽAUSKAS E, TAMOŠAUSKAS G, et al. Light Filaments without Self-Channeling[J/OL]. Phys. Rev. Lett., 2004, 92: 253903. https://link.aps.org/doi/10.1103/PhysRevLett.92.253903. DOI: 10.1103/PhysRevLett.92.253903.

[15] PORRAS M A, PAROLA A, FACCIO D, et al. Nonlinear Unbalanced Bessel Beams: Stationary Conical Waves Supported by Nonlinear Losses[J/OL]. Phys. Rev. Lett., 2004, 93: 153902. https://link.aps.org/doi/10.1103/PhysRevLett.93.153902. DOI: 10.1103/PhysRevLett.93.153902.

[16] PORRAS M A, RUIZ-JIMÉNEZ C, LOSADA J C. Underlying conservation and stability laws in nonlinear propagation of axicon-generated Bessel beams[J/OL]. Phys. Rev. A, 2015, 92: 063826. https://link.aps.org/doi/10.1103/PhysRevA.92.063826. DOI: 10.1103/PhysRevA.92.063826.

[17] POLESANA P, COUAIRON A, FACCIO D, et al. Observation of Conical Waves in Focusing, Dispersive, and Dissipative Kerr Media[J/OL]. Phys. Rev. Lett., 2007, 99: 223902. https://link.aps.org/doi/10.1103/PhysRevLett.99.223902. DOI: 10.1103/PhysRevLett.99.223902.

[18] POLESANA P, FRANCO M, COUAIRON A, et al. Filamentation in Kerr media from pulsed Bessel beams[J/OL]. Phys. Rev. A, 2008, 77: 043814. https://link.aps.org/doi/10.1103/PhysRevA.77.043814. DOI: 10.1103/PhysRevA.77.043814.

[19] POLYNKIN P, KOLESIK M, ROBERTS A, et al. Generation of extended plasma channels in air using femtosecond Bessel beams[J/OL]. Opt. Express, 2008, 16(20): 15733-15740. http://opg.optica.org/oe/abstract.cfm?URI=oe-16-20-15733. DOI: 10.1364/OE.16.015733.

[20] AKTURK S, ZHOU B, FRANCO M, et al. Generation of long plasma channels in air by focusing ultrashort laser pulses with an axicon[J/OL]. Optics Communications, 2009, 282(1): 129-134. https://www.sciencedirect.com/science/article/pii/S0030401808009607. DOI: https://doi.org/10.1016/j.optcom.2008.09.048.

[21] MILLS M S, KOLESIK M, CHRISTODOULIDES D N. Dressed optical filaments[J/OL]. Opt. Lett., 2013, 38(1): 25-27. http://opg.optica.org/ol/abstract.cfm?URI=ol-38-1-25. DOI: 10.1364/OL.38.000025.

[22] SCHELLER M, MILLS M S, MIRI M A, et al. Externally refuelled optical filaments[J/OL]. Nature Photonics, 2014, 8(4): 297-301. https://doi.org/10.1038/nphoton.2014.47. DOI: 10.1038/nphoton.2014.47.

[23] BHUYAN M K, COURVOISIER F, LACOURT P A, et al. High aspect ratio nanochannel machining using single shot femtosecond Bessel beams[J/OL]. Applied Physics Letters, 2010, 97(8): 081102. eprint: https://doi.org/10.1063/1.3479419. https://doi.org/10.1063/1.3479419. DOI: 10.1063/1.3479419.

[24] VETTER C, GIUST R, FURFARO L, et al. High Aspect Ratio Structuring of Glass with Ultrafast Bessel Beams[J/OL]. Materials, 2021, 14(22). https://www.mdpi.com/1996-1944/14/22/6749. DOI: 10.3390/ma14226749.

[25] JUKNA V, MILIÁN C, XIE C, et al. Filamentation with nonlinear Bessel vortices[J/OL]. Opt. Express, 2014, 22(21): 25410-25425. http://opg.optica.org/oe/abstract.cfm?URI=oe-22-21-25410. DOI: 10.1364/OE.22.025410.

[26] DOTA K, PATHAK A, DHARMADHIKARI J A, et al. Femtosecond laser filamentation in condensed media with Bessel beams[J/OL]. Phys. Rev. A, 2012, 86: 023808. https://link.aps.org/doi/10.1103/PhysRevA.86.023808. DOI: 10.1103/PhysRevA.86.023808.

[27] BHUYAN M K, VELPULA P K, COLOMBIER J P, et al. Single-shot high aspect ratio bulk nanostructuring of fused silica using chirp-controlled ultrafast laser Bessel beams[J/OL]. Applied Physics Letters, 2014, 104(2): 021107. eprint: https://doi.org/10.1063/1.4861899. https://doi.org/10.1063/1.4861899. DOI: 10.1063/1.4861899.

[28] COURVOISIER F, STOIAN R, COUAIRON A. [INVITED] Ultrafast laser micro- and nano-processing with nondiffracting and curved beams: Invited paper for the section : Hot topics in Ultrafast Lasers[J/OL]. Optics & Laser Technology, 2016, 80: 125-137. https://www.sciencedirect.com/science/article/pii/S0030399215303923. DOI: https://doi.org/10.1016/j.optlastec.2015.11.026.

[29] BERTI N, ETTOUMI W, KASPARIAN J, et al. Reversibility of laser filamentation[J/OL]. Opt. Express, 2014, 22(17): 21061-21068. http://www.osapublishing.org/oe/abstract.cfm?URI=oe-22-17-21061. DOI: 10.1364/OE.22.021061.

[30] BERTI N, ETTOUMI W, HERMELIN S, et al. Nonlinear synthesis of complex laser waveforms at remote distances[J/OL]. Phys. Rev. A, 2015, 91: 063833. https://link.aps.org/doi/10.1103/PhysRevA.91.063833. DOI: 10.1103/PhysRevA.91.063833.

[31] DURNIN J, MICELI J J, EBERLY J H. Diffraction-free beams[J/OL]. Phys. Rev. Lett., 1987, 58: 1499-1501. https://link.aps.org/doi/10.1103/PhysRevLett.58.1499. DOI: 10.1103/PhysRevLett.58.1499.

[32] HERMAN R M, WIGGINS T A. Production and uses of diffractionless beams[J/OL]. J. Opt. Soc. Am. A, 1991, 8(6): 932-942. https://opg.optica.org/josaa/abstract.cfm?URI=josaa-8-6-932. DOI: 10.1364/JOSAA.8.000932.

[33] SCOTT G, MCARDLE N. Efficient generation of nearly diffraction-free beams using an axicon[J/OL]. Optical Engineering, 1992, 31(12): 2640-2643. https://doi.org/10.1117/12.60017. DOI: 10.1117/12.60017.

[34] BRZOBOHATÝ O, ČIŽMÁR T, ZEMÁNEK P. High quality quasi-Bessel beam generated by round-tip axicon[J/OL]. Opt. Express, 2008, 16(17): 12688-12700. https://opg.optica.org/oe/abstract.cfm?URI=oe-16-17-12688. DOI: 10.1364/OE.16.012688.

[35] JIMÉNEZ-GAMBÍN S, JIMÉNEZ N, BENLLOCH J M, et al. Generating Bessel beams with broad depth-of-field by using phase-only acoustic holograms[J/OL]. Scientific Reports, 2019, 9(1): 20104. https://doi.org/10.1038/s41598-019-56369-z. DOI: 10.1038/s41598-019-56369-z.

[36] GONG L, REN Y X, XUE G S, et al. Generation of nondiffracting Bessel beam using digital micromirror device[J/OL]. Appl. Opt., 2013, 52(19): 4566-4575. https://opg.optica.org/ao/abstract.cfm?URI=ao-52-19-4566. DOI: 10.1364/AO.52.004566.

[37] PECK E R, REEDER K. Dispersion of air[J]. J. Opt. Soc. Am, 1972, 62(8): 958.

[38] FEIT M D, FLECK J A. Effect of refraction on spot-size dependence of laser-induced breakdown[J/OL]. Applied Physics Letters, 1974, 24(4): 169-172. eprint: https://doi.org/10.1063/1.1655139. https://doi.org/10.1063/1.1655139. DOI: 10.1063/1.1655139.

[39] GORI F, GUATTARI G, PADOVANI C. Bessel-Gauss beams[J/OL]. Optics Communications, 1987, 64(6): 491-495. https://www.sciencedirect.com/science/article/pii/0030401887902768. DOI: https://doi.org/10.1016/0030-4018(87)90276-8.

# Chapter 4 Nonlinear propagation of ring-Airy beams in air beyond kilometer range

In the previous chapter, we discussed how to simultaneously control the position and length of the filament by backward propagation of the modulated laser output. By carefully tuning the parameters of a torus pulse, the generation of a femtosecond filament with fixed length can be achieved at a distance ranging from 1 to 1000 meters. However, we note that the further the location of the filament generation from the laser, the larger the radius of the required torus pulse, or the smaller the cone angle $\theta$ corresponding to its spatial phase. This brings difficulty in realization of the experimental setup. In addition, the nonlinear propagation of intense Bessel-Gauss beams with small $\theta$ leads to nonuniform filaments[1].

To reduce the size of the optical device, we introduce ring-Airy beams in this chapter. We investigate the nonlinear propagation dynamics of the beam over kilometer scales in the atmosphere. The self-reconstruction and self-acceleration properties of ring-Airy beam are crucial. Beams with small diameters can abruptly auto-focus at very long distance. Therefore, the goal of this study is to deliver the highest intensity in the focal region, making applications related to ionization and filamentation feasible. I will show how the appearance of nonlinear effects affects the position of the focus region and the distribution of the optical field, and quantify their relationship with the input power. Finally, filaments generated in the focusing region are also mentioned.

## 4.1 Introduction

About a decade ago, finite-energy ring-Airy beams were proposed as prototypical waveforms that exhibit enhanced autofocusing contrast and abruptness in the case of long focal lengths[2-3]. Due to their cubic radial phase distribution, ring Airy beams are able to undergo auto-focusing featured by an acceleration of the focusing rate around the focal point on axis, without the assist of an external lens or nonlinearity during propagation. The distribution of energy over the ring beam profile is one of the key ingredients allowing for the contrast enhancement in the region of the autofocus, hereafter called the focal region. The autofocusing property of ring Airy beams is preserved in the nonlinear regime of powerful laser beams,

opening the way to applications ranging from filamentation[4-6], high harmonic generation[7] to THz generation[8], biomedical manipulation and micromachining[9-12], and multiphoton polymerization[13]. Due to their ring structure, ring-Airy beams can also be focused beyond obstacles smaller than their ring beam radius, opening the way to applications where the target focal point lies behind an obstacle. In addition, ring Airy beams exhibit self-healing characteristics similar to those of Bessel beams, allowing for their reconstruction after encountering an obstacle[14]. Different types of ring-Airy beams have also been studied with properties related to the vorticity[15-19], coherence[20-22] and polarization[23-25].

The linear propagation dynamics and control of ring-Airy beams using different modulation method has been studied extensively: Theoretically, it is possible to precisely control the characteristics of a ring Airy beam (trajectory of the peak intensity, amplitude and width) and its focusing characteristics by carefully engineering the wavefront[26]. By modulating the spatial spectrum using a Gaussian function, the focal intensity is enhanced, the focal size is shortened, while the focal position remains virtually unchanged[27]. A similar result is obtained applying a Bessel modulation directly on the spatial profile of the ring Airy beam, leading to a shorter focal length than for an unmodulated beam[12]. The focal region can also be tailored by applying an additional conical phase in paraxial[28-29] and nonparaxial regimes[30]. Assisted with nonparaxial energy flow, the paraxial abrupt autofocusing leads to a strong enhancement in focal peak intensity, approaching the wavelength limit[31]. Beams with different initial emission angles can be superimposed to focus simultaneously on the 1st and 2nd peaks, thus influence the focal positions and intensities[32]. However, only few works deal with the nonlinear evolution of ring-Airy beams. The filamentation dynamics and corresponding wavefront evolution beyond the autofocus of a ring-Airy beam are described in[6,33]. The nonlinear propagation of ring-Airy beams with different truncation factors is also investigated[34]. To the best of our knowledge, previous research works have mainly focused propagation, whether it is linear or nonlinear, and regulation of ring-Airy beams over short-distances. Long-distance propagation of ring-Airy beams in air still have to be studied to identify properties that could be useful in potential atmospheric applications.

In this work, we focus on the nonlinear propagation dynamics of intense finite energy ring-Airy beams in the atmosphere at kilometer scales. We have thoroughly investigated the evolution of the ring-Airy beam wavefront as a function of the input power through numerical

simulations, with the goal of delivering the highest intensity in the focal region. Before the beam reaches the focal region, its intensity remains low enough for the beam to propagate almost linearly. However, when the first ring of the beam converges on the central axis, the sudden accumulation of inward energy flow leads to a large increase in light intensity, causing significant nonlinearity. A previous study has shown that the enhancement of maximum intensity or intensity contrast exceeds two orders of magnitude in linear propagation[2]. Our results show that the intensity contrast can be further amplified by the Kerr nonlinearity in the final stage of autofocusing that leads to to an enhancement by more than four orders of magnitude. The position of the nonlinear focus is determined by the total power and its ratio to the power content contained in the primary ring. An empirical formula was given in Ref.[6] that predicts the nonlinear focus shift for propagation of a few centimeters, on the basis of which we derived a modified version that is valid up to kilometer scales. Regardless the position, the induced filaments around focus are almost invariant to the input condition. The lateral size is about 100 $\mu$m, where the deposited power is always a measure of the critical power of the air.

Considering that our main goal is not the complex dynamics of filamentation, but the determination of how to control laser energy deposition at kilometric distances by utilising the autofocusing property of a ring-Airy beam. The framework of this study is thus set by the frozen pulse approximation [see section 4.2] which, besides accelerating the computation, limits the validity of our results to cases where the pulse profile effectively undergoes limited changes during propagation. The complex spatio-temporal dynamics occurring within a filament cannot be described in the framework of our frozen pulse approximation. Thus, we will restrict our simulation and analysis to the propagation range up to the auto-focus region.

### 4.1.1 Finite-energy ring-Airy beam and its linear propagation

The electric field envelope of a finite-energy ring-Airy beam is defined as:

$$\mathcal{E}(z=0,r) = \mathcal{E}_0 \mathrm{Ai}\left(\frac{r_0 - r}{w_0}\right) \exp\left(\alpha \frac{r_0 - r}{w_0}\right), \tag{4–1}$$

where Ai() is the Airy function[35], $r$ is the radial coordinate, $r_0$ and $w_0$ are the radius and scaling parameter of the primary ring, and $\alpha$ denotes the truncation factor leading to a finite power ring-Airy beam. Generation of the beam in experiments has been demonstrated in many previous works based on the Fourier transform of a modulated wavefront[3,6,36-39]. The

intensity profile of a ring-Airy beam is shown in Fig. 4–1. The amplitude of the envelope has

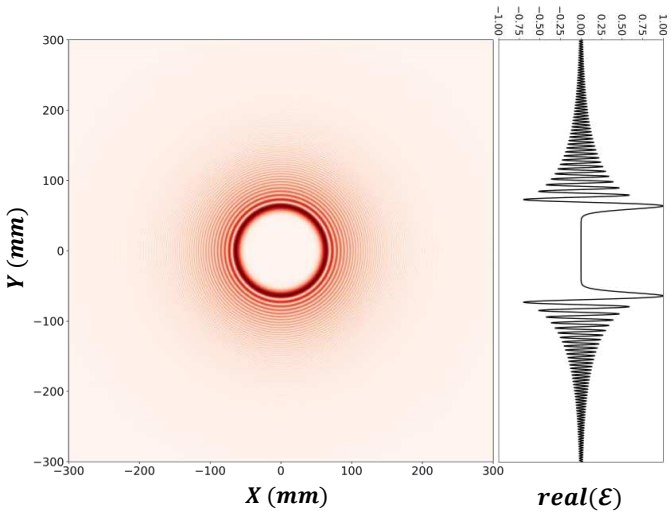


**Figure 4–1 Normalized intensity plot of a finite energy ring-Airy beam,** $w_0 = 4$ **mm,** $r_0 = 60$ **mm,** $\alpha = 0.05$**. The figure on the right is a map of the light intensity distribution sliced along the center.**

an oscillating structure, and when $r > r_0$, the oscillation decays exponentially. Meanwhile, due to the translation of the center position of the Airy function along radius, the amplitude is almost zero at $r < r_0$. Its total input power is then calculated by the following integral[2]:

$$\begin{aligned} P_{\text{in}} &= 2\pi \int_0^\infty |\mathcal{E}(r)|^2 r dr \\ &= |\mathcal{E}_0|^2 w_0^2 2\pi \int_0^\infty |\text{Ai}\left(\frac{r_0 - r}{w_0}\right) \exp\left(\alpha \frac{r_0 - r}{w_0}\right)|^2 \frac{r}{w_0} d\frac{r}{w_0} \\ &= |\mathcal{E}_0|^2 w_0^2 \sqrt{\frac{\pi}{2\alpha}} \exp(\frac{2\alpha^3}{3}) [\frac{r_0}{w_0} + \frac{1 - 4\alpha^3}{4\alpha}], \end{aligned} \tag{4–2}$$

from which we can see that for the ideal ring-Airy beam ($\alpha = 0$), the total power carried by the beam is infinite.

In linear regime, the beam propagates forward without any loss. However, its unique intensity distribution gives it self-accelerating properties when propagating. That is to say, the wavefront of the beam will bend towards the center as shown in Fig. 4–2. The inward energy flow develops slowly and is responsible for the abrupt autofocusing of the beam. The radial position of the maximum peak intensity follows a quasi-parabolic trajectory before it

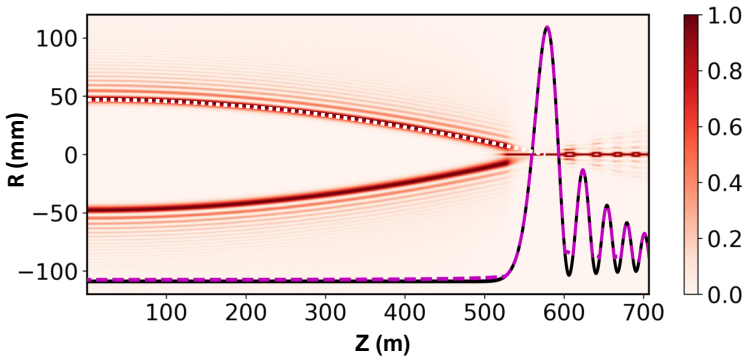


**Figure 4–2 Linear propagation of a finite energy ring-Airy beam, $w_0 = 3$ mm, $r_0 = 45$ mm, $\alpha = 0.05$, the maximum intensity is normalized to 1. The auto-focus is at $f = 565$ m. The white dotted line represents the quadratic acceleration. The magenta dashed line denotes the maximum light intensity and the black solid line denotes the light intensity in the center.**

enters the focal region similar to the case of the 1D Airy beam, which can be described as:

$$R(z) = R_0\sqrt{1-(\frac{z}{f})^2}, \tag{4–3}$$

where $R_0 \equiv r_0 - w_0 \cdot g(\alpha)$ denotes the position of the maximum intensity of the input beam, $g(\alpha)$ is equal to the first zero of the function $\mathrm{Ai}'(r) + \alpha \cdot \mathrm{Ai}(r)$. For example, $g(\alpha = 0.05) = 0.968$. The position of the auto-focus is at $f = 4z_R\sqrt{r_0/w_0 + 1}$ with the Rayleigh length $z_R \equiv k_0 w_0^2/2$[2-3,6,29].

For a given truncation factor $\alpha = 0.05$, the power content of the primary ring $P_1$ is equal to $0.4P_{\mathrm{in}}$. As the field propagates forward, the relationship between the power contained in the primary ring and the propagation distance is expressed as:

$$P_1(z) = \int_0^{r_1(z)} 2\pi r|\mathcal{E}(r,z)|^2 dr, \tag{4–4}$$

where $r_1(z)$ denotes the first point with minimum intensity outside the primary ring in radial direction. As shown in Fig. 4–3, Both the boundary $r_1(z)$ of the primary ring and its power $P_1(z)$ vary with the propagation distance. The ring Airy beam automatically focuses during linear propagation, while $P_1$ decreases slightly with increasing propagation distance. Unlike the non-truncated Airy beam exhibiting a balanced power flux with inward and outward components sustaining the power content in every ring, our input light field is modulated by a exponential function and the light field exponentially decays in the periphery, suppressing the

inward flux and resulting in the decrease of power. By calculating the energy current [shown in Fig. 4–3(b)] during propagation, we can see clearly that a small portion of the power is then progressively transferred from the interior to the exterior as a result of diffraction. Closer to the focal region, when the ring collapses and starts forming a bell-shaped beam, the numerical determination of $r_1(z)$ becomes more difficult as the primary ring disappears, the ring pattern is reorganized and the calculation of $P_1$ is less accurate.

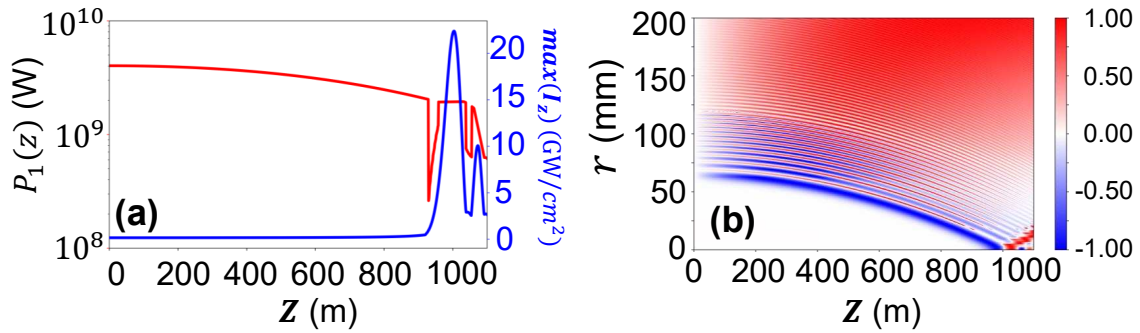


**Figure 4–3 Power content in the primary ring of a finite energy ring-Airy beam as a function of $z$. (a) The red line denotes the power content in the primary ring, the blue line denotes the on-axis intensity. (b) Energy current defined as the gradient of the phase, negative/positive values represent inward/outward flow. Beam parameters: $w_0 = 4$ mm, $r_0 = 60$ mm, $\alpha = 0.05$.**

## 4.2 Nonlinear propagation dynamics of ring-Airy beam

As mentioned in the end of the introduction, we simulate the propagation of ring-Airy beams using frozen time scheme. This implies that the dispersion of the pulse will not be taken into account and that the calculation of plasma density will be handled separately. The electric field $\mathcal{E}(r, z)$ is assumed to represent the central time slice of a laser pulse whose temporal profile is and remains Gaussian $\exp(-t^2/t_p^2)$ with duration $t_p$. The nonlinear evolution of the envelope of an electric field is described by an extended nonlinear Schrödinger equation (NLSE). Under the paraxial and slowly varying envelope approximations, the equation reads

$$\partial_z \mathcal{E} = \frac{i}{2k} \Delta_\perp \mathcal{E} + ik_0 n_2 |\mathcal{E}|^2 \mathcal{E} - \frac{\beta_K}{2} |\mathcal{E}|^{2K-2} \mathcal{E} - \frac{\sigma}{2}(1 + i\omega_0 \tau_c)\rho \mathcal{E}, \tag{4–5}$$

where the terms on the $r.h.s$ of Eq. 4–5 account for diffraction, optical Kerr effect, multiphoton absorption(MPA) and plasma defocusing. It describes the evolution of the beam profile

of the laser pulse in the reference frame of the moving pulse. The definitions of all the variables shown in 4–5 are the same as in sec 3.4.1. Parameters used in our simulations in air are summarized in Table 4–1. The critical power $P_{cr}$ for self-focusing is about 3.2 GW. Note that

**Table 4–1 Parameters used for simulations of the nonlinear propagation of the finite energy ring-Airy beam**

| | Air, 800 nm |
|---|---|
| $w_0$ (mm) | 4 |
| $r_0$ (mm) | 60 |
| $\alpha$ | 0.05 |
| $n_2$ ($m^2$/W) | $3.2 \times 10^{-23}$ |
| $\tau_c$ (fs) | 350 |
| $E_g$ (eV) | 12.1 |
| $K$ | 8 |
| $\beta^{(K)}$ ($m^{13}$/$W^7$) | $4 \times 10^{-121}$ |
| $a$ ($m^3$/s) | $5.0 \times 10^{-13}$ |

in keeping with our frozen pulse approximation, the electron density $\rho$ is calculated at every $(z, r)$ by solving Eq. (2–22) for a pulse whose maximum intensity is $|\mathcal{E}(r, z)|^2$ and temporal profile is a Gaussian function $\exp(-t^2/t_p^2)$. The computed plasma density $\rho$ as a function of intensity $I$ is shown in Fig. 4–4. The linear dependence observed in this log-logarithmic scale plot demonstrates an exponential relationship between plasma density and intensity. Also, the longer the pulse duration, the larger the plasma density produced.

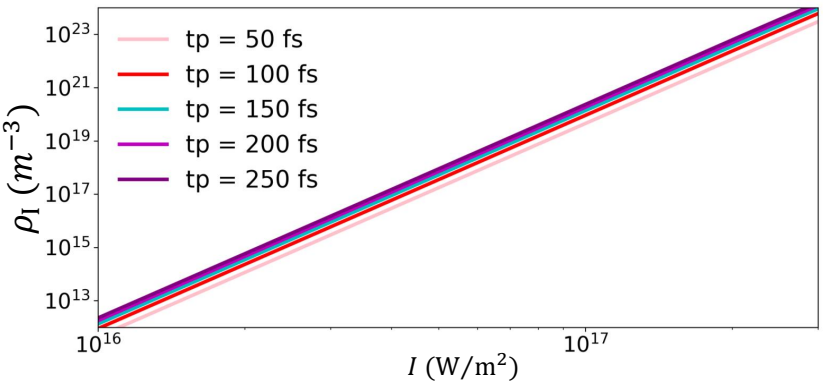


**Figure 4–4 Pre-computed plasma density as a function of intensity using the frozen pulse approximation.**

The primary ring parameters $w_0$ and $r_0$ are chosen so as to set the linear auto-focus distance at one kilometer, precisely at $f \approx 1005.3$ m. Up to the focal region, group velocity dispersion is the main effect acting on the pulse profile evolution. For an input pulse duration $t_p = 250fs$, the characteristic length of group velocity dispersion (GVD) is $L_{GVD} = t_p^2/(2k_0^{(2)}) \approx 1562.5$ m (dispersive coefficient in air $k_0^{(2)} = 20$ fs$^2$/m). Comparison between $L_{GVD}$ and $f$ justifies the neglect of dispersion in the NLSE[Eq. (4–5)][40], which amounts to keeping the pulse duration constant in our calculation. Furthermore, we can pre-chirp the input beam to compensate the dispersion during propagation in a real experiment.

Our choice of parameters was governed by the goal of reaching the highest possible intensity in the focal region while controlling its position. Linear propagation of a ring-Airy beam shows that the position of the focus corresponds to the collapse of the primary ring. In order to enhance the abruptness of this collapse, we therefore selected a parameter set allowing us to increase the power of the primary ring. Our simulations led to various situations where the beam could not properly autofocus: (i) A too high peak intensity immediately leads to ionization of air and associated nonlinear losses. (ii) A too high beam power leads to Kerr self-focusing and beam collapse in the form of a ring followed by diffraction. Our choice of parameters was thus governed by the constraints of avoiding these situations, i.e., we selected the geometric beam parameters $w_0$ and $r_0$ to fix the focal distance at 1 km while keeping a relatively large ring width. The collapse distance indeed scales as $w_0^2$ and could therefore be postponed beyond the position of the autofocus. Then we selected a truncation factor $\alpha = 0.05$, for which the power content of the primary ring $P_1$ is equal to $0.4\,P_{\text{in}}$, allowing us to perform simulations for beam powers such that the power content of the primary ring reaches up to ten critical powers for self-focusing $P_{cr}$. This is a large value that usually leads to the self-focusing and collapse of bell-shaped beams.

However, due to the distribution of power over a ring, an almost linear propagation is preserved until the focal region is approached and the abrupt stage of autofocusing begins. At this point, the ring collapse into a bell-shaped beam and the process is further accelerated by Kerr self-focusing. A detailed view of the ring collapse as well as the nonlinear Kerr effect assisted-focusing around the focal region are shown in Fig. 4–5. Fig. 4–5(b) shows how the beam profiles evolve around the first auto-focusing point during nonlinear propagation when the input power $P_{\text{in}} = 20$ GW. Clear observation of nonlinear self-focusing at 1 km is seen

in the plot of amplitude distribution. Compared with the linear energy current shown in Fig. 4–5(c), the nonlinear energy current in Fig. 4–5(d) exhibits an enhanced contrast of in & out.

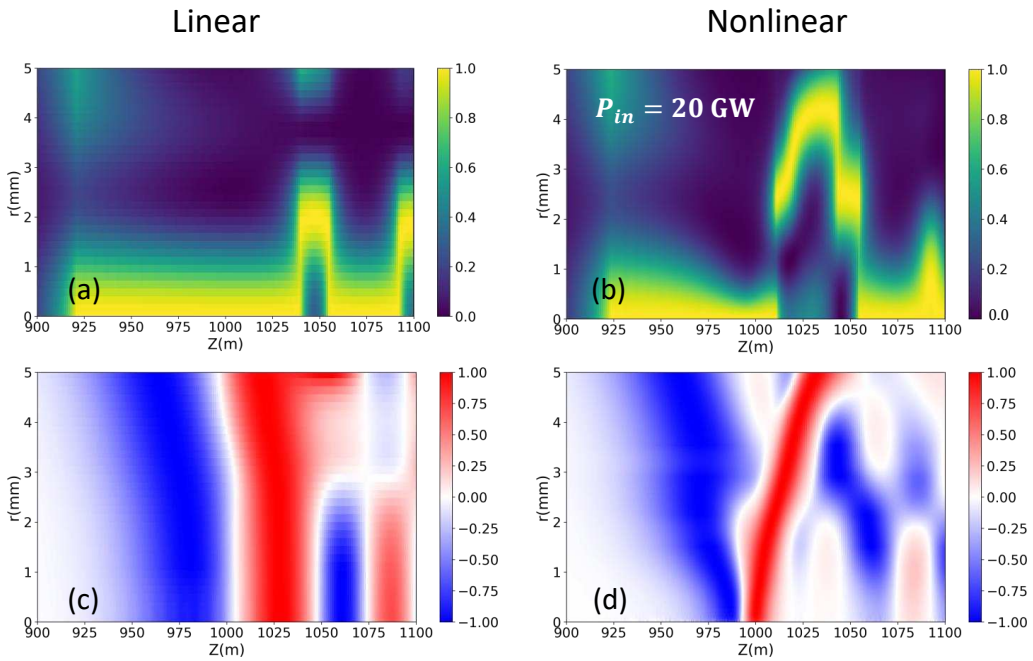


**Figure 4–5 Comparison between linear and nonlinear propagation of a finite energy ring-Airy beam around the first auto-focus. The first row shows the local intensity profile in detail. The second row is the energy current of the field, negative/positive values represent inward/outward flow. The simulation is done with $w_0 = 4$ mm, $r_0 = 60$ mm, $\alpha = 0.05$, and total power $P_{\text{in}} = 20$ GW.**

### 4.2.1 Nonlinear shift of the first auto-focus

We simulate the nonlinear propagation of a finite energy ring-Airy beam with a certain input power range. The range selection of input power is similar to the requirements of the aforementioned parameter selection, to ensure that there is a certain nonlinearity but not too outrageously large. Based on this consideration, we set the input power range from 10 GW to 110 GW, where some of the simulation results are shown in Fig. 4–6. From the results we can see that as the input power $P_{\text{in}}$ increases, the non-linear effects become more and more significant. It is worth noting that not only does the beam waist become sharper, but also the position moves backwards. Considering that we are investigating the effect of the input power on the position of the nonlinear focus and that the subsequent formation of the filament cannot

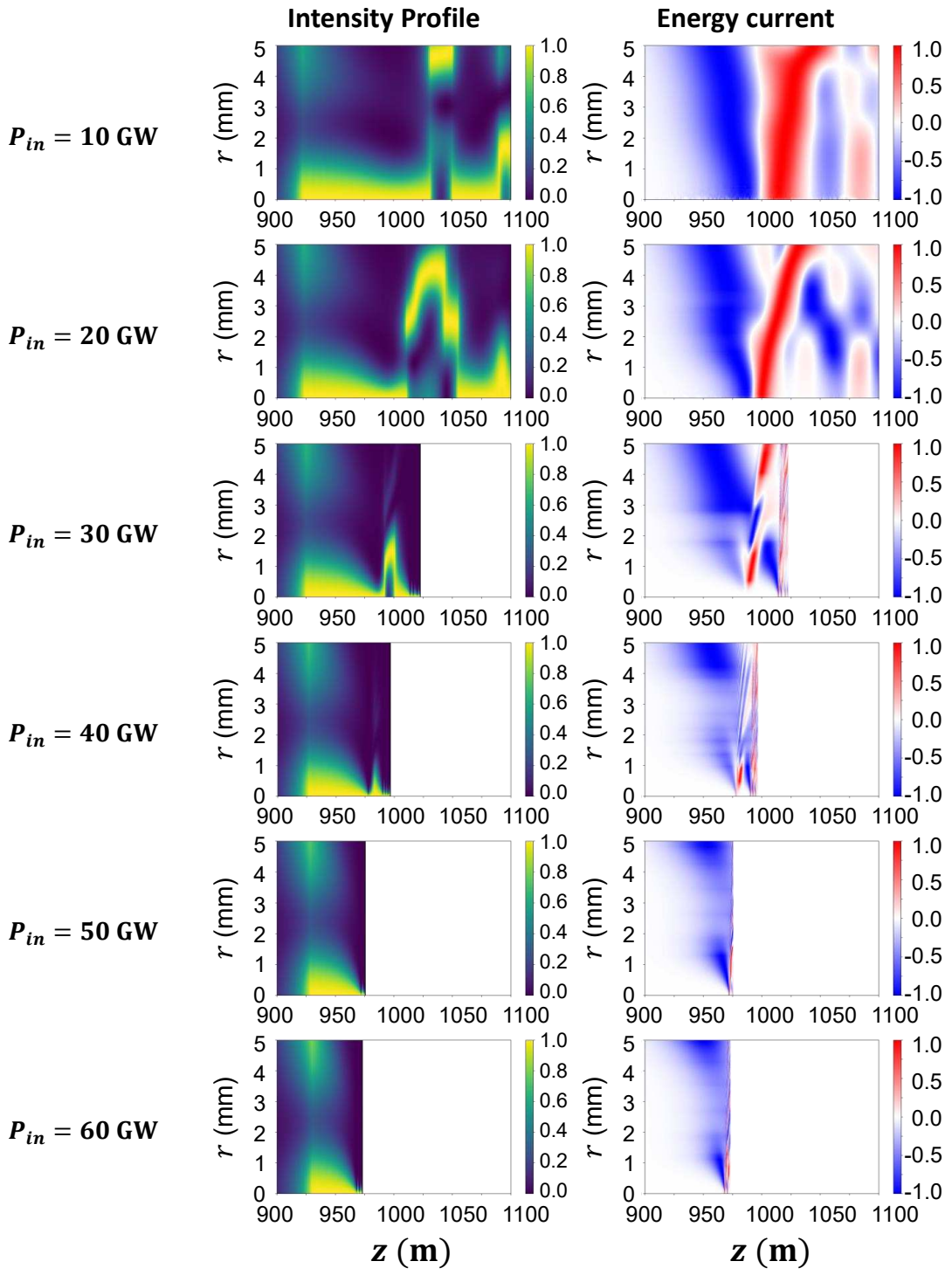


**Figure 4–6 Nonlinear evolution of the intensity profile, energy current and on-axis intensity of the beam as a function of propagation distance $z$ near the first auto-focus. The blank region in the lower panels are because our calculations were stopped early after the nonlinear focus.**

be realistically described in the frozen time approximation, we have deliberately interrupted the program early just after the beam converges on-axis.

Fig. 4–7 shows the maximum intensity as a function of propagation distance $z$ with different input powers $P_{\text{in}}$. Propagation is almost linear with a maximum intensity below ionization threshold up to the nonlinear focus. When the beam approaches the focus, the intensity contrast becomes sharper for larger input powers. However, filamentation is only obtained for input powers above 25 GW. For input powers between 25 GW and 40 GW, the nonlinear focus corresponds to a local intensity maximum but the clamped intensity characterizing a filament is only reached a few meters beyond the nonlinear focus. In this range of input powers, the inward power flux carried by the primary ring leads to a bell-shaped beam with power in excess of $P_{\text{cr}}$ while remaining too weak to induce a collapse, as a certain collapse distance is required that depend on the power content and convergence of the beam. Hence, filamentation does not start before an additional power flux, for instance from the second ring, converges to the center. When $P_{\text{in}}$ exceeds 40 GW, a sudden intensity build-up occurs and leads to filamentation starting from the nonlinear focus. We note that the position of the nonlinear focus, whether it coincides with the beginning of filamentation or not, shifts to shorter distances as the input power increases.

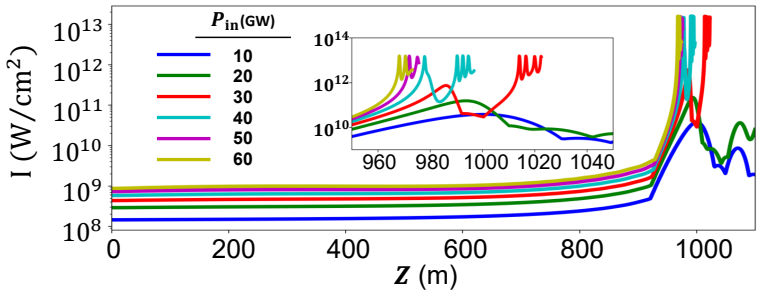


**Figure 4–7 Maximum intensity as a function of input power and propagation distance z**

By increasing the power of the input beam while keeping its maximum intensity below ionization threshold, we increase the power contained in the primary ring, thus enhancing further the final self-focusing and collapse of the bell-shaped beam resulting from the convergence of the primary ring. Higher order effects then become relevant and prevent collapse. Beyond this point a filament is generated on-axis.

As shown in Fig. 4–8, the maximum intensity contrast is enhanced by two orders of mag-

nitude compared to the case of linear propagation of a ring-Airy beam. In our simulations, the contrast increases from 150 to 80000 by increasing the input power above the filamentation threshold. For larger input powers, plasma defocusing and MPA efficiently clamps the peak intensity at the same value ($\sim$ 20 TW/cm$^2$) and the contrast drops, simply reflecting the increase of the peak intensity of the input beam.

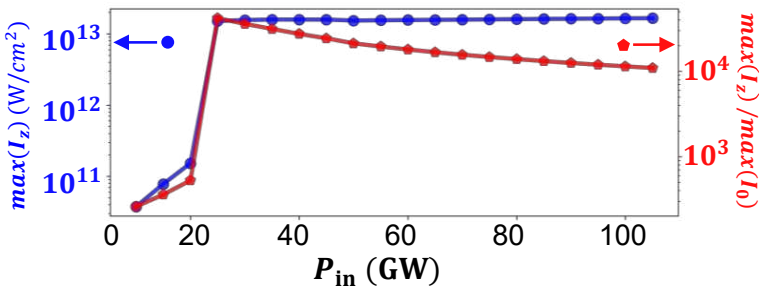


**Figure 4–8 Maximum intensity and contrast as a function of input power $P_{in}$.**

Figure 4–9(a) shows the shift of nonlinear focus as functions of the input power $P_{in}$ for three different values of the truncation factor $\alpha$. As mentioned earlier, the filament starts a few tens of centimeters beyond the nonlinear focus for moderate values of $P_{in}$, and from the nonlinear focus for higher powers. Both the position of the nonlinear focus and the filament starting point are decreasing functions of the input power $P_{in}$, or the power content of the primary ring $P_1(\alpha) \equiv \gamma_\alpha P_{in}$, and decreasing functions of $\alpha$ as well, in keeping with the fact that lower values of the truncation factor are associated with a higher inward power flux. Note that to facilitate the comparison of results obtained with different $\alpha$ correspondences, the input power is adjusted such that the power content of the primary ring $P_1$ is consistent across all values of $\alpha$.

Panagiotopoulos *et al.* have investigated the nonlinear propagation dynamics of ring-Airy beams in condensed media over short distances ($\sim$ centimeter scales)[6,33,40], and have proposed an empirical formula predicting the nonlinear focus shift. In our simulations, we observed a similar dynamics for the propagation of ring-Airy beams over kilometer scales but the empirical formula for shift of the nonlinear focus had to be adapted to these distances.

The following empirical law for the position of the nonlinear focus $f_{nf}$ matches our

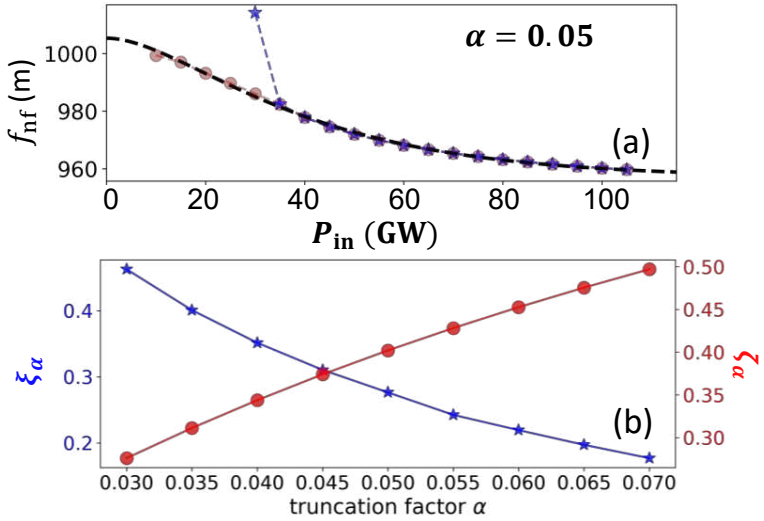


**Figure 4–9 Nonlinear shift of the first auto-focus. (a) Nonlinear focus shift (red curve, circle) and position of maximum intensity (blue curve, star) as a function of the input power, the black dashed line denotes the fitting by Eq.** (4–6), $\alpha = 0.05$. **(b) Fitting parameteres $\xi_\alpha$ (blue curve, star) and $\zeta_\alpha$ (red curve, circle) as a function of truncation factor $\alpha$.**

simulation results accurately:

$$f_{\mathrm{nf}} = f - (f - f_{\min}) \left[ 1 - \exp\left( - \left[ \zeta_\alpha \frac{\gamma_\alpha P_{\mathrm{in}}}{P_{\mathrm{cr}}} \right]^{\xi_\alpha} \right) \right]^2 , \tag{4–6}$$

where $f \equiv 4 z_R \sqrt{1 + r_0/w_0}$ is the linear focus, $f_{\min} = f\sqrt{1 - 1.5 w_0/R_0}$ is the estimated propagation distance, in which $R_0 \equiv r_0 - w_0 \cdot g(\alpha)$ is the radial location of the first intensity maximum of the ring-Airy beam, $\gamma_\alpha \equiv P_1(\alpha)/P_{\mathrm{in}}$. The exact values of $g(\alpha)$ and $\gamma_\alpha$ when $r_0/w_0 = 15$ can be found in Table 4–2. The fit is only valid up to a power limit

**Table 4–2 Truncation factor $\alpha$, $g(\alpha)$ and $\gamma_\alpha \equiv P_1/P_{\mathrm{in}}$ when $r_0/w_0 = 15$**

| $\alpha$ | 0.030 | 0.035 | 0.040 | 0.045 | 0.050 | 0.055 | 0.060 | 0.065 | 0.070 |
|---|---|---|---|---|---|---|---|---|---|
| $g(\alpha)$ | 0.987 | 0.983 | 0.980 | 0.974 | 0.968 | 0.964 | 0.957 | 0.954 | 0.949 |
| $\gamma_\alpha$ | 0.276 | 0.311 | 0.344 | 0.374 | 0.402 | 0.428 | 0.453 | 0.475 | 0.497 |

($P_{\mathrm{in}} < 100$ GW) as ring-Airy beams of larger power do self-focus and collapse onto a singular ring before reaching a nonlinear focus. Thus, the at larger powers, the nonlinear focus shift and the starting point of the filament will deviate from the trend given by Eq. (4–6). This threshold is difficult to determine exactly and can only be calibrated by numerical calculations or experiments.

In the fitting function of $f_{\mathrm{nf}}$, we also introduce an additional parameter $\zeta_\alpha$ and a coefficient $\xi_\alpha$ in the exponent for better fitting. Fig. 4–9(b) shows the quantities $\xi_\alpha$ and $\zeta_\alpha$, extracted out from numerical simulation results, as functions of the truncation factor $\alpha$ that controls how much energy from the tail of the beam can be transferred to the center. $\xi_\alpha$ is a monotonic decreasing function with gradually increasing $\alpha$. The inward power flux from the tail of the ring-Airy beam diminishes, and the power of the primary ring undergoes a comparatively stronger diffraction. This results in the decrease of $\xi_\alpha$ for larger $\alpha$, which means that the nonlinear focus will shift as a function of the input power at a slower rate. Correspondingly, when $\alpha$ increases, the numerator $\zeta_\alpha \gamma_\alpha P_{\mathrm{in}}$ in the exponent must increase in order to observe nonlinear focus shift of the same scale compared to small $\alpha$. Although $\gamma_\alpha$ increases with $\alpha$, it is not enough to counter balance with the suppress effect due to decrease of $\xi_\alpha$. So in the fitted equation, our coefficient $\zeta_\alpha$ also increases as $\alpha$ increases, as shown in Fig. 4–9(b).

### 4.2.2 Generation of filaments at kilometer scale

From the transverse beam profile shown in the top panel of Fig. 4–10, we characterized the diameter of $\approx 100$ $\mu$m for the filament after it is formed ($z > 973$ m). As can be seen from Fig. 4–10, regardless of the input power, the maximum power contained in a cylinder of radius 100 $\mu$m is $\sim 3$ GW, i.e., about $P_{cr}$ and it the same order of magnitude is obtained for the power in cylinders of larger radii of 0.5 or 1 mm, even if the power in the primary ring of the input beam is ten times larger. This results is in keeping with early observations of filaments in air[41] and is mainly due to intensity clamping within the filament[42], a phenomenon that neither depend on the input beam shape, nor on the propagation history.

## 4.3 Conclusion

In conclusion, we have studied the nonlinear propagation dynamics of finite energy ring-Airy beams at kilometer scales in air. By numerically solving the NLSE, we find that for a range of input powers up to $\sim 30$ $P_{\mathrm{cr}}$, a ring-Airy beam propagates quasi-linearly until the primary ring forms a bell-shaped beam whose convergence is accelerated as it experiences a short self-focusing stage up to a nonlinear focus. The position of the nonlinear focus is shifted to shorter distances as the input power increases. The nonlinear focus shift is also influenced

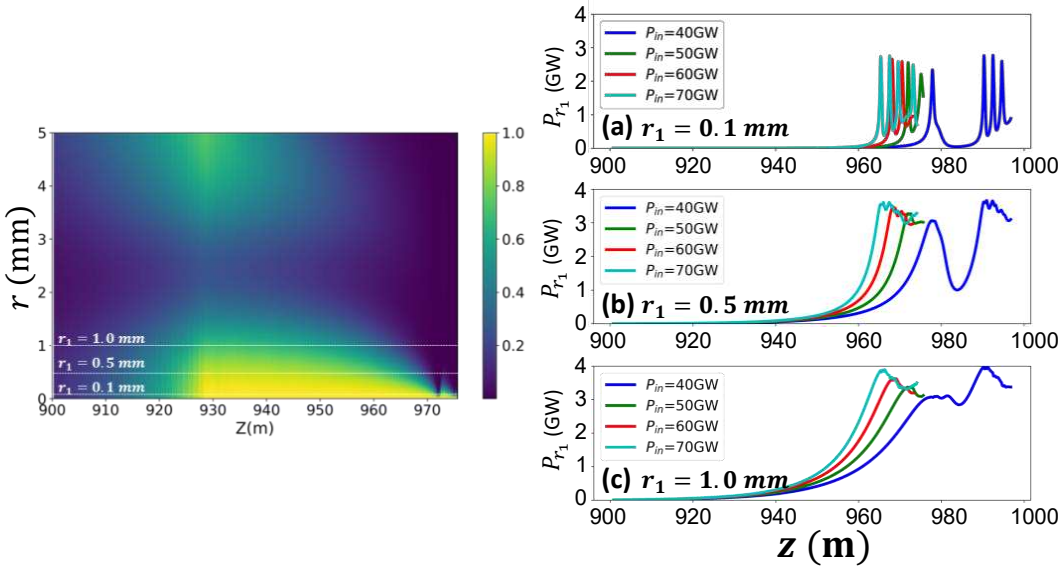


**Figure 4–10 Power contained in a beam section of radius (a) 100 $\mu$m corresponding to the filament; (b) 0.5 mm and (c) 1 mm, as a function of propagation distance, for different input powers. On the left panel is the detailed view of the intensity profile $I(r,z)$ near the nonlinear focus ($z \sim 973$ m) when $P_{\text{in}} = 50$ GW.**

by the apodization of the ring-Airy beam as its larger shifts are obtained for small truncation factors, corresponding to weakly apodized beams with a stronger inward power flux. We have proposed an empirical formula that reproduces the nonlinear focus shift obtained in numerical simulations over a range of powers above $P_{\text{cr}}$, thus predicting the position of the starting point of filamentation and the highest intensity. Beyond this point, a plasma string is generated by the pulse, whose highly nonlinear dynamics cannot be described by our model. Nevertheless, our results show that the power localized in the filament and in a cylindrical region ten times wider than the filament diameter is roughly $P_{\text{cr}}$ and therefore, the plasma string formed at the nonlinear focus cannot be extended further than a few tens of centimeters. In contrast with the projection scheme based on Bessel-beams, the length and uniformity of the plasma string is here limited by the power threshold above which the primary ring undergoes a singular ring collapse before the nonlinear focus is reached. Hence, the interest of the present projection scheme based on ring-Airy beams lies in its ability to deliver a power density of 20 TW/cm$^2$ on a target located at kilometric distances.

It is worth noting that input powers required to initiate filamentation in air at a distance of 1 km by using a ring-Airy beam only requires tens of GW, which is at least one

order of magnitude lower than the terawatt laser pulses used in previous works[43-47]. We hope our findings will contribute to the development of laser beam and pulse shaping for the transmission of high laser energy densities to remote targets in the atmosphere and related atmospheric applications.

## Bibliography

[1] POLESANA P, FRANCO M, COUAIRON A, et al. Filamentation in Kerr media from pulsed Bessel beams[J/OL]. Phys. Rev. A, 2008, 77: 043814. https://link.aps.org/doi/10.1103/PhysRevA.77.043814. DOI: 10.1103/PhysRevA.77.043814.

[2] EFREMIDIS N K, CHRISTODOULIDES D N. Abruptly autofocusing waves[J/OL]. Opt. Lett., 2010, 35(23): 4045-4047. https://opg.optica.org/ol/abstract.cfm?URI=ol-35-23-4045. DOI: 10.1364/OL.35.004045.

[3] PAPAZOGLOU D G, EFREMIDIS N K, CHRISTODOULIDES D N, et al. Observation of abruptly autofocusing waves[J/OL]. Opt. Lett., 2011, 36(10): 1842-1844. https://opg.optica.org/ol/abstract.cfm?URI=ol-36-10-1842. DOI: 10.1364/OL.36.001842.

[4] POLYNKIN P, KOLESIK M, MOLONEY J V, et al. Curved Plasma Channel Generation Using Ultraintense Airy Beams[J/OL]. Science, 2009, 324(5924): 229-232. eprint: https://www.science.org/doi/pdf/10.1126/science.1169544. https://www.science.org/doi/abs/10.1126/science.1169544. DOI: 10.1126/science.1169544.

[5] POLYNKIN P, KOLESIK M, MOLONEY J. Filamentation of Femtosecond Laser Airy Beams in Water[J/OL]. Phys. Rev. Lett., 2009, 103: 123902. https://link.aps.org/doi/10.1103/PhysRevLett.103.123902. DOI: 10.1103/PhysRevLett.103.123902.

[6] PANAGIOTOPOULOS P, PAPAZOGLOU D G, COUAIRON A, et al. Sharply autofocused ring-Airy beams transforming into non-linear intense light bullets[J/OL]. Nature Communications, 2013, 4(1): 2622. https://doi.org/10.1038/ncomms3622. DOI: 10.1038/ncomms3622.

[7] KOULOUKLIDIS A D, PAPAZOGLOU D G, FEDOROV V Y, et al. Phase Memory Preserving Harmonics from Abruptly Autofocusing Beams[J/OL]. Phys. Rev. Lett., 2017, 119: 223901. https://link.aps.org/doi/10.1103/PhysRevLett.119.223901. DOI: 10.1103/PhysRevLett.119.223901.

[8] LIU K, KOULOUKLIDIS A D, PAPAZOGLOU D G, et al. Enhanced terahertz wave emission from air-plasma tailored by abruptly autofocusing laser beams[J/OL]. Optica, 2016, 3(6): 605-608. https://opg.optica.org/optica/abstract.cfm?URI=optica-3-6-605. DOI: 10.1364/OPTICA.3.000605.

[9] ZHANG P, PRAKASH J, ZHANG Z, et al. Trapping and guiding microparticles with morphing autofocusing Airy beams[J/OL]. Opt. Lett., 2011, 36(15): 2883-2885. https://opg.optica.org/ol/abstract.cfm?URI=ol-36-15-2883. DOI: 10.1364/OL.36.002883.

[10] LU W, SUN X, CHEN H, et al. Abruptly autofocusing property and optical manipulation of circular Airy beams[J/OL]. Phys. Rev. A, 2019, 99: 013817. https://link.aps.org/doi/10.1103/PhysRevA.99.013817. DOI: 10.1103/PhysRevA.99.013817.

[11] LIANG Y, LIANG G, XIANG Y, et al. Manipulation and Assessment of Human Red Blood Cells with Tunable "Tug-of-War" Optical Tweezers[J/OL]. Phys. Rev. Appl., 2019, 12: 064060. https://link.aps.org/doi/10.1103/PhysRevApplied.12.064060. DOI: 10.1103/PhysRevApplied.12.064060.

[12] LU F, WU H, LIANG Y, et al. Bessel-modulated autofocusing beams for optimal trapping implementation[J/OL]. Phys. Rev. A, 2021, 104: 043524. https://link.aps.org/doi/10.1103/PhysRevA.104.043524. DOI: 10.1103/PhysRevA.104.043524.

[13] MANOUSIDAKI M, PAPAZOGLOU D G, FARSARI M, et al. Abruptly autofocusing beams enable advanced multiscale photo-polymerization[J/OL]. Optica, 2016, 3(5): 525-530. https://opg.optica.org/optica/abstract.cfm?URI=optica-3-5-525. DOI: 10.1364/OPTICA.3.000525.

[14] HU Y, ZHANG P, LOU C, et al. Optimal control of the ballistic motion of Airy beams[J/OL]. Opt. Lett., 2010, 35(13): 2260-2262. https://opg.optica.org/ol/abstract.cfm?URI=ol-35-13-2260. DOI: 10.1364/OL.35.002260.

[15] DAVIS J A, COTTRELL D M, SAND D. Abruptly autofocusing vortex beams[J/OL]. Opt. Express, 2012, 20(12): 13302-13310. https://opg.optica.org/oe/abstract.cfm?URI=oe-20-12-13302. DOI: 10.1364/OE.20.013302.

[16] JIANG Y, HUANG K, LU X. Propagation dynamics of abruptly autofocusing Airy beams with optical vortices[J/OL]. Opt. Express, 2012, 20(17): 18579-18584. https://opg.optica.org/oe/abstract.cfm?URI=oe-20-17-18579. DOI: 10.1364/OE.20.018579.

[17] LI P, LIU S, PENG T, et al. Spiral autofocusing Airy beams carrying power-exponent-phase vortices[J/OL]. Opt. Express, 2014, 22(7): 7598-7606. https://opg.optica.org/oe/abstract.cfm?URI=oe-22-7-7598. DOI: 10.1364/OE.22.007598.

[18] ZHANG X, LI P, LIU S, et al. Autofocusing of ring Airy beams embedded with off-axial vortex singularities[J/OL]. Opt. Express, 2020, 28(6): 7953-7960. https://opg.optica.org/oe/abstract.cfm?URI=oe-28-6-7953. DOI: 10.1364/OE.387961.

[19] JIANG Y, ZHAO S, YU W, et al. Abruptly autofocusing property of circular Airy vortex beams with different initial launch angles[J/OL]. J. Opt. Soc. Am. A, 2018, 35(6): 890-894. https://opg.optica.org/josaa/abstract.cfm?URI=josaa-35-6-890. DOI: 10.1364/JOSAA.35.000890.

[20] JIANG Y, YU W, ZHU X, et al. Propagation characteristics of partially coherent circular Airy beams[J/OL]. Opt. Express, 2018, 26(18): 23084-23092. https://opg.optica.org/oe/abstract.cfm?URI=oe-26-18-23084. DOI: 10.1364/OE.26.023084.

[21] LI T, LI D, ZHANG X, et al. Partially coherent radially polarized circular Airy beam[J/OL]. Opt. Lett., 2020, 45(16): 4547-4550. https://opg.optica.org/ol/abstract.cfm?URI=ol-45-16-4547. DOI: 10.1364/OL.397993.

[22] LI T, ZHANG X, HUANG K, et al. Experimental generation of partially coherent circular Airy beams[J/OL]. Optics & Laser Technology, 2021, 137: 106814. https://www.sciencedirect.com/science/article/pii/S003039922031447X. DOI: https://doi.org/10.1016/j.optlastec.2020.106814.

[23] LIU S, WANG M, LI P, et al. Abrupt polarization transition of vector autofocusing Airy beams[J/OL]. Opt. Lett., 2013, 38(14): 2416-2418. https://opg.optica.org/ol/abstract.cfm?URI=ol-38-14-2416. DOI: 10.1364/OL.38.002416.

[24] YE D, PENG X, ZHOU M, et al. Simulation of generation and dynamics of polarization singularities with circular Airy beams[J/OL]. J. Opt. Soc. Am. A, 2017, 34(11): 1957-1960. https://opg.optica.org/josaa/abstract.cfm?URI=josaa-34-11-1957. DOI: 10.1364/JOSAA.34.001957.

[25] CHEN M, HUANG S, SHAO W. Tight focusing of radially polarized circular Airy vortex beams[J/OL]. Optics Communications, 2017, 402: 672-677. https://www.sciencedirect.com/science/article/pii/S0030401817305655. DOI: https://doi.org/10.1016/j.optcom.2017.06.089.

[26] GOUTSOULAS M, EFREMIDIS N K. Precise amplitude, trajectory, and beam-width control of accelerating and abruptly autofocusing beams[J/OL]. Phys. Rev. A, 2018, 97: 063831. https://link.aps.org/doi/10.1103/PhysRevA.97.063831. DOI: 10.1103/PhysRevA.97.063831.

[27] GENG T, ZHANG X. Propagation properties of the circular Airy beam with a Gaussian envelope in Fourier space[J/OL]. Opt. Express, 2020, 28(2): 2447-2455. https://opg.optica.org/oe/abstract.cfm?URI=oe-28-2-2447. DOI: 10.1364/OE.384143.

[28] ZHANG J, LI Y, TIAN Z, et al. Controllable autofocusing properties of conical circular Airy beams[J/OL]. Optics Communications, 2017, 391: 116-120. https://www.sciencedirect.com/science/article/pii/S0030401817300457. DOI: https://doi.org/10.1016/j.optcom.2017.01.027.

[29] MANSOUR D, PAPAZOGLOU D G. Tailoring the focal region of abruptly autofocusing and autodefocusing ring-Airy beams[J/OL]. OSA Continuum, 2018, 1(1): 104-115. https://opg.optica.org/osac/abstract.cfm?URI=osac-1-1-104. DOI: 10.1364/OSAC.1.000104.

[30] LU W, CHEN H, LIU S, et al. Circular Airy beam with an arbitrary conical angle beyond the paraxial approximation[J/OL]. Phys. Rev. A, 2022, 105: 043516. https://link.aps.org/doi/10.1103/PhysRevA.105.043516. DOI: 10.1103/PhysRevA.105.043516.

[31] MANOUSIDAKI M, FEDOROV V Y, PAPAZOGLOU D G, et al. Ring-Airy beams at the wavelength limit[J/OL]. Opt. Lett., 2018, 43(5): 1063-1066. https://opg.optica.org/ol/abstract.cfm?URI=ol-43-5-1063. DOI: 10.1364/OL.43.001063.

[32] WANG Y, JIANG Y. Dual autofocusing circular Airy beams with different initial launch angles[J/OL]. Journal of Quantitative Spectroscopy and Radiative Transfer, 2022, 278: 108010. https://www.sciencedirect.com/science/article/pii/S002240732100501X. DOI: https://doi.org/10.1016/j.jqsrt.2021.108010.

[33] PANAGIOTOPOULOS P, COUAIRON A, KOLESIK M, et al. Nonlinear plasma-assisted collapse of ring-Airy wave packets[J/OL]. Phys. Rev. A, 2016, 93: 033808. https://link.aps.org/doi/10.1103/PhysRevA.93.033808. DOI: 10.1103/PhysRevA.93.033808.

[34] JIANG Q, SU Y, MA Z, et al. Nonlinear manipulation of circular Airy beams[J/OL]. Applied Physics B, 2019, 125(6): 105. https://doi.org/10.1007/s00340-019-7218-8. DOI: 10.1007/s00340-019-7218-8.

[35] BERRY M V, BALAZS N L. Nonspreading wave packets[J/OL]. American Journal of Physics, 1979, 47(3): 264-267. eprint: https://doi.org/10.1119/1.11855. https://doi.org/10.1119/1.11855. DOI: 10.1119/1.11855.

[36] WANG F, ZHAO C, DONG Y, et al. Generation and tight-focusing properties of cylindrical vector circular Airy beams[J/OL]. Applied Physics B, 2014, 117(3): 905-913. https://doi.org/10.1007/s00340-014-5908-9. DOI: 10.1007/s00340-014-5908-9.

[37] QIAN Y, LAI S, MAO H. Generation of High-Power Bottle Beams and Autofocusing Beams[J]. IEEE Photonics Journal, 2018, 10(1): 1-7. DOI: 10.1109/JPHOT.2018.2799165.

[38] CHREMMOS I D, ZHANG P, PRAKASH J, et al. Fourier-space generation of abruptly autofocusing beams and optical bottle beams.[J]. Optics letters, 2011, 36(18): 3675-7.

[39] 王晓章, 唐峰, 原勐捷, 等. 实验模拟环形艾里光束在大气扰动中的光束漂移[J]. 中国激光, 2015, 42(8).

[40] PANAGIOTOPOULOS P, ABDOLLAHPOUR D, LOTTI A, et al. Nonlinear propagation dynamics of finite-energy Airy beams[J]. Phys. Rev. A, 2012, 86: 013842.

[41] BRAUN A, KORN G, LIU X, et al. Self-channeling of high-peak-power femtosecond laser pulses in air[J/OL]. Opt. Lett., 1995, 20(1): 73-75. http://opg.optica.org/ol/abstract.cfm?URI=ol-20-1-73. DOI: 10.1364/OL.20.000073.

[42] KASPARIAN J, SAUERBREY R, CHIN S. The critical laser intensity of self-guided light filaments in air[J]. Appl. Phys. B, 2000, 71: 877-879.

[43] HOUARD A, WALCH P, PRODUIT T, et al. Laser-guided lightning[J/OL]. Nature Photonics, 2023. https://doi.org/10.1038/s41566-022-01139-z. DOI: 10.1038/s41566-022-01139-z.

[44] MÉCHAIN G, C.D’ Amico, ANDRÉ Y B, et al. Range of plasma filaments created in air by a multi-terawatt femtosecond laser[J/OL]. Optics Communications, 2005, 247(1): 171-180. https://www.sciencedirect.com/science/article/pii/S0030401804011812. DOI: https://doi.org/10.1016/j.optcom.2004.11.052.

[45] DURAND M, HOUARD A, PRADE B, et al. Kilometer range filamentation[J/OL]. Opt. Express, 2013, 21(22): 26836-26845. http://opg.optica.org/oe/abstract.cfm?URI=oe-21-22-26836. DOI: 10.1364/OE.21.026836.

[46] KASPARIAN J, ACKERMANN R, ANDRÉ Y B, et al. Electric events synchronized with laser filaments in thunderclouds[J]. Opt. Express, 2008, 16(8): 5757-5763.

[47] GOFFIN A, LARKIN I, TARTARO A, et al. Optical Guiding in 50-Meter-Scale Air Waveguides[J/OL]. Phys. Rev. X, 2023, 13: 011006. https://link.aps.org/doi/10.1103/PhysRevX.13.011006. DOI: 10.1103/PhysRevX.13.011006.

# Chapter 5 Online composite analysis in potash with LIBS coupled with machine learning

In the previous two chapters we detailed how the generation of specific filaments in air can be achieved by modulating the light field distribution. After obtaining the desired filament, based on the interaction of the filament with the medium, we may detect and analyze the substance at a distance. Among many possible applications, filament assisted laser induced break-induced spectroscopy (LIBS) is one of the most attractive because of its advantages of non-contact, real-time and high sensitivity. However, the quality of the collected LIBS spectra is greatly influenced by both chemical and physical matrix effect, which greatly reduces the accuracy of quantitative analysis. Therefore, it is not enough to know how to remotely control and produce good filaments for LIBS applications, we also need to be able to address the impact and challenges of various external factors on the collected spectrum signals.

## 5.1 Introduction

An essential component for plant growth is potassium. By taking part in enzyme activation, the production of different organic molecules (carbohydrates and proteins), the control of water and nutrient transport, and other processes, it influences the plant life cycle[1]. Crop productivity is hampered by a lack of potassium in agricultural soil, necessitating the use of potash fertilizer to supplement potassium[2]. Potash is a non-renewable resource that can only be created by mining potash ores or extracting from salt lakes. It cannot be made from other compounds. Almost 90 million tons (40 million tons of potassium oxide $K_2O$ equivalent) of mass production are organized annually[3].

To optimize the production process, conserve raw materials and energy, and regulate the quality of the finished products, particularly the concentrations of potassium and water in them for commercial trades, it is crucial for the potash production industry to characterize the raw and transformed materials during the production. The current method of examination involves taking samples from the production line and testing them offline in a lab on site. As is the case in China[4-5], the technique is governed by national standards, giving it legal value and making it crucial for large-scale industry production, associated commercial

activities, and end uses. The Chinese standards specifically state, among other things, that the equivalent $K_2O$ wt% concentration $c_{K_2O}$ should be measured using the tetraphenylboron sodium gravimetric method[6] with a tolerated absolute bias less than 0.38% for replicate measurements in the same laboratory, and less than 0.80% when measurements from different laboratories are compared. The conversion from $c_{K_2O}$ to the concentration of $c_{KCl}$ is done through $c_{KCl} = \frac{74}{47} c_{K_2O}$, as is the measurement tolerance bias. Whereas mass loss should be used to calculate the water concentration ($c_{H_2O}$) when heating the material below 105°C, with an absolute bias of less than 0.20% for replicate measurements.

The assessment of the potassium concentration in potash also employs spectrochemical analytical methods, such as atomic absorption spectrometry (AAS)[7], inductively coupled plasma-optical emission spectrometry (ICP-OES)[7], and inductively coupled plasma-mass spectrometry (ICP-MS)[8]. These techniques' exceptional analytical capabilities and the related operating circumstances make them appropriate for laboratory analysis. Yet, it is necessary to move toward online and automatic characterisation of processed materials in the potash fertilizer manufacturing chain in order to advance factory management system and production process automation. Prompt gamma neutron activation analysis (PGNAA) is one of the element analytical methods that allows for online detection. However, this method has some limitations in terms of limited sensitivity and radioactive safety concerns[9]. The online mode of X-ray fluorescence (XRF) can be employed with a high sensitivity for heavy metals[10]. When exposed to light components like potassium in potash, it becomes less sensitive. Again, using ionizing radiation would reduce the appeal of XRF for online industrial analysis.

Due to its distinctive characteristics, laser-induced breakdown spectroscopy (LIBS) provides a high potential for online detection and analysis[11]. Many industrial applications, particularly for the inspection and analysis of items on a conveyer belt, have been made possible by recent advancements in the approach[12]. Several university laboratories and R&D firms have proposed and evaluated the use of LIBS for potash fertilizer characterisation. With a laboratory size conveyer belt system with raw samples obtained from production facilities in Russia, Belarus, and Israel (51 samples), a first assessment of the viability of LIBS for potash fertilizer online characterisation has been reported, particularly when compared to PGNAA and XRF The outcomes showed how LIBS may be used to determine all the ele-

ments in potash that are important for industrial process control in real time. More recently, a study focused on the development and optimization of a multivariate model using random forest (RF), using a laboratory LIBS setup with 53 samples obtained from Salt Lake in Qinghai Province in China and prepared in compressed pellets after dehydration by heating and homogenization in an agate mortar[13]. The outcomes demonstrated the effectiveness of the potash LIBS spectral treatment using a multivariate calibration approach. More generally, several machine learning methods[14-19], such as back-propagation neural networks (BPNN)[15] and convolutional neural networks[20-21], have been used to the analysis of LIBS spectrum data (CNN).

Using a specially designed LIBS instrument put online above a conveyer belt of a production factory in Salt Lake, Qinghai province, China, we report simultaneous measurement of $H_2O$ and KCl concentrations in final product potash fertilizer. Offline measurements (with 119 samples) were carried out using manual samplings at regular intervals of about an hour, followed by analysis in the on-site laboratory using the aforementioned procedures outlined by the national standards, while LIBS measurements were carried out continuously at a rate of 3 Hz throughout the manual sampling period. As a result of the correlation between the offline analysis data and the online collected LIBS spectra, it was possible to develop multivariate calibration models for $H_2O$ and KCl that were based on machine learning and used the CNN and BPNN algorithms. Online acquisition of LIBS spectra on a conveyer belt implies unavoidable additional spectrum fluctuations due to changes in the surface position of moving materials, and most importantly variation of moisture in the produced fertilizer due to instability of the production process, in comparison to the aforementioned previous works on LIBS analysis of potash fertilizer. This fluctuation causes a shift in the matrix effect in the LIBS spectra, which has a big impact on how accurate KCl can be determined. So, to extract the concentration of $H_2O$ and then that of KCl with precision that meets the requirements of the national standards, efficient machine learning regression models are essential. We will first rapidly review the developed online measurement LIBS setup, the related operating settings, and the outcomes of the offline analysis of $H_2O$ and KCl in the sections that follow. Then, univariate calibration curves with K I emission lines will be shown, highlighting significant experimental fluctuations and disturbances brought on by changes in the concentration of $H_2O$ in the materials under study. The construction of machine learning-based

models will be explored in detail prior to the presentation of their analytical performances, especially in comparison with the related requirements of the national standards.

## 5.2 Principle of laser-induced breakdown spectroscopy

A graphical illustration of the principle of laser-induced breakdown spectroscopy is shown in Fig. 5–1. It involves several complicated interaction processes between laser and matter. When a intense pulsed laser illuminates and focus on the surface of an object. Atoms and molecules near the laser and material's contact surface absorb the incident photons and energy. In this localized region, the energy is rapidly transformed into heat, resulting in an increase in temperature, ablation of the material, melting, and the creation of vapor near the surface. This procedure takes roughly tens of nanoseconds. The produced material vapor absorbs further electromagnetic radiation, causing the temperature to keep increasing until the plasma is generated, at which point the temperature can reach as high as 20,000K. At this early stage of generation of plasma, the electron density in the plasma is so high that the spectral lines we measure will be dominated by mainly due to free-free transitions of electrons. We will observe a broad continuum background showing no specific line features. Then, the plasma plume will quickly expand and decay, recombinations and de-excitations of electrons and ions of specific elements result in the unique emission lines. Finally, emission lines as well as the continuum background diminish as the plasma cools down and temperature decreases. In this procedure, the plasma's lifetime is determined by the input laser, the ambient pressure, and the substance. Generally, it is in the range of 0.5-10 $\mu$s.

Figure 5–2 illustrates the behavior of emission spectra at various time scales, as previously described. Now, with the proper spectrometer, it is possible to concurrently capture all emission lines of various elements for elemental analysis. This is the core of laser-induced breakdown spectroscopy.

## 5.3 Online LIBS measurements and sampling information

Online measurement was implemented using a LIBS setup. As shown schematically in Fig. 5–3(a), the optical configuration was quite classical. Quantel Ultra 100, a small, industrial-grade Q-switched Nd:YAG laser, produced 100 mJ-equivalent fundamental laser

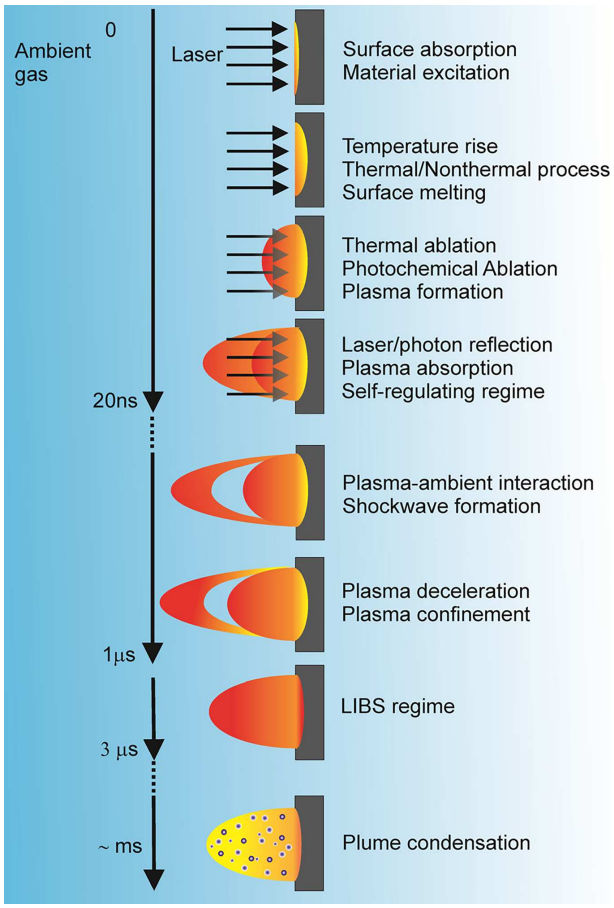


**Figure 5–1 Schematic of the processes of laser-induced breakdown spectroscopy at different time scales. Image is taken from ref.[22].**

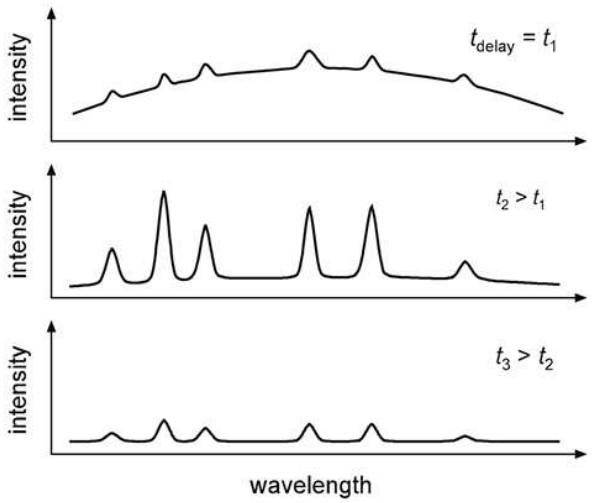


**Figure 5–2 Schematic of the emission spetra of laser-induced breakdown spectroscopy at different time scales. Image is taken from ref.[11].**

pulses at a repetition rate of 3 Hz. A lens with a focus length of 500 mm in normal incidence was utilized to direct laser pulses toward potash particles using a wide bandwidth high reflection mirror. The LIBS spectral intensity was strongly impacted by variations in the powder surface. By making the surface relatively flat with a scraper, the influence was reduced. The laser pulse focusing lens backward collimated the emission from the produced plasma and the broad bandwidth mirror directed it toward a dichroic filter, which reflected it away from the laser pulses. The collimated emission was then concentrated into an optical fiber using a signal focusing lens with a focus length of 100 mm. A compact CCD spectrometer (AvaSpec-Mini, Avantes) with a spectral range of 350 nm to 830 nm and a resolution of roughly 1.0 nm was attached to the final one. A laser pulse was used to synchronize the

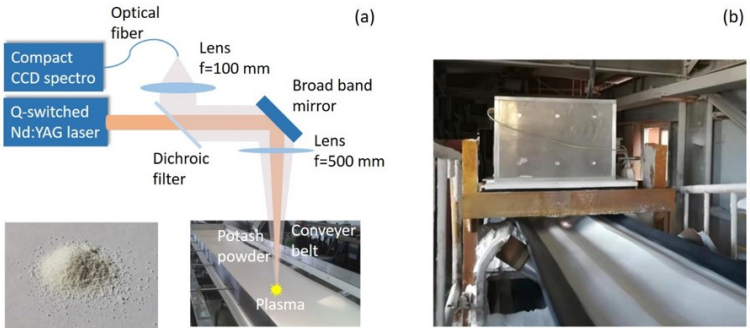


**Figure 5–3 Schematic presentation of the used online experimental setup (a) and a picture of the installation on a production conveyer belt in the factory in Salt Lake in Qinghai Province China (b).**

CCD. A photo of the LIBS system mounted on an industrial conveyer belt of a factory in Salt Lake, Qinghai, China, is also shown in Fig. 5–3(b). After being installed, the system operated continuously, enabling the collection of 3 LIBS spectra per second. A one-hour interval was used for manual sample collection at the same time. A soup spoon was used to remove a bulk of potash from the production line for each collection, weighing around 100 g. As required by the factory's operating regulations, the gathered materials were tested in the on-site laboratory using the procedures outlined in the national standards stated in the introduction. The collections were done over the course of six consecutive days ( D1 - D6 ).

**Table 5–1 Sample information and offline data for the concentration of $H_2O$ and KCl in wt%**

| Sampling no. | Sampling time | Concentration(wt%) | | Sampling no. | Sampling time | Concentration(wt%) | |
|---|---|---|---|---|---|---|---|
| | | $H_2O$ | KCl | | | $H_2O$ | KCl |
| 1 | D1-T3 | 0.14 | 95.12 | 61 | | 0.12 | 94.80 |
| 2 | | 0.08 | 96.10 | 62 | | 0.26 | 95.02 |
| 3 | D1-T4 | 0.10 | 95.15 | 63 | D4-T3 | 0.22 | 94.96 |
| 4 | | 0.14 | 95.20 | 64 | | 0.10 | 94.20 |
| 5 | | 0.10 | 95.08 | 65 | | 0.24 | 94.18 |
| 6 | | 0.08 | 94.40 | 66 | | 0.10 | 94.96 |
| 7 | | 0.10 | 94.88 | 67 | | 0.08 | 95.08 |
| 8 | | 0.06 | 95.10 | 68 | | 0.10 | 95.10 |
| 9 | D2-T1 | 0.08 | 95.12 | 69 | | 0.16 | 95.18 |
| 10 | | 0.12 | 95.16 | 70 | D4-T4 | 0.08 | 95.22 |
| 11 | D2-T2 | 0.10 | 95.15 | 71 | | 0.10 | 95.00 |
| 12 | | 0.10 | 95.10 | 72 | | 0.06 | 95.14 |
| 13 | | 0.06 | 95.17 | 73 | | 0.12 | 95.18 |
| 14 | | 0.10 | 95.12 | 74 | | 0.26 | 95.02 |
| 15 | | 0.08 | 95.10 | 75 | | 0.10 | 94.70 |
| 16 | | 0.10 | 95.16 | 76 | | 0.22 | 94.57 |
| 17 | | 0.08 | 95.04 | 77 | | 0.14 | 94.80 |
| 18 | | 0.10 | 95.14 | 78 | | 0.10 | 94.70 |
| 19 | | 0.38 | 95.10 | 79 | | 0.16 | 95.10 |
| 20 | | 0.44 | 95.14 | 80 | | 0.52 | 94.86 |
| 21 | D2-T3 | 0.52 | 95.04 | 81 | | 0.18 | 93.86 |
| 22 | | 0.12 | 95.12 | 82 | | 0.20 | 92.85 |
| 23 | | 0.14 | 95.20 | 83 | | 0.16 | 93.04 |
| 24 | | 0.26 | 95.24 | 84 | | 0.24 | 92.22 |
| 25 | | 0.30 | 95.16 | 85 | D5-T1 | 0.22 | 92.10 |
| 26 | | 0.12 | 95.04 | 86 | | 0.42 | 92.40 |
| 27 | | 0.16 | 95.04 | 87 | | 0.50 | 93.80 |
| 28 | | 0.10 | 95.12 | 88 | | 1.88 | 93.25 |
| 29 | | 0.52 | 95.10 | 89 | | 1.56 | 94.31 |
| 30 | | 0.26 | 95.18 | 90 | | 0.62 | 93.52 |
| 31 | | 0.32 | 95.26 | 91 | | 0.32 | 94.10 |
| 32 | | 0.18 | 95.30 | 92 | | 0.22 | 93.20 |

continued next page

continued table 5–1

| Sampling no. | Sampling time | Concentration(wt%) $H_2O$ | Concentration(wt%) KCl | Sampling no. | Sampling time | Concentration(wt%) $H_2O$ | Concentration(wt%) KCl |
|---|---|---|---|---|---|---|---|
| 33 | | 0.12 | 95.16 | 93 | | 0.16 | 94.88 |
| 34 | | 0.10 | 95.24 | 94 | D5-T2 | 0.10 | 95.04 |
| 35 | D3-T2 | 0.10 | 95.12 | 95 | | 0.28 | 94.88 |
| 36 | | 0.12 | 95.10 | 96 | | 0.32 | 94.52 |
| 37 | | 0.10 | 94.24 | 97 | | 0.20 | 95.10 |
| 38 | | 0.10 | 94.62 | 98 | D5-T3 | 0.16 | 94.64 |
| 39 | | 0.10 | 95.06 | 99 | | 0.22 | 94.50 |
| 40 | | 0.16 | 94.70 | 100 | | 0.34 | 94.26 |
| 41 | | 0.10 | 94.52 | 101 | | 0.30 | 93.72 |
| 42 | D3-T3 | 0.10 | 94.56 | 102 | | 0.12 | 95.10 |
| 43 | | 0.14 | 94.50 | 103 | D6-T2 | 0.10 | 95.04 |
| 44 | | 0.10 | 94.22 | 104 | | 0.12 | 95.15 |
| 45 | | 0.12 | 94.10 | 105 | | 0.08 | 95.08 |
| 46 | | 0.12 | 95.20 | 106 | | 0.22 | 94.82 |
| 47 | | 0.08 | 95.00 | 107 | | 0.26 | 94.65 |
| 48 | | 0.10 | 94.40 | 108 | | 0.54 | 95.10 |
| 49 | | 0.10 | 94.62 | 109 | D6-T3 | 0.80 | 94.70 |
| 50 | | 0.10 | 94.50 | 110 | | 0.74 | 94.88 |
| 51 | | 0.08 | 94.26 | 111 | | 0.86 | 95.10 |
| 52 | D3-T4 | 0.08 | 95.10 | 112 | | 0.70 | 95.06 |
| 53 | | 0.10 | 94.62 | 113 | | 0.54 | 94.92 |
| 54 | | 0.14 | 94.20 | 114 | | 0.36 | 94.50 |
| 55 | | 0.10 | 94.80 | 115 | | 0.42 | 94.64 |
| 56 | D4-T2 | 0.10 | 95.04 | 116 | | 0.44 | 94.36 |
| 57 | | 0.16 | 94.96 | 117 | D6-T4 | 0.28 | 94.92 |
| 58 | | 0.22 | 95.12 | 118 | | 0.30 | 95.10 |
| 59 | D4-T3 | 0.34 | 94.40 | 119 | | 0.22 | 95.04 |
| 60 | | 0.20 | 93.66 | | | | |

Table 5–1 lists the details of the data collection and on-site laboratory analysis of $H_2O$ and KCl. The timing of sample collection is specified as T1: 00:00 to 05:59, T2: 06:00 to 11:59, T3: 12:00 to 17:59, and T4: 18:00 to 23:59, during the course of a 24-hour period. The

gathered samples and their laboratory analytical data were linked to the continually recorded LIBS spectra. An observation made at the factory showed that the product's moisture level changed quite quickly over a period of several minutes. Since the collection time was accurate to the minute, we opted to link each sample obtained to the LIBS spectra recorded in the interval of ± 1 minute. Therefore, we considered that $120 \times 3 = 360$ LIBS spectra would correspond to the materials with statistically equivalence , particularly for the concentrations of $H_2O$ and KCl within the precisions of their respective measurements, for calibration model training and validation.

## 5.4 Raw spectra and the influence due to water

In Fig. 5–4, online LIBS spectra are shown for four manual samplings (n°13, n°58, n°86, and n°112 in Table 5–1), with different $H_2O$ concentrations. The main emission lines are identified with the NIST spectra database and indicated in the figure: K, Na, Ca, Mg, Li, Sr, H and O. Due to the high concentration of KCl in the sample, the K I 766.5 nm and 769.9 nm lines self-reverse in a detailed view at 767.5 nm. Each of the presented spectrum is the average

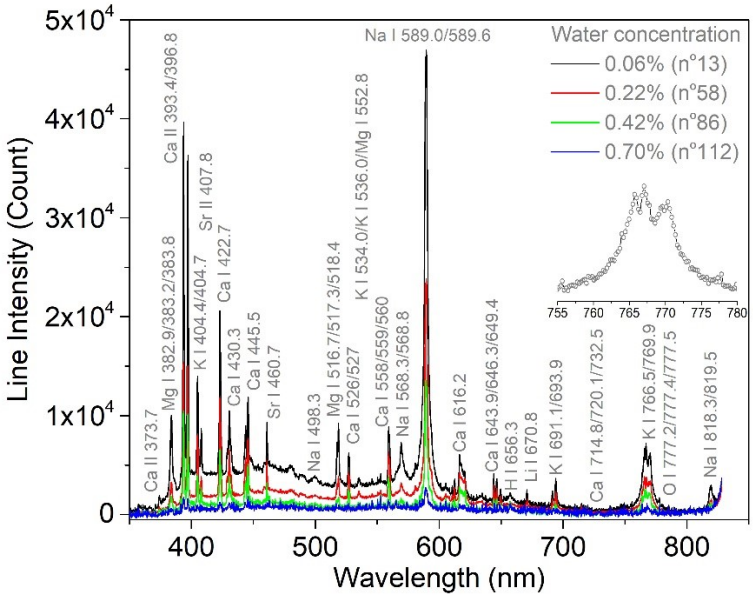


**Figure 5–4 Average online LIBS spectra for four manual samples of the product at various levels of moisture.**

of 360 single laser shot raw spectra acquired at a rate of 3 Hz over a period of 2 minutes, each of which is connected to a specific offline sampling and laboratory analysis. Identification of the primary spectral features in the relevant spectral range with the NIST atomic spectrum database[23] reveals emission lines from the main elements present in potash, including K, Na, Ca (also ionic lines), Mg, Li, and Sr (also ionic lines), as well as gas elements, H and O, which are also present in the atmosphere. We can observe that they are strongly influenced by the moisture of the product because both the line intensities and the spectral continuum decrease as the $H_2O$ concentration rises. Particularly, the H I 656.3 nm line exhibits a decorrelation with product moisture as its intensity drops with increasing $H_2O$ content. This means that we are unable to create the calibration curve for $H_2O$ concentration determination with the associated hydrogen line using the conventional laboratory based method. The approach of spectrochemical analysis by correlation is used in this work to investigate the relationship between the moisture of the sample and the overall behavior of a LIBS spectrum[19].

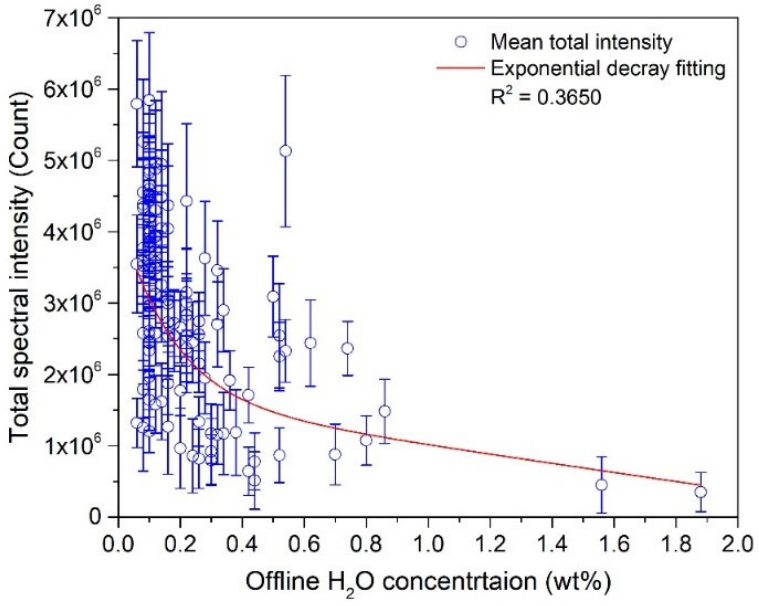


**Figure 5–5 Univariate modeling of the concentration of $H_2O$ based on average total spectral intensities. The error bars represent the single shot spectra's standard deviation.**

Figure 5–5 displays average total spectral intensity corresponding to different manual samplings as a function of the related $H_2O$ concentration. The standard deviation is calculated

by:

$$\sigma_X^2 = \mathbb{E}(X - \mathbb{E}[X])^2 = \mathbb{E}[X^2] - (\mathbb{E}[X])^2. \tag{5–1}$$

As the $H_2O$ concentration rises, we can see that the total spectral intensity globally drops, supporting the findings from Fig. 5–4. The total intensity of the spectra's relationship to the product's $H_2O$ content can be shown by fitting using an exponential decay function. We also note that the experimental points' $R^2 = 0.3650$ dispersion with regard to the exponential decay is fairly high. Hence, it would not be possible to determine the $H_2O$ concentration precisely by simply correlating the overall spectral intensity with it.

## 5.5 Univariate analysis and results on KCl

The emission lines from the potassium element can be used to characterize the KCl to be found in potash for this purpose in a LIBS spectrum. Figure 5–4 presents three groups of K I lines that were detected in the recorded spectra: K I 404.4 and 404.7 nm lines, K I 766.5 and 769.9 nm lines, and K I 691.1 and 693.9 nm lines (L3). According to the spectroscopic data from the NIST database, L1 and L3 are resonant lines and should be significantly impacted by self-absorption. This is particularly true of L1, as both of its lines clearly display self-reversal behavior. Although they are significantly less intense, the L2 lines are not resonant lines.

We used the L2 lines instead of the K I lines since they should be less impacted by self-absorption in a univariate calibration model. As a function of the offline KCl concentration for the 119 offline samplings, Fig. 5–6(a) shows the average raw intensity of the L2 lines (peak intensity minus the background). With regard to the linear regression and a relatively low $R^2$ value, we can observe a significant dispersion of the average intensities. The intensity that is normalized to the total spectral intensity (integration of the area under the spectrum) is displayed in Fig. 5–6(b). Even as the $R^2$ value rises, the normalized average intensities yet again show a fairly large dispersion. The results are shown in Figs. 5–6(c) and (d), which were obtained by first normalizing the background intensity with that of the Mg I 383 nm line and then with that of the Ca I 423 nm line. In comparison to the raw data, the normalized data exhibits a higher correlation with the linear regression. Due to the large impact of the product's moisture, the extremely low $R^2$ values obtained still do not allow the calibrated models to have quantitative analytical ability.

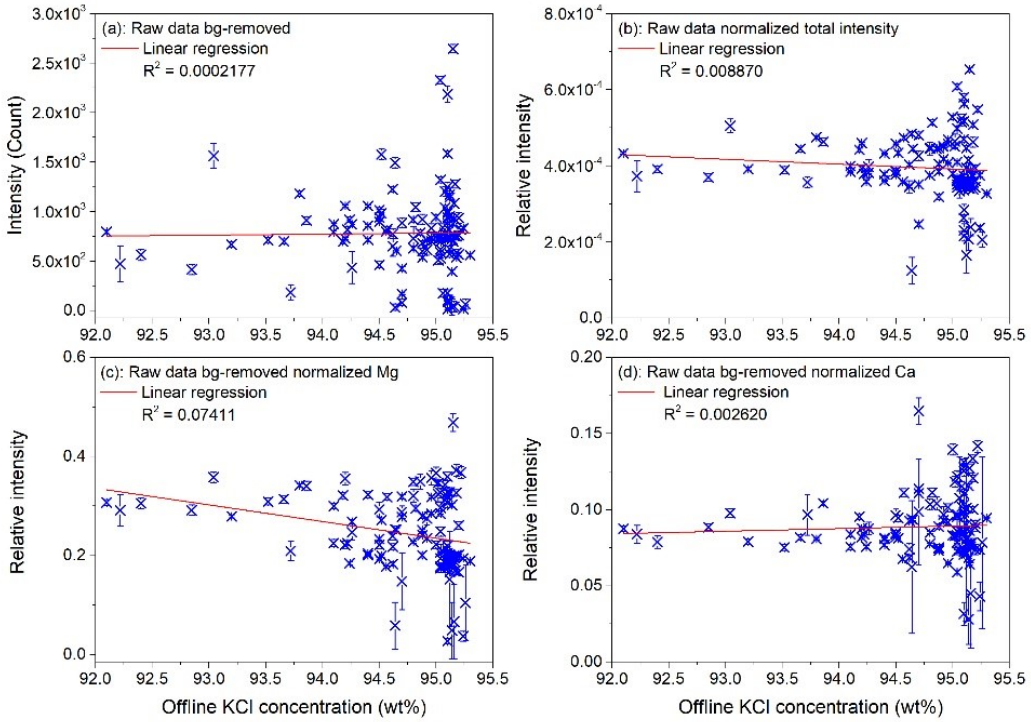


**Figure 5–6 Average intensity of the L2 lines around 692 nm as a function of the offline concentration for different manual samplings. The error bars correspond to standard deviation over the single shot spectra. (a) background-removed raw intensity; (b) raw intensity normalized by total spectral intensity; (c) background-removed raw intensity normalized by Mg I 383 nm line; (d) background-removed raw intensity normalized by Ca I 423 nm line.**

## 5.6 Machine learning-based multivariate calibration model

### 5.6.1 Flow chart of algorithm and data processing

Therefore, it is required to explore a multivariate method that can effectively determine the concentrations of $H_2O$ and KCl from online LIBS spectra. Considering that the influence of water on the spectrum is quite global, influencing both the background and all spectral lines (not only the associated H I and O I lines), it can be regarded as a matrix effect when determining KCl concentration. By investigating the overall association between a LIBS spectrum and the $H_2O$ concentration of the associated sample, our plan was to first identify the $H_2O$ concentration and then use it as the additional dimension in the generalized spectrum to predict the KCl concentration. Figure 5–7 depicts a flowchart of multivariate

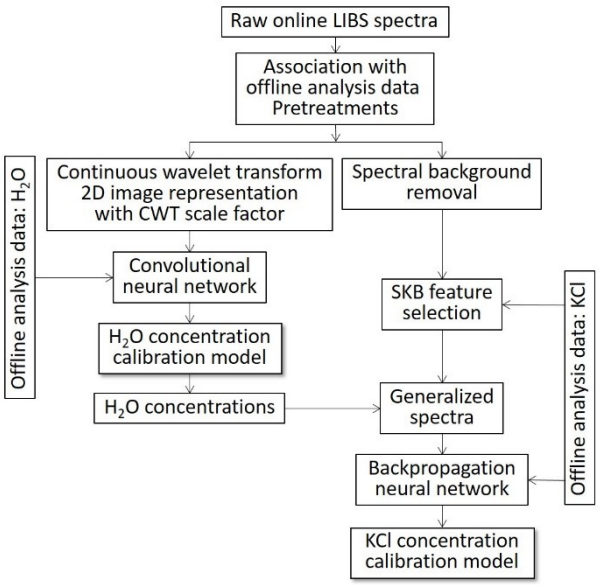


**Figure 5–7 Training and validation algorithm flowchart for machine learning-based multivariate calibration models.**

model training and validation that was utilized in our research. As previously noted, each offline analysis data set was matched to the online LIBS spectra that were collected in intervals of 2 minutes around the sampling time, yielding a total of 360 single shot spectra: $2 \times 60 \times 3 = 360$. An algorithm that measures the intensity of the Na I 589 nm lines was used identifying about 10 spectra that abnormally displayed low intensities as a result of experimentally unexpected circumstances. A particular spectrum that had an excessively low intensity at 589 nm and was similar to the spectral background was eliminated. The remain-

ing spectra were then averaged to reduce fluctuation by grouping single shot spectra based on when they were acquired into subsequent packages for averaging. This produced 6 successive average spectra for processing for the $H_2O$ concentration calibration model and 10 successive average spectra for processing for the KCl concentration calibration model. Due to instability in the drying process and nonuniformity in the materials, we observed a quicker change in the product's moisture using in-situ observations at the manufacturing site. Considering KCl changed slowly during manufacturing, we decided to average a larger ensemble of spectra for the training of the $H_2O$ concentration calibration model. The overall number of valid spectra for a given set of offline analysis data varied slightly, therefore for the $H_2O$ and KCl model training, the total number was divided by 6 or 10 accordingly. The quotient that was obtained controlled how many spectra from the ensemble of spectra corresponding to a specific offline analysis would be included in the packages for averaging, and the reminder showed which spectra were not employed. The subsequent steps for training the $H_2O$ and KCl concentration calibration model used the generated 6 or 10 average spectra for each offline set of data.

For the assessment of the multivariate calibration models, the following parameters will be used: coefficient of determination $R^2$, relative error of calibration (REC), relative error of prediction (REP), standard deviation (RSD), and limit of detection (LOD). their detailed definitions are listed below:

$$R^2 = 1 - \frac{RSS}{TSS}, \tag{5–2a}$$

$$REC/REP(\%) = \frac{X_{C/P} - X}{X}, \tag{5–2b}$$

$$RSD(\%) = \frac{\sigma_X}{\mathbb{E}[X]} \times 100, \tag{5–2c}$$

$$LOD = \frac{3\sigma_a}{b}, \tag{5–2d}$$

in which RSS denote the sum of squared residuals and TSS the total sum of squares of the calibration data, $X_{C/P}$ the prediction value using calibration and validation data with $X$ the true values, $\sigma_X$ the standard deviation of data sequence $X$, $\sigma_a$ the standard deviation of $a$ and $b$ the slope in a linear fitting $y = a + bx$.

### 5.6.2 Calibration model for water concentration

Based on the information presented in Figs. 5–4 and 5–5, we know that the product's moisture affects the behavior of the entire spectrum, the continuum spectral background as well as the emission lines, although the directly related H I line has no direct correlation with $H_2O$ concentration. Studying the relationship between the full spectrum and the $H_2O$ concentration using machine learning seems to be the only viable method for developing a calibration model[19]. The correlation to the water concentration can be made more clear if the original spectrum is further expanded along an extra axis, such as its frequency channel, which can explicitly indicate the change in its aspect due to the change in $H_2O$ concentration of the product. Continuous wavelet transform (CWT) is helpful for this development since it gives an overcomplete signal representation[24]. The signal's expansion is implemented as shown below:

$$\mathbb{S}(\Delta, \Lambda) = \int_{-\infty}^{+\infty} s(\lambda) \frac{1}{\sqrt{\Delta}} \psi(\frac{\lambda - \Lambda}{\Delta}) d\lambda, \tag{5–3}$$

where $s(\lambda)$ is an averaged LIBS spectrum, $\mathbb{S}(\Delta, \Lambda)$ its coefficient of CWT, $\psi$ the mother function with $\Delta > 0$ corresponding to the scale parameter (spectral window in nm), and $\Lambda$ the translation parameter (center of the spectral window in nm). In order for the numerical values of CWT to more accurately depict the global aspect of the spectrum, the mother function should be chosen to mirror the shape of the spectral peaks in the initial spectrum. It is for this reason that the Mexican hat wavelet was selected as the mother function of CWT, as it has also been effectively employed for Raman spectrum analysis[24]. The analytical expression is:

$$\psi(x) = \frac{2}{\sqrt{3}} \pi^{-1/4} (1 - x^2) \exp(-\frac{x^2}{2}), x \equiv \frac{\lambda - \Lambda}{\Delta}. \tag{5–4}$$

Figure 5–8 depicts a typical average spectrum as a function of $\lambda$ (Fig. 5–8(b)) and its CWT coefficients as a function of $\Lambda$ and $\Delta$ (Fig. 5–8(a), normalized to the positive maximum) Spectrum-images of CWT coefficients were loaded into a convolutional neural network (CNN) for regression on offline $H_2O$ concentration data. CNNs are a type of deep neural networks that are most often used to analyze visual information[25]. Typical applications include image and video recognition, image classification, medical image analysis, and natural language processing. In this study, we chose to build a CNN-based regression model utilizing CWT spectrum-images due to CNN's optimized capacity to extract the most signifi-

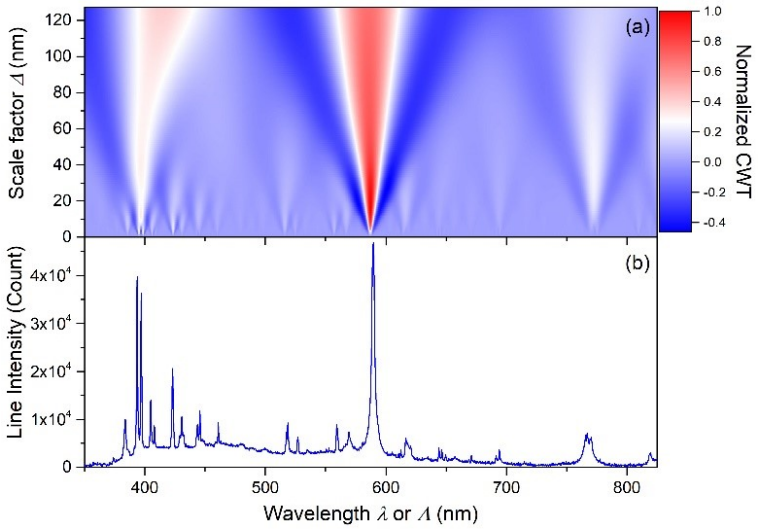


**Figure 5–8 Continuous wavelet transformation coefficients (a) of an average spectrum (b).**

cant features from the input images based on the desired outcome, as well as its independence from prior knowledge and human effort in feature selection. In contrast to an image recognition and classification challenge, the objective of optimization in this study was regression. This means that, following the selection of features, they are loaded into neural networks for an optimization process that would result in a regression model capable of minimizing the mean squared error (MSE) between the model-predicted values and the offline analysis data for the ensemble of training spectrum-images.

In the implementation of the aforementioned CNN-based regression model training and validation, a training data set consisting of 101 groups of six spectrum-images and their associated 101 offline $H_2O$ concentrations was selected. Validation data comprised the remaining 18 groups of 6 spectrum-images and their associated offline $H_2O$ concentrations. The corresponding sample numbers of these groups in Table 5–1 are [4, 11, 17, 22, 25, 27, 20, 32, 33, 39, 45, 56, 63, 72, 23, 82, 85, 86, 96, 110]. During the training phase with the training data set, a cross-validation approach (with a dynamic separation of training data and testing data) was utilized to maximize the model's overall performance while minimizing overfitting. In this process, the CNN's hyperparameters (number of layers and number of filters in each layer) and model parameters (connecting weights) were adjusted constantly. The optimized network shown in Fig.5–9 exhibited a good structure with a reduced level of complexity, hence minimizing the possibility of overfitting. It consists of four convolutional layers ac-

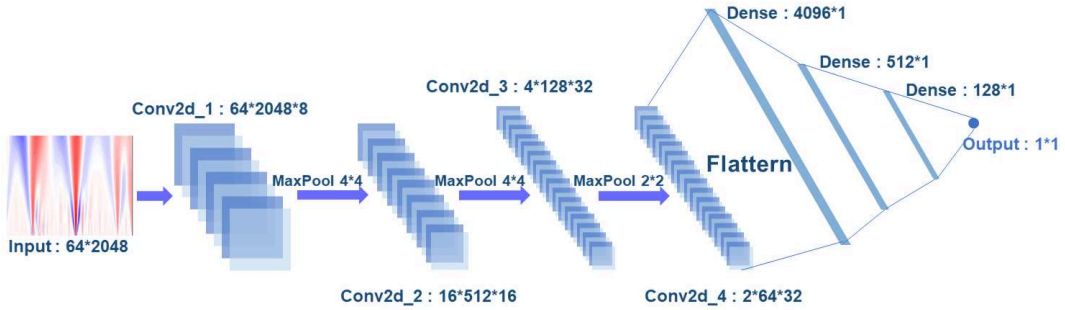


**Figure 5–9 Structure of the convolutional neural network.**

companied with maxpooling process and three dense layers. Activcation function is set to be 'relu' which means rectified linear activation function. It is a piecewise linear function with the following properties:

$$f(x) = x^+ = \max(0, x) = \begin{cases} x & \text{if } x > 0, \\ 0 & \text{otherwise.} \end{cases}, \tag{5–5}$$

$$f'(x) = \begin{cases} 1 & \text{if } x > 0, \\ 0 & \text{if } x < 0. \end{cases}, \tag{5–6}$$

where x is the input argument of an neuron in the network. The connection between the fourth layer and the first dense layer is build through flatterning of the feature matrix. The input of the network is the CWT coefficients and the output is the predicted water concentration.

Given that the $H_2O$ concentration of the most of the calibration data ranges from 0.0 to 1.0 wt%, an effort was made for a reasonably uniform redistribution of the $H_2O$ concentration of the validation data set for validation purposes. The two offline $H_2O$ concentrations (for n° 88 and n° 98 in Table 5–1) were omitted from the validation set because they were the only data points above the concentration of 1.0 wt% and the amount of the calibration data in this range was so few.

The resulting performance of $H_2O$ model is presented in Fig. 5–10 after the structure of CNN has been optimized. Here, we can see the calibration model with the projected concentrations for the calibration data set as a function of the offline data (in blue cross) as well as the linear regression (in blue straight line). We can observe an excellent $R^2$ of 0.9887 and a linear regression slope of 1.0335, which is quite close to the ideal case. The validation points between offline data and model predictions are also shown in the picture (in orange

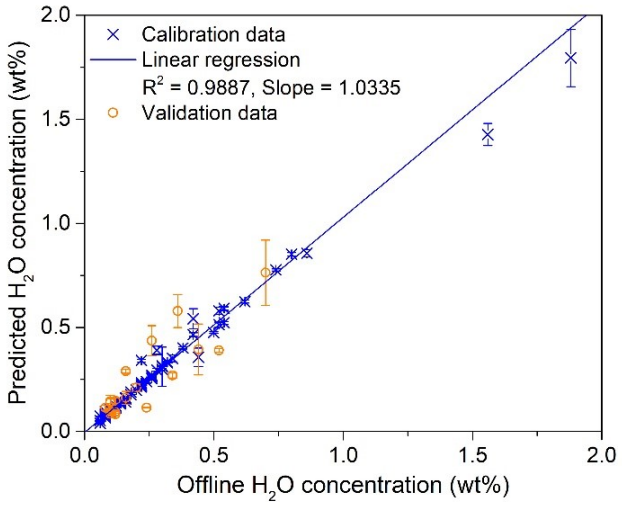


**Figure 5–10 Performance of the multivariate calibration model of $H_2O$ based on CNN.The calibration data for the model training, together with the linear regression, are shown in blue cross and blue straight line, respectively. The validation data is shown in an orange circle. For a specific offline study, the error bars in the image show the ± standard deviation of the model predicted concentrations among the 6 average spectra.**

circles), demonstrating strong agreement with the calibration model. The figure's error bars represent the standard deviation of the predicted values for the six average spectra.

Table 5–2 additionally includes additional figures of merit that were computed and displayed. A REC of 5.828% and a LOD of 0.0416 wt% are shown. Regarding the prediction performances, RSD remains within a reasonable range while REP reaches a value of 31.05%, which is significantly higher than REC. A deeper look at the picture reveals a decline in the

**Table 5–2 Parameters assessing the performances of the multivariate calibration model for $H_2O$**

| Calibration model | | | Prediction performance | |
|---|---|---|---|---|
| $R^2$ | REC(%) | LOD(wt%) | REP(%) | RSD(%) |
| 0.9887 | 5.828 | 0.0416 | 31.05 | 5.63 |

model's ability to predict outputs, particularly at $H_2O$ concentrations greater than or equal to 0.25 weight percent, where the quantity of training data diminishes. This gives us reason to believe that adding more offline analysis data with a more uniform distribution across the range of $H_2O$ concentrations under consideration would improve model prediction accuracy

and result in a smaller REP.

We also compared the offline analytical results with the model-predicted $H_2O$ concentrations for the calibration and validation sets, based to which we were able to calculate the bias of the prediction (the difference between the value predicted by the model and the value obtained via offline analysis), which we then compared to the requirement in the Chinese national standard (GB6549-2011)[4]. Figure 5–11 displays the results, and it is obvious that

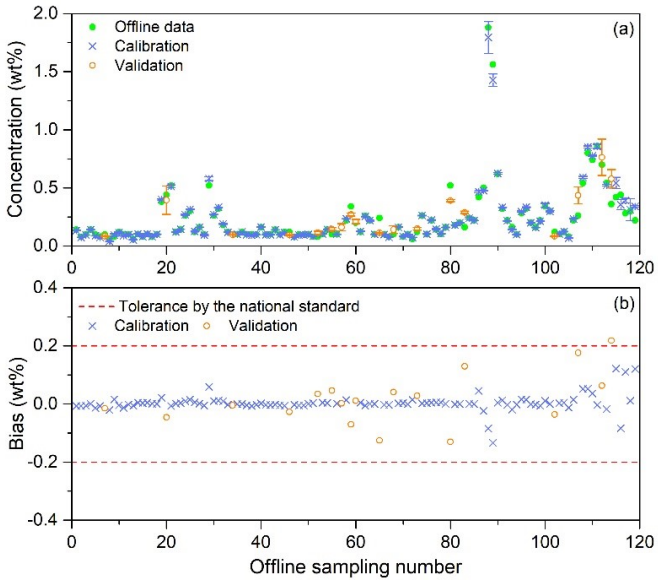


**Figure 5–11 (a) Comparison between the model-predicted water concentration and the offline analysis data; (b) presentation of the prediction bias (difference between the model-predicted value and the offline analysis value) and comparison with the requirement of the national standard, absolute bias $\leqq 0.2\%$ for $H_2O$**

almost all of the predicted $H_2O$ concentrations meet the requirements of the national standard, attesting to the model's effectiveness.

### 5.6.3 Baseline correction and feature selection

According to the flowchart, spectral background correction was performed on the average spectra first. Baseline correction is a common preprocessing step in many analytical techniques, such as spectroscopy, chromatography, and electrochemistry. The purpose of baseline correction is to remove the systematic drift or noise present in the signal that is not related to the analyte of interest. Here are some commonly used baseline correction methods:

1. Straight-line fitting method: The simplest baseline correction method is to fit a straight

line to the baseline and subtract it from the original signal. This method assumes that the baseline is a linear function of the independent variable. This method is easy to implement but may not be appropriate if the baseline is nonlinear[26].

2. Polynomial fitting method: This method fits a polynomial function to the baseline and subtracts it from the original signal. The degree of the polynomial can be varied depending on the complexity of the baseline. This method can handle nonlinear baselines and is widely used in spectroscopy and chromatography[27].
3. Moving average method: This method smooths the baseline by averaging over a moving window of data points. The window size can be adjusted to optimize the tradeoff between smoothing and resolution. This method is computationally efficient and useful for removing high-frequency noise[28].
4. Wavelet transform method: This method uses wavelet transform to decompose the signal into different frequency components. The baseline is then estimated from the low-frequency components and subtracted from the original signal. This method is robust to noise and can handle nonstationary signals[24,29].

Considering their unique characteristics, the proposed and implemented approach for our LIBS spectra relates to continuous wavelet transform-based method. It includes peak detection combined with derivative peak-width estimates and polynomial fitting of spectral background for an optimum correction over the entire spectral range. First of all, CWT accurately calculates peak positions in a confined wavelet space by applying a threshold value to the scale factor (50 nm in our case) and the CWT coefficient of peaks with significant values in this space. And then, a derivative calculation of the wavelet coefficients surrounding each peak position at different scales yields an estimate of the peak width, enabling the peak to be eliminated exactly from the spectrum. Finally, polynomial fitting of the peak-excluded spectrum using least squares yields the spectral background, which is further corrected from the raw spectrum to produce the background-corrected spectrum, as depicted in Fig. 5–12.

The background-corrected spectra were next processed for feature selection using the SelectKBest (SKB) algorithm. The principle is to calculate the covariance between the intensity of a given channel in a spectrum and the KCl concentration of the corresponding sample, for the ensemble of the spectra in the training data set corresponding to different KCl offline analysis concentrations. The spectral channels of a spectrum are then ordered according

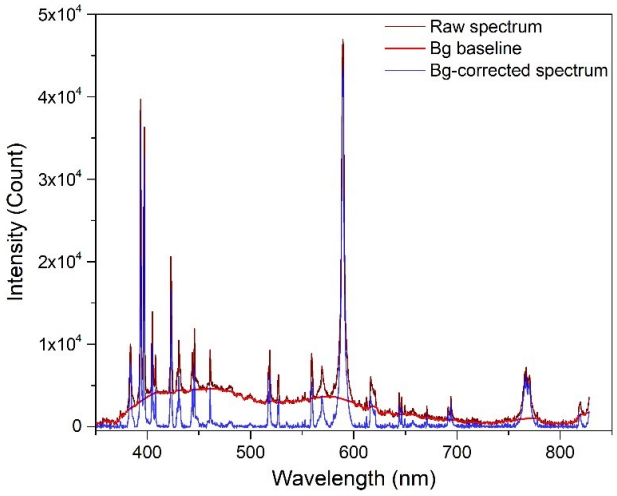


**Figure 5–12 Result of spectral background correction with a raw spectrum, the calculated spectral background and the background-corrected spectrum.**

to their correlation with the offline KCl concentration, from highest to lowest. To quantify this correlation, the Pearson correlation coefficient was adopted as the parameters expressing such connection. The Pearson's correlation coefficient between two variables in mathematics is calculated as the quotient of their covariance and the product of their respective standard deviations. The formula can be written as:

$$\rho_{X,Y} = \frac{\mathrm{cov}(X,Y)}{\sigma_X \sigma_Y} = \frac{\mathbb{E}[(X-\mu_X)(Y-\mu_Y)]}{\sigma_X \sigma_Y}, \tag{5–7}$$

where cov stands for the covariance, $\sigma_{X/Y}$ the standard deviation of $X/Y$, $\mathbb{E}$ the expectation and $\mu_{X/Y}$ the mean of $X/Y$.

Figure 5–13 illustrates the Pearson's correlation coefficients of the channels in a spectrum generated from the spectra in the training data set (Fig. 5–13 (b)) and a typical background-corrected spectrum (Fig. 5–13 (a)) for better visualization. A specific spectral channel can be positively or negatively correlated with the KCl concentration, as indicated by a positive or negative coefficient. A ranking based on the absolute value of Pearson's coefficient allowed 100 channels with the highest correlation or anti-correlation with the KCl concentrations of the training data set to be selected. The selected features are indicated by a red circle and vertical red line in Fig. 5–13 (b). Additionally, these characteristics are highlighted on the background-corrected spectrum in Fig. 5–13 (a). Although the features are selected based

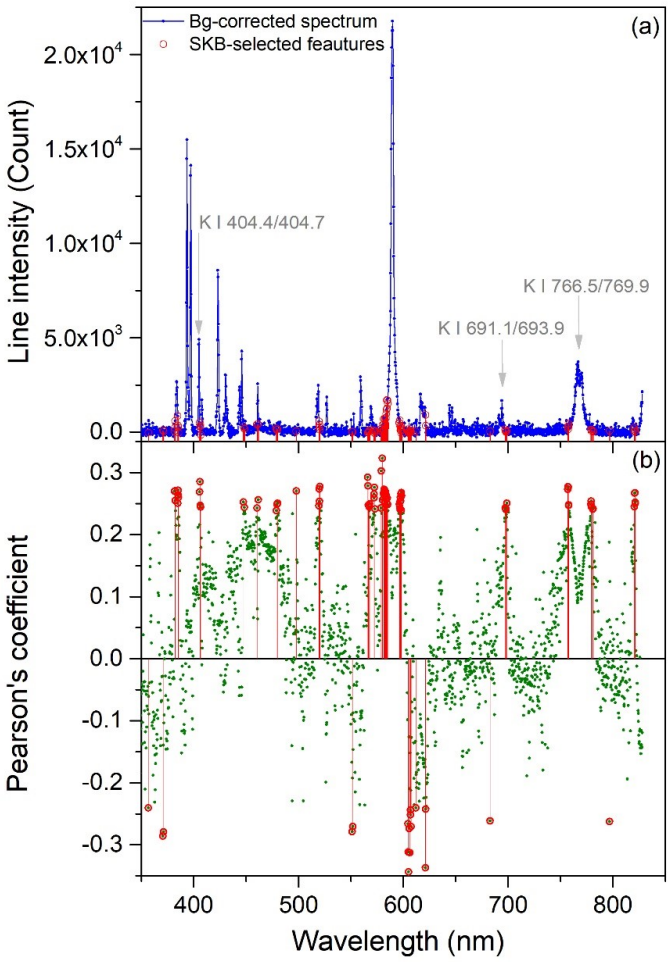


**Figure 5–13 Spectral feature selection using SKB algorithm: (a) A typical background-corrected spectrum (in blue dots), the intensities of the 100 selected features are highlighted with red circles; (b) Pearson correlation coefficients for each spectral channel calculated for the training data set (green dots), the 100 selected features are highlighted with red circles, which are the most correlated or anti-correlated with the offline KCl concentrations of the training data set.**

on their ranking with the Pearson coefficients, we can see that none of them have a considerably higher coefficient than the others. Hence, the correlation with the KCl content is very well spread across a vast range of characteristics. But a certain number of them can be ascribed a clear physical meaning, such as those connected with the three groups of K I lines depicted in Fig. 5–13 (a) that have a strong positive connection. Interestingly, we note that these characteristics correlate to the wings of the K I spectral lines, not the centers. The loss of correlation between these line centers and KCl concentration in the product is indicative of considerable self-absorption caused by the high concentration of KCl in the product. This phenomena is prominent around the group of K I 766.5/769.9 nm lines, where the Pearson coefficients exhibit a minimum at the center of these damaged lines, which are impacted by self-reversal.

### 5.6.4 Calibration model for KCl concentration

Each offline data set for KCl determination has ten average spectra associated, as was previously described. To create the model training data set, an ensemble of 100 groups of 10 average spectra and 100 offline KCl concentrations were chosen. The remaining 19 offline data's average spectra were used as the validation data set. An effort was made to evenly distribute the validation data in the 93% to 95.5% range, which contained the majority of the calibration data. The corresponding sample numbers of these groups in Table 5–1 are [6, 13, 26, 29, 37, 38, 41, 58, 66, 71, 74, 76, 78, 81, 83, 99, 102, 109, 114].

The 100 selected features of each average spectrum in the training data set were concatenated with the mean $H_2O$ concentration predicted by the above discussed $H_2O$ concentration model for the group of average spectra associated to the same offline $H_2O$ concentration, by the above discussed $H_2O$ concentration calibration model, to form a generalized spectrum of 101 channels. The ensemble of the generalized spectra was then employed as the input variables for a back propagation neural network (BPNN) with an input layer (101 neurons), a hidden layer (6 neurons), and an output layer (1 neuron for KCl concentration). The structure of the network is shown in Fig. 5–14. The training of the model is described in depth in reference [15], including a cross-validation approach to improve the model's performance. Using generalized spectra and the related KCl concentrations, the training process for the provided neural network topology produced a KCl concentration calibration model. The model was

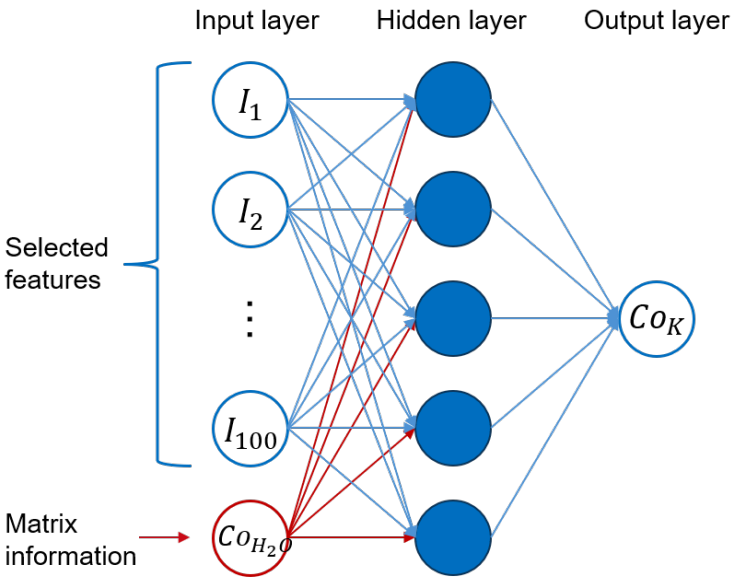


**Figure 5–14 Structure of the back-propagated neural network. It consists of three layers: an input layer, a hidden layer and an output layer. The feature of water concentration act as the additional matrix information in constructing the generalized spectrum for the training of the model.**

then evaluated using the validation data set, which consisted of the generalized spectra derived from spectral features selected based on the 100 channels determined by the training spectra, concatenated with the corresponding mean $H_2O$ concentration predicted by the water concentration calibration model.

The obtained results are shown in Fig. 5–15, where the calibration model with the projected concentrations for the training data set as a function of the offline data (in blue cross) and the linear regression are displayed (in blue straight line). We see a decent $R^2 = 0.9789$ and a slope of linear regression of 0.9599, which is quite close to the ideal value of 1. The validation points of model-predicted value versus offline data are also included (in orange circles) in the plot, demonstrating a strong connection with the calibration model. The error bars in the graph represent the standard deviation of the predicted values for ten average spectra. Further figures of merit were computed and shown in Table 5–3. The REC is 0.07412%, which is quite low. In terms of prediction performance, the REP and RSD values of 0.189% and 0.0433%, respectively, are both quite satisfactory.

In addition, we further compared the model-predicted KCl concentrations for the training and validation data sets, as well as the offline analysis data. This allowed us to calculate

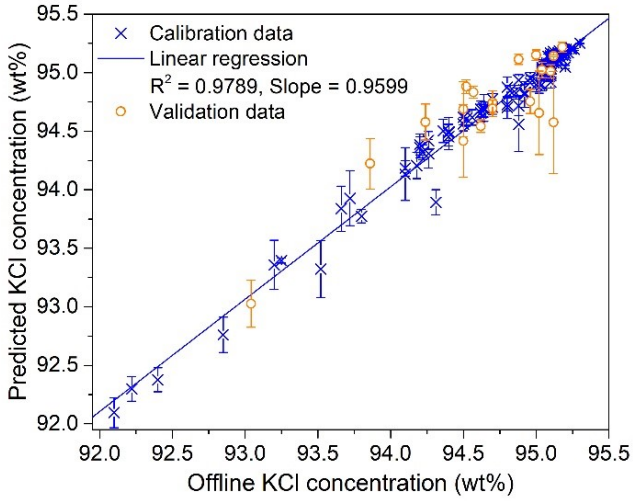


**Figure 5–15 Performance of the multivariate calibration model of $H_2O$ based on CNN. The calibration data for model training is shown in blue cross together with the linear regression in blue straight line. The validation data is shown in orange circle. The error bars in the figure represent of the model predicted concentrations among the 10 average spectra.**

**Table 5–3 Parameters assessing the performances of the multivariate calibration model for KCl**

| Calibration model | | Prediction performance | |
|---|---|---|---|
| $R^2$ | REC(%) | REP(%) | RSD(%) |
| 0.9789 | 0.07412 | 0.189 | 0.438 |

the bias of the prediction, which may be compared to the Chinese national standard's requirement (GB6549-2011)[4]. The results are displayed in Fig. 5–16, where it can be seen that all forecasted KCl concentrations fulfill the national standard, attesting to the model's performance.

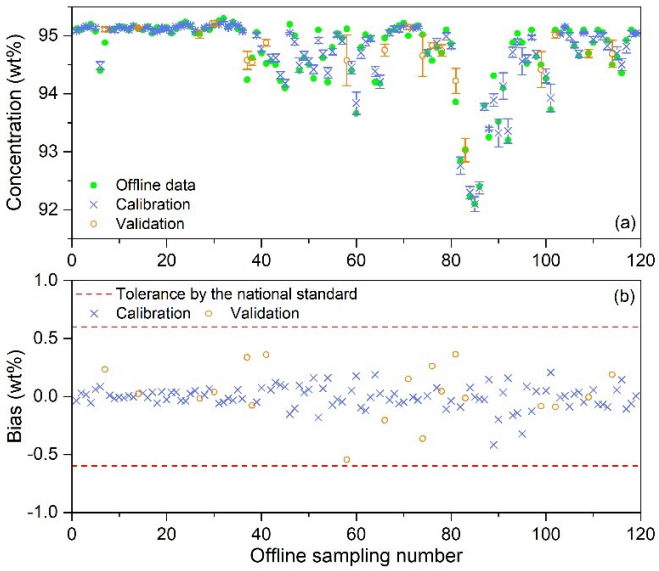


**Figure 5–16 (a) Comparison between the model-predicted KCl concentration and the offline analysis data; (b) presentation of the prediction bias (difference between the model-predicted value and the offline analysis value) and comparison with the requirement of the national standard, absolute bias ≦ 0.598% for KCl.**

## 5.7 Conclusion

In this work, online in situ and simultaneous assessments of the concentrations of $H_2O$ and KCl in potash at the last stage of manufacture for product quality evaluation were demonstrated. The obtained absolute measurement biases for both substances fall within the limits specified by the Chinese national standard, namely less than 0.2% for $H_2O$ and less than 0.598% for KCl. This demonstration has established a solid foundation for the implementation of LIBS in the potash extraction sector for a variety of control and evaluation purposes at various production stages.

In addition to the experimental issue of the project, which has been resolved with the development of a dedicated LIBS instrument capable of continuous and automatic operation

in the real industrial environment with temperature variations, dusts, and vibrations, there are several other issues that have been addressed. The LIBS data treatment method and accompanying algorithms have been developed as the project's essential and crucial component. Indeed, the interaction of a powder and water mixture with a focused, high-intensity laser pulse results in the formation of a complex material. In addition to the inability to characterize the interaction mechanism with a simple physical model, the influence of water on the LIBS spectrum of potash powder appears to be highly complex, affecting the spectrum in its whole - spectral lines and background.

Our approach, therefore, consisted in considering the influence of water as a matrix effect in the determination of KCl in potash. The ensuing working flowchart directed us to first determine the $H_2O$ concentration of a product and then, with the knowledge of the $H_2O$ concentration, process the spectrum for KCl concentration determination. Specifically, in the implementation of the algorithm shown in the working flowchart, the average spectra were converted into spectrum-images using continuous wavelet transform (CWT) following a pretreatment in order to highlight the influence of water on the completeness of a LIBS spectrum. Within a calibration model, CNN, an efficient image processing method, was employed to map spectrum-images to offline analysis water concentrations. To generate background-corrected average spectra for KCl determination, an approach combining CWT, derivative calculation, and least squares fitting was first employed. A feature selection based on the SKB method produced 100 spectral features that were predominantly correlated or anti-correlated with the offline analysis KCl concentrations. By concatenating the selected characteristics and the model-predicted concentration, generalized spectra were generated and fed to a BPNN. The ultimate result was a KCl calibration model. Overall, both models had an $R^2$ greater than 0.97, a REP of 31 wt% for $H_2O$ and 0.189 wt% for KCl, and acceptable absolute biases for the determination of both chemicals in potash relative to the national standard, as stated at the beginning of the conclusion, which was the purpose of the research.

## Bibliography

[1] PRAJAPATI K. The importance of potassium in plant growth - A review[J]. Indian Journal of Plant Sciences, 2012, 1: 177-186.

[2] HE P, YANG L, XU X, et al. Temporal and spatial variation of soil available potassium in China (1990–2012)[J/OL]. Field Crops Research, 2015, 173: 49-56. https://www.sciencedirect.com/science/article/pii/S0378429015000064. DOI: https://doi.org/10.1016/j.fcr.2015.01.003.

[3] U.S. Geological Survey. Mineral commodity summaries 2023[R/OL]. Report. Reston, VA, 2023: 210. https://doi.org/10.3133/mcs2023. DOI: 10.3133/mcs2023.

[4] The State Bureau of Quality and Technical Supervision. GB/T 6549-2011 Potassium chloride[S]. Beijing: Standard Press of China, 2011.

[5] The State Bureau of Quality and Technical Supervision. GB/T 37918-2019 Fertilizer grade potassium chloride[S]. Beijing: Standard Press of China, 2019.

[6] ENGELBRECHT R M, MCCOY F A. Determination of Potassium by Tetraphenylborate Method[J]. Analytical Chemistry, 1956, 28: 1772-1773.

[7] NIELSEN S S. Sodium and Potassium Determinations by Atomic Absorption Spectroscopy and Inductively Coupled Plasma-Optical Emission Spectroscopy[M/OL]// Food Analysis Laboratory Manual. Cham: Springer International Publishing, 2017: 171-177. https://doi.org/10.1007/978-3-319-44127-6_20. DOI: 10.1007/978-3-319-44127-6_20.

[8] ARNQUIST I J, HOPPE E W. The quick and ultrasensitive determination of K in NaI using inductively coupled plasma mass spectrometry[J/OL]. Nuclear Instruments and Methods in Physics Research Section A: Accelerators, Spectrometers, Detectors and Associated Equipment, 2017, 851: 15-19. https://www.sciencedirect.com/science/article/pii/S0168900217301547. DOI: https://doi.org/10.1016/j.nima.2017.01.064.

[9] GAFT M, NAGLI L, ELIEZER N, et al. Elemental analysis of halogens using molecular emission by laser-induced breakdown spectroscopy in air[J/OL]. Spectrochimica Acta Part B: Atomic Spectroscopy, 2014, 98: 39-47. https://www.sciencedirect.com/science/article/pii/S0584854714000883. DOI: https://doi.org/10.1016/j.sab.2014.05.011.

[10] QING S, XINLEI Z, YAN Z, et al. Development of an online X-ray fluorescence analysis system for heavy metals measurement in cement raw meal[J/OL]. Spectroscopy Letters, 2016, 49(3): 188-193. eprint: https://doi.org/10.1080/00387010.2015.11181

27. https://doi.org/10.1080/00387010.2015.1118127. DOI: 10.1080/00387010.2015.1118127.

[11] NOLL R. Laser-Induced Breakdown Spectroscopy: Fundamentals and Applications[M]. Heidelberg: Springer Berlin, 2012.

[12] NOLL R, FRICKE-BEGEMANN C, CONNEMANN S, et al. LIBS analyses for industrial applications –an overview of developments from 2014 to 2018[J/OL]. J. Anal. At. Spectrom., 2018, 33: 945-956. http://dx.doi.org/10.1039/C8JA00076J. DOI: 10.1039/C8JA00076J.

[13] DING Y, ZHANG W, ZHAO X, et al. A hybrid random forest method fusing wavelet transform and variable importance for the quantitative analysis of K in potassic salt ore using laser-induced breakdown spectroscopy[J/OL]. J. Anal. At. Spectrom., 2020, 35: 1131-1138. http://dx.doi.org/10.1039/D0JA00010H. DOI: 10.1039/D0JA00010H.

[14] BOUCHER T F, OZANNE M V, CARMOSINO M L, et al. A study of machine learning regression methods for major elemental analysis of rocks using laser-induced breakdown spectroscopy[J/OL]. Spectrochimica Acta Part B: Atomic Spectroscopy, 2015, 107: 1-10. https://www.sciencedirect.com/science/article/pii/S0584854715000518. DOI: https://doi.org/10.1016/j.sab.2015.02.003.

[15] SUN C, TIAN Y, GAO L, et al. Machine Learning Allows Calibration Models to Predict Trace Element Concentration in Soils with Generalized LIBS Spectra[J/OL]. Scientific Reports, 2019, 9(1): 11363. https://doi.org/10.1038/s41598-019-47751-y. DOI: 10.1038/s41598-019-47751-y.

[16] ZHANG Y, SUN C, GAO L, et al. Determination of minor metal elements in steel using laser-induced breakdown spectroscopy combined with machine learning algorithms[J/OL]. Spectrochimica Acta Part B: Atomic Spectroscopy, 2020, 166: 105802. https://www.sciencedirect.com/science/article/pii/S0584854719306068. DOI: https://doi.org/10.1016/j.sab.2020.105802.

[17] YUE Z, SUN C, GAO L, et al. Machine learning efficiently corrects LIBS spectrum variation due to change of laser fluence[J/OL]. Opt. Express, 2020, 28(10): 14345-14356. https://opg.optica.org/oe/abstract.cfm?URI=oe-28-10-14345. DOI: 10.1364/OE.392176.

[18] XU W, SUN C, TAN Y, et al. Total alkali silica classification of rocks with LIBS: influences of the chemical and physical matrix effects[J/OL]. J. Anal. At. Spectrom., 2020, 35: 1641-1653. http://dx.doi.org/10.1039/D0JA00157K. DOI: 10.1039/D0JA00157K.

[19] ZHANG Y, SUN C, YUE Z, et al. Correlation-based carbon determination in steel without explicitly involving carbon-related emission lines in a LIBS spectrum[J/OL]. Opt. Express, 2020, 28(21): 32019-32032. https://opg.optica.org/oe/abstract.cfm?URI=oe-28-21-32019. DOI: 10.1364/OE.404722.

[20] LU C, WANG B, JIANG X, et al. Detection of K in soil using time-resolved laser-induced breakdown spectroscopy based on convolutional neural networks[J/OL]. Plasma Science and Technology, 2018, 21(3): 034014. https://dx.doi.org/10.1088/2058-6272/aaef6e. DOI: 10.1088/2058-6272/aaef6e.

[21] CHEN J, PISONERO J, CHEN S, et al. Convolutional neural network as a novel classification approach for laser-induced breakdown spectroscopy applications in lithological recognition[J/OL]. Spectrochimica Acta Part B: Atomic Spectroscopy, 2020, 166: 105801. https://www.sciencedirect.com/science/article/pii/S0584854719306317. DOI: https://doi.org/10.1016/j.sab.2020.105801.

[22] HUSSEIN A E, DIWAKAR P K, HARILAL S S, et al. The role of laser wavelength on plasma generation and expansion of ablation plumes in air[J/OL]. Journal of Applied Physics, 2013, 113(14): 143305. eprint: https://doi.org/10.1063/1.4800925. https://doi.org/10.1063/1.4800925. DOI: 10.1063/1.4800925.

[23] ALEXANDER KRAMIDA J R, Yuri Ralchenko, NIST ASD Team. NIST Atomic Spectra Database (version 5.10)[S/OL]. Gaithersburg: National Institute of Standards, 2022. https://doi.org/10.18434/T4W30F. DOI: 10.18434/T4W30F.

[24] ZHANG Z M, CHEN S, LIANG Y Z, et al. An intelligent background-correction algorithm for highly fluorescent samples in Raman spectroscopy[J/OL]. Journal of Raman Spectroscopy, 2010, 41(6): 659-669. eprint: https://analyticalsciencejournals.onlinelibrary.wiley.com/doi/pdf/10.1002/jrs.2500. https://analyticalsciencejournals.onlinelibrary.wiley.com/doi/abs/10.1002/jrs.2500. DOI: https://doi.org/10.1002/jrs.2500.

[25] KRIZHEVSKY A, SUTSKEVER I, HINTON G E. ImageNet Classification with Deep Convolutional Neural Networks[J/OL]. Commun. ACM, 2017, 60(6): 84-90. https://doi.org/10.1145/3065386. DOI: 10.1145/3065386.

[26] MARK H, WORKMAN J. Chemometrics in Spectroscopy (Second Edition)[M]. Academic Press, 2018.

[27] GAN F, RUAN G, MO J. Baseline correction by improved iterative polynomial fitting with automatic threshold[J/OL]. Chemometrics and Intelligent Laboratory Systems, 2006, 82(1): 59-65. https://www.sciencedirect.com/science/article/pii/S0169743905001589. DOI: https://doi.org/10.1016/j.chemolab.2005.08.009.

[28] SCHULZE H G, FOIST R B, OKUDA K, et al. A Small-Window Moving Average-Based Fully Automated Baseline Estimation Method for Raman Spectra[J/OL]. Applied Spectroscopy, 2012, 66(7): 757-764. eprint: https://doi.org/10.1366/11-06550. https://doi.org/10.1366/11-06550. DOI: 10.1366/11-06550.

[29] CARLOS COBAS J, BERNSTEIN M A, MARTÍN-PASTOR M, et al. A new general-purpose fully automatic baseline-correction procedure for 1D and 2D NMR data[J/OL]. Journal of Magnetic Resonance, 2006, 183(1): 145-151. https://www.sciencedirect.com/science/article/pii/S1090780706002266. DOI: https://doi.org/10.1016/j.jmr.2006.07.013.

# Chapter 6 Conclusions and perspectives

In this thesis, we investigated the simultaneous control of filament position and length, the dynamics of nonlinear propagation of intense finite energy ring-Airy beams at the kilometer scale, and the application of quantitative elemental analysis based on laser induced breakdown spectroscopy assisted by the state-of-the-art machine learning techniques. In particular, we implemented a series of numerical codes solving the extended nonlinear Schrödinger equation to simulate and diagnose the nonlinear propagation of electric fields in air, and built neural networks to quantitatively and statistically model spectral data and KCl and moisture content in potash fertilizer.

Firstly, we considered the remote control of the properties of the filament. Unavoidable losses occur as an ultrashort and intense laser pulse propagates in air because of self-focusing and subsequent multiphoton absorptions, preventing long distance projection of filaments required in many applications of ultrashort and intense pulses in the atmosphere. Suitable engineering of the initial wavefront constitutes a way to distribute these losses within a filament at a predefined location. In this work we implement inverse design associated with an intermediate state in numerical simulation of the propagation of an ultrashort and intense laser pulse in order to find out the initial wavefront for the required remote filament generation. More specifically, starting from the intermediate state of a Bessel-Gauss beam, the pulse propagates forward evolving into a uniform filament together with a plasma channel. It then reversely propagates into a divergent conical beam with a decreasing intensity. Numerical blowups in the reverse propagation of an ionizing pulse are therefore avoided. The results show an initial pulse in the form of a torus beam profile with a linear radial phase shift, characterized by the radii of the major and minor rings, $w_R$ and $w_r$. The forward propagation of the torus pulse generates thus at a distance $d$, a filament of length $L$ that can be related to $w_R$, $w_r$ and $d$ by an empirical relation. The scalability of the conical beam solution allows for the ability of projecting a uniform and long filament into a remote distance without theoretical limitation. In a practical point of view, a filament can be generated up to one kilometer with a tabletop optical pulse shaper.

Our results constitute a major step to a full control of remote generation of long plasma channels in the atmosphere with femtosecond laser pulses. They open the way to the devel-

opment of important applications of ultrashort laser pulses in the atmosphere, such as remote sensing, generation of virtual antennas for stealthy communications or lightning protection with a laser conducting rod, which were hampered so far by the difficulty to generate long and uniform plasma channels remotely in the atmosphere. The combination of reverse engineering and inverse design introduced in this work provides an elegant solution to this issue, which can be further easily transposed for remote projections of different sources of radiation in air.

Secondly, in order to initiate filamentation at distance of hundreds or even kilometer scales in the atmosphere, previous works were based on terawatt peak power laser systems and allowed investigations on the limitations due to diffraction and the effects of air turbulence to be conducted. However, our study on the nonlinear propagation dynamics of gigawatt finite-energy ring-Airy beams opens up a possibility to generate filaments remotely using gigawatt laser powers. The unique advantages of ring-Airy beams - self-reconstruction and parabolic trajectory of the peak intensity - are utilised. Thus, the robustness of the wavefront of the beam is guaranteed when it encounters small object during propagation. The rings of the beam will shrink, converge and autofocus abruptly along propagation. This means that we can send beams with relatively low initial intensity, which then propagate linearly or quasi-linearly before autofocusing, amplifying hundreds or even thousands of times after focusing. Furthermore, when the beam converges in the center, the induced nonlinear effects due to increasing intensity such as the Kerr effect will further accelerate the converging process. The influence of the ring-Airy beam parameters on the position of the nonlinear focus is investigated showing that the nonlinear focus would shift backward as the power increases. The magnitude of this shift depends on both the input power and the specific apodization form of the ring-Airy beam. Once the intensity of the beam exceeds ionization threshold of air, the filament will be generated and observed. The power contained in the region surrounding the filament is found to be the same order of magnitude as the critical power for self-focusing 3.3 GW, and it is almost independent of the input parameters.

Finally, we demonstrated online *in situ* characterization of potash fertilizer, a powder material, at its final production stage in factory on the production conveyer belt for quality assessment, with a specifically developed laser-induced breakdown spectroscopy (LIBS) instrument and a dedicated data treatment software based on machine learning. Besides

the usual difficulties encountered in online LIBS analysis, the specific challenge resides in moisture variation in the product, which results in a complex sample of powder of particle size 100 µm mixed with water ($H_2O$). Influence on LIBS spectrum was clearly observed, while no detailed physical model is available to describe such influence. In addition, the emission line intensity from hydrogen (H $\alpha$ line) observed in spectrum did not show clear relation to the $H_2O$ concentration. The approach of analysis by correlation of the whole spectrum to the concentration was used to first determine the $H_2O$ concentration, which was further used as an additional parameter to concatenate with a LIBS spectrum in the formation of generalized spectrum. The last was used as input vector to train KCl concentration calibration model. More specifically, LIBS spectra were first transformed into 2-D images with continuous wavelet transform (CWT). Convolutional neural network (CNN) then allowed mapping spectrum-images to the $H_2O$ concentrations of the corresponding samples. While a back-propagation neural network (BPNN) mapped generalized spectra to the KCl concentrations of the samples. The tests with online LIBS spectra and the corresponding offline analysis data of 119 samples taken during the period of LIBS measurements demonstrate advanced analytical performances of the trained models for $H_2O$ and KCl. Comparison between the model-predicted concentrations and the data from the offline analysis shows determination bias which fulfil the requirements of the concerned national standards (bias $\leqq$ 0.20% for $H_2O$ and $\leqq$ 0.598% for KCl) for the quasi totality of the tested samples.

At the end of this thesis, we would like to briefly introduce several potential projects that could be followed up based on the research work in this thesis. Considering that the two works related to the filament at the beginning were completely based on numerical simulations, the most straightforward option for the next step of the research is to enter the laboratory and select the appropriate experimental equipment to carry out experiments to verify our calculations and ideas. As we have simplified the model in our calculations and have not taken into account the effect of atmospheric turbulence on the propagation of intense laser pulses, it is also necessary to investigate it numerically as well as experimentally, which is essential when the beam propagation distance is in the order of hundreds of meters or even kilometers. When the pulse width is short, the dispersion of the pulse during propagation also needs to be taken into account, which allows us to study the complex dynamics involved in the propagation of non-linear pulses and the precise control of the subsequent filament. We

can also combine the concept of reverse engineering with the ring Airy beam and use it as an intermediate state for indirect control of intense laser far-field delivery. As shown in Fig. 6–1, the peak intensity of the ring Airy beam will follow a parabolic trajectory along propagation, a Bottle beam will be formed between the output and the intermediate state and the final target position. The advantage of this is that the size of the modulation equipment required for laser

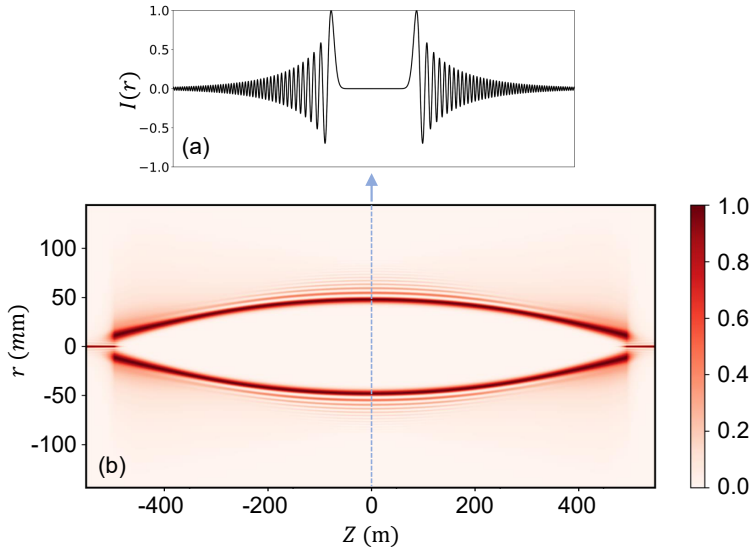


**Figure 6–1 Demonstration of the ring-Airy beam as an intermediate state. (a) Light intensity distribution of a ring-Airy beam in cylindrical coordinate. (b) Evolution of the intensity profile along forward & backward propagation of a ring-Airy beam, its characteristic bending nature leads to the formation of a Bottle shape. Simulation parameters:** $w_0 = 3$ **mm,** $r_0 = 45$ **mm.**

beam exit is significantly reduced compared to the Bessel-Gauss intermediate state. It would be also worthwhile to investigate how to avoid the purely numerical divergence that arises in certain situations close to the clamping intensity, when non-linear losses are converted into gain during propagating in the reverse direction. Discretization results in unavoidable small numerical errors in solving non-linear partial differential equations. Propagation in the inverse direction can cause results to flow from one locally stable manifold, reaching the clamping intensity from below to another reaching the clamping intensity from above. If this occurs, the simulation ends up in a divergence in reverse propagation. We need to identify when this situation is likely to arise and, by means of a local stability analysis, find a solution to maintain the solution on its stable manifold, so that the solution space corresponding to forward and inverse propagation is the same.

# Appendix A Wavelet transform

Apart from the Fourier transform technique described above, there is another spectrum analysis tool called $wavelettransform$. It decomposes a signal $s(t)$ into a 2D space $(a, b)$ with wavelet matrix coefficient $\mathbb{C}(a, b)$ as follows:

$$\mathbb{C}(a,b) = \int_{-\infty}^{+\infty} s(t)\,\psi_{a,b}(t)\,dt, \tag{A–1}$$

where $\psi_{a,b}(t)$ is the mother wavelet with scale $a$ and shifting $b$. When the signal $s(t)$ contains sudden jumps or singularities, the wavelet transform is more advantageous than the Fourier transform. If the chosen form of the mother wavelet $\psi_{a,b}(t)$ matches with signal $s(t)$, this is when $\mathbb{C}(a, b)$ reaches its maximum. Thus, the coefficient characterizes the weights of the signal decomposed onto the 2D space $(a, b)$.

We selected the Mexican Hat wavelet as our mother wavelet:

$$\psi(t) = \left(\frac{2}{\sqrt{3}}\pi^{-\frac{1}{4}}\right)\left(1-t^2\right)\exp(-t^2/2), \tag{A–2}$$

with scaled and shifting $\psi_{a,b}(t) \equiv \frac{1}{\sqrt{a}}\psi\left(\frac{t-b}{a}\right)$, $a$ in $R^+$, $b$ in $R$.

The details about how to use wavelet transform to find the peak, denoise and remove the continuous background are refer to the work of Zhi-Min Zhang *et al.*[1].The originial code package is written in R (https://code.google.com/archive/p/baselinewavelet/,or https://github.com/zmzhang/baselineWavelet).

A example showing the wavelet transform process of a Raman spectrum is as follows:

```
data(raman)
x=m[7,]
scales <-seq(1, 70, 1)
wCoefs <- cwt(x, scales=scales, wavelet='mexh')
png("WaveletCoeffs.png",width=1000,height=600)
image(1:nrow(wCoefs), scales, wCoefs,
col=terrain.colors(256), axes=FALSE, xlab='index',
ylab='CWT coefficient scale', main='CWT coefficients')
box()
dev.off()
localMax <- getLocalMaximumCWT(wCoefs)
ridgeList <- getRidge(localMax, gapTh=3, skip=2)
png("RidgeList.png",width=1000,height=600)
plotRidgeList(ridgeList)
```

```
dev.off()
majorPeakInfo = identifyMajorPeaks(x, ridgeList, wCoefs, SNR.Th=1,ridgeLength=5)
peakWidth=widthEstimationCWT(x,majorPeakInfo)
backgr = baselineCorrectionCWT(x,peakWidth,lambda=1000,differences=1)
corrected=x-backgr
png("Signal_Bg.png",width=1000,height=600)
plot(xa,x,type='l',ylim=c(min(c(x,corrected)),
max(c(x,corrected))),main="The background-correction result of Raman Spectra",
xlab=expression("Wavenumber / cm"^-1),ylab="Raman Intensity/Arbitr. Units")
points(xa[majorPeakInfo$peakIndex],x[majorPeakInfo$peakIndex])
lines(xa,backgr,lty=5)
lines(xa,corrected)
dev.off()
```

Below we have implemented this code in Python environment via rpy2 (https://github.com/lzou13/baselineWavelet_python).

```
import rpy2.robjects as ro
from rpy2.robjects.packages import importr
from numpy import *
# import R's "baselineWavelet" package
bW= importr('baselineWavelet')
def baselineWavelet(Spectrum_data):
    S=Spectrum_data
    # Transform the original data into R language format
    rFS=ro.FloatVector(S)
    # Creating a R array correspond to the data's dimension
    sS=ro.FloatVector(range(1,shape(S)[0]+1))
    # Start the wavelet analysis from R's baselineWavelet package
    scales=ro.r.seq(1,127,1)
    cwtargs={'scales':scales,'wavelet':'mexh'}
    # Wavelet coeffecients calculated by cwt
    wCoefs=ro.r.cwt(rFS,**cwtargs)
    # Get the ridge of wavelet coeffecients and output it into png file.
    localMax=bW.getLocalMaximumCWT(wCoefs)
    #******************
    ridgeList=bW.getRidge(localMax, gapTh=3, skip=2)
    # Calculating the background contribution
    MPargs={'SNR.Th':1,'ridgeLength':10}
    # Peak infomation
    majorPeakInfo = bW.identifyMajorPeaks(rFS, ridgeList, wCoefs,scales,**MPargs)
    peakWidth=bW.widthEstimationCWT(rFS,majorPeakInfo)
    bCargs={'lambda':1000,'differences':1}
    #******************
    backgr = bW.baselineCorrectionCWT(rFS,peakWidth,**bCargs)
    corrected=ro.FloatVector(array(rFS)-array(backgr))
    #******************
    #wavelet coeffecients, baseline, baseline-corrected spectrum
    return array(wCoefs),array(backgr),array(corrected)
```

# List of Research Achievements

## Publications

[1] **Long Zou**, Chen Sun, Yunfei Rao, Tianyang Sun, Jin Yu and Arnaud Couairon. Reverse wavefront engineering for remote generation of a near-infrared femtosecond Bessel beam filament in air[J], Phys. Rev. Research 2022, 4:043025

[2] **Long Zou**, Chen Sun, Mengting Wu, Yuqing Zhang, Zengqi Yue, Weijie Xu, Sahar Shabbir, Fengye Chen, Bin Liu, Wenhui Liu and Jin Yu. Online simultaneous determination of $H_2O$ and KCl in potash with LIBS coupled to convolutional and back-propagation neural networks[J], J. Anal. At. Spectrom., 2021, 36:303-313

[3] **Long Zou**, Chen Sun, Jin Yu and Arnaud Couairon. Laser energy deposition with ring-Airy beams beyond kilometer range in the atmosphere, Submitted to Phys. Rev. A

[4] Mengting Wu, Weijie Xu, **Long Zou**, Yuqing Zhang, Zengqi Yue, Sahar Shabbir, Fengye Chen, Bin Liu, Wenhui Liu, Jin Yu  Chen Sun. Precise determination of potassium in potash with self-absorption correction in laser-induced breakdown spectroscopy[J]. Appl. Phys. B, 2020, 128:102

[5] Tao Zeng, Anthony Hegg, **Long Zou**, Shengtao Jiang, Wei Ku. Transport in the emergent Bose liquid: Bad metal, strange metal, and weak insulator, all in one system[J]. Preprint, arXiv: 2112.05747

[6] Shengtao Jiang, **Long Zou**, and Wei Ku. Non-Fermi-liquid scattering against an emergent Bose liquid: Manifestations in the kink and other exotic quasiparticle behavior in the normal-state cuprate superconductors[J]. Phys. Rev. B, 2019, 99:104507

[7] Sahar Shabbir, Weijie Xu, Yuqing Zhang, Chen Sun, Zengqi Yue, **Long Zou**, Fengye Chen, Jin Yu. Machine learning and transfer learning for correction of the chemical and physical matrix effects in the determination of alkali and alkaline earth metals with LIBS in rocks[J]. Spectrochim. Acta B At. Spectrosc, 2022, 194:106478

[8] Weijie Xu, Chen Sun, Yuqing Zhang, Zengqi Yue, Sahar Shabbir, **Long Zou**, Fengye Chen, Li Wang and Jin Yu. Accurate determination of structural $H_2O$ in rocks using LIBS coupled with machine learning algorithms extensively exploring the characteristics of the H $\alpha$ line[J]. J. Anal. At. Spectrom., 2022, 37:317-329

[9] Chen Sun, Weijie Xu, Yongqi Tan, Yuqing Zhang, Zengqi Yue, **Long Zou**, Sahar Shab-

bir, Mengting Wu, Fengye Chen & Jin Yu. From machine learning to transfer learning in laser-induced breakdown spectroscopy analysis of rocks for Mars exploration[J]. Sci. Rep., 2021, 11:21379

[10] Fengye Chen, Chen Sun, Zengqi Yue, Yuqing Zhang, Weijie Xu, Sahar Shabbir, **Long Zou**, Weiguo Lu, Wei Wang, Zhenwei Xie, Lanyun Zhou, Yan Lu, Jin Yu. Screening ovarian cancers with Raman spectroscopy of blood plasma coupled with machine learning data processing[J]. Spectrochim. Acta A Mol. Biomol. Spectrosc., 2022, 265:120355

[11] Zengqi Yue, Chen Sun, Fengye Chen, Yuqing Zhang, Weijie Xu, Sahar Shabbir, **Long Zou**, Weiguo Lu, Wei Wang, Zhenwei Xie, Lanyun Zhou, Yan Lu, and Jin Yu, Machine learning-based LIBS spectrum analysis of human blood plasma allows ovarian cancer diagnosis[J]. Biomed. Opt. Express, 2021, 12:2559-2574

[12] Sahar Shabbir, Yuqing Zhang, Chen Sun, Zengqi Yue, Weijie Xu, **Long Zou**, Fengye Chen, Jin Yu. Transfer learning improves the prediction performance of a LIBS model for metals with an irregular surface by effectively correcting the physical matrix effect[J]. J. Anal. At. Spectrom., 2021, 36(7):1441-1454

[13] Yuqing Zhang, Chen Sun, Zengqi Yue, Sahar Shabbir, Weijie Xu, Mengting Wu, **Long Zou**, Yongqi Tan, Fengye Chen, and Jin Yu, Correlation-based carbon determination in steel without explicitly involving carbon-related emission lines in a LIBS spectrum[J]. Opt. Express, 2020, 28:32019-32032

[14] Weijie Xu, Chen Sun, Yongqi Tan, Liang Gao, Yuqing Zhang, Zengqi Yue, Sahar Shabbir, Mengting Wu, **Long Zou**, F. Chen, S. Liu and Jin Yu. Total alkali silica classification of rocks with LIBS: influences of the chemical and physical matrix effects[J]. J. Anal. At. Spectrom., 2020, 35:1641-1653

[15] Zengqi Yue, Chen Sun, Liang Gao, Yuqing Zhang, Sahar Shabbir, Weijie Xu, Mengting Wu, **Long Zou**, Yongqi Tan, Fengye Chen, and Jin Yu. Machine learning efficiently corrects LIBS spectrum variation due to change of laser fluence[J]. Opt. Express 2020, 28:14345-14356

## Conferences

1. Application of LIBS spectral data processing based on machine learning algorithm in potash Fertilizer online analysis, The 9th Chinese Symposium on Laser-Induced Breakdown Spectroscopy (Poster, Dunhuang, China, 05/2023)
2. Inverse design and control of remotely generated uniform plasma channels in air, SPIE Photonics Europe, Nonlinear Optics and its Applications (Oral presentation, Strasbourg, France, 4/2022)
3. Online simultaneous determination of H2O and KCl in potash with LIBS coupled to convolutional and back-propagation neural networks, 11th International Conference on Laser-Induced Breakdown Spectroscopy (Oral presentation, Online, 09/2020)
4. Application of LIBS spectral data processing based on machine learning algorithm in potash Fertilizer online analysis, The 8th Chinese Symposium on Laser-Induced Breakdown Spectroscopy (Oral presentation, Online, 08/2020)
5. Normal-state optical conductivity and linear resistivity of the cuprates from tightly bound pre-formed pairs, APS March Meeting (Oral presentation, Boston, Massachusetts, USA, 03/2019)
6. Normal-State Optical Conductivity of the Cuprates from Tightly Bound Pre-Formed Pairs, APS March Meeting (Oral presentation, Los Angeles, California, USA, 03/2018)
7. A 2nd kind of Superconducting Gap and its Novel Phenomena in Cuprates, The 7th Workshop on Quantum Many-Body Computation (Poster, UCAS, Beijing, China, 05/2017)

ECOLE DOCTORALE

**Titre:** Simulation du dépôt d'énergie laser dans l'air avec des champs lumineux structurés et traitement de données d'apprentissage automatique pour une analyse quantitative des cibles à distance

**Mots clés:** Méthodes de conception inverses, Simulation numérique, Filamentation d'impulsion laser, LIBS, l'algorithme d'apprentisage automatique et l'effet de matrice

**Résumé:** La propagation d'impulsions laser ultra-courtes et ultra-intenses dans l'atmosphère est de plus en plus étudiée. Un contrôle précis de la focalisation du champ laser et de la distribution des filaments de lumière qui s'étendent au-delà du foyer est nécessaire pour de nombreuses applications, comme la mission d'exploration de Mars qui comprend l'analyse des éléments chimiques à l'aide de la spectroscopie de désintégration induite par laser (LIBS), l'analyse de la composition de l'atmosphère par des techniques de détection et de télémétrie lumineuses (LIDAR), le déclenchement et le guidage de décharges électriques entre les nuages, ou la génération de lasers à lumière blanche par filamentation laser. Un contrôle quantitatif des propriétés de l'impulsion laser est très difficile en raison de l'interaction non-linéaire complexe entre l'impulsion laser intense et le milieu. Actuellement, les méthodes couramment utilisées reposent sur le contrôle des paramètres initiaux de l'impulsion laser en fonction du champ laser observé sur la cible. La grande dimension de l'espace des paramètres et la sensibilité des résultats aux conditions initiales rendent l'ajustement du champ laser hors du laboratoire difficile et inefficace pour répondre aux exigences des applications pratiques.
Dans ce contexte, cette thèse propose une réponse à quelques-uns des défis de la propagation d'impulsions laser femtoseconde à longue portée, basée sur des scénarios de modulation de l'impulsion laser qui garantissent d'atteindre un champ laser sur cible avec les propriétés souhaitées. Ces scénarios ont été obtenus en associant méthodes d'ingénierie inverse et simulations numériques. Nous montrons que différents champs cibles peuvent être facilement et efficacement atteints en modulant le champ en sortie du laser. Chaque fois que cela est possible, la modulation est obtenue par simulation de la propagation inverse du champ cible vers le laser.

**Title:** Simulation of laser energy deposition with structured light beams in air and machine learning data treatment for LIBS analysis of remote targets

**Keywords:** nonlinear propagation, filamentation of structured light pulses, numerical simulation and reverse engineering, laser-induced breakdown spectroscopy, machine learning and matrix effect

**Abstract:** The propagation of ultrashort and ultra-intense laser pulses in the atmosphere is increasingly studied. Precise control of the focusing of the laser field and the distribution of light filaments extending beyond the focus is required for many applications, such as the Mars exploration mission on the analysis of chemical elements using Laser Induced Breakdown Spectroscopy (LIBS), the analysis of the composition of air by Light Detection and Ranging (LIDAR) techniques, the triggering and guiding of electric discharges between clouds, or the generation of white light laser by filamentation. A quantitative control of the light pulse properties is very difficult due to the complex nonlinear interaction between the intense laser pulse and the medium. At present, commonly used methods rely on the parameter control of the initial laser output and the feedback of the field at the target position. The high-dimension of the parameter space and the high sensitivity of the results to the initial conditions make the adjustment of the laser field outside the laboratory difficult and inefficient to meet the requirements of practical applications.
In this context, this thesis proposes an answer to some of the challenges of long-range femtosecond laser pulse propagation, based on laser pulse modulation scenarios that guarantee to reach an on-target laser field with the desired properties. These scenarios were obtained by combining reverse engineering methods and numerical simulations. We show that different target fields can be easily and efficiently achieved by modulating the laser output field. Whenever possible, the modulation is obtained by simulating the reverse propagation of the target field towards the laser.

**Institut Polytechnique de Paris**
91120 Palaiseau, France